

REPORT DOCUMENTATION PAGE			Form Approved OMB NO. 0704-0188		
<p>The public reporting burden for this collection of information is estimated to average 1 hour per response, including the time for reviewing instructions, searching existing data sources, gathering and maintaining the data needed, and completing and reviewing the collection of information. Send comments regarding this burden estimate or any other aspect of this collection of information, including suggestions for reducing this burden, to Washington Headquarters Services, Directorate for Information Operations and Reports, 1215 Jefferson Davis Highway, Suite 1204, Arlington VA, 22202-4302. Respondents should be aware that notwithstanding any other provision of law, no person shall be subject to any penalty for failing to comply with a collection of information if it does not display a currently valid OMB control number.</p> <p>PLEASE DO NOT RETURN YOUR FORM TO THE ABOVE ADDRESS.</p>					
1. REPORT DATE (DD-MM-YYYY) 21-05-2015		2. REPORT TYPE Ph.D. Dissertation		3. DATES COVERED (From - To) -	
4. TITLE AND SUBTITLE Thin Film Materials and Devices for Resistive Temperature Sensing Applications			5a. CONTRACT NUMBER W911NF-06-2-0026		
			5b. GRANT NUMBER		
			5c. PROGRAM ELEMENT NUMBER 611102		
6. AUTHORS Hitesh Basantani			5d. PROJECT NUMBER		
			5e. TASK NUMBER		
			5f. WORK UNIT NUMBER		
7. PERFORMING ORGANIZATION NAMES AND ADDRESSES Pennsylvania State University Office of Sponsored Programs 110 Technology Center Building University Park, PA 16802 -7000			8. PERFORMING ORGANIZATION REPORT NUMBER		
9. SPONSORING/MONITORING AGENCY NAME(S) AND ADDRESS (ES) U.S. Army Research Office P.O. Box 12211 Research Triangle Park, NC 27709-2211			10. SPONSOR/MONITOR'S ACRONYM(S) ARO		
			11. SPONSOR/MONITOR'S REPORT NUMBER(S) 50361-EL-MUR.31		
12. DISTRIBUTION AVAILABILITY STATEMENT Approved for public release; distribution is unlimited.					
13. SUPPLEMENTARY NOTES The views, opinions and/or findings contained in this report are those of the author(s) and should not be construed as an official Department of the Army position, policy or decision, unless so designated by other documentation.					
14. ABSTRACT Thin films of vanadium oxide (VOx) and hydrogenated amorphous silicon (a-Si:H) are the two dominant material systems used in resistive infrared radiation detectors (microbolometers) for sensing long wave infrared (LWIR) wavelengths in the 8-14 μm range. Typical thin films of VOx (x < 2) currently used in the bolometer industry have a magnitude of temperature coefficient of resistance (TCR) between 2%/K to 3%/K. In contrast, thin films of hydrogenated germanium (SiGe:H) have TCR between 3%/K to 4%/K. Devices made from either of these materials have resulted in similar device performance with NETD < 25 mK. The performance of the					
15. SUBJECT TERMS Thin Film Materials and Devices for Resistive Temperature Sensing Applications					
16. SECURITY CLASSIFICATION OF:			17. LIMITATION OF ABSTRACT UU	15. NUMBER OF PAGES	19a. NAME OF RESPONSIBLE PERSON Mark Horn
a. REPORT UU	b. ABSTRACT UU	c. THIS PAGE UU			19b. TELEPHONE NUMBER 814-865-0332

Report Title

Thin Film Materials and Devices for Resistive Temperature Sensing Applications

ABSTRACT

Thin films of vanadium oxide (VO_x) and hydrogenated amorphous silicon (a-Si:H) are the two dominant material systems used in resistive infrared radiation detectors (microbolometers) for sensing long wave infrared (LWIR) wavelengths in the 8-14 μ m range. Typical thin films of VO_x ($x < 2$) currently used in the bolometer industry have a magnitude of temperature coefficient of resistance (TCR) between 2%/K to 3%/K. In contrast, thin films of hydrogenated germanium (SiGe:H) have |TCR| between 3%/K to 4%/K. Devices made from either of these materials have resulted in similar device performance with NETD \approx 25 mK. The performance of the microbolometers is limited by the electronic noise, especially 1/f noise. Therefore, regardless of the choice of bolometer sensing material and read out circuitry, manufacturers are constantly striving to reduce 1/f noise while simultaneously increasing TCR to give better signal to noise ratios in their bolometers and ultimately, better image quality with more thermal information to the end user.

In this work, thin films of VO_x and hydrogenated germanium (Ge:H), having TCR values > 4 %/K are investigated as potential candidates for higher sensitivity next generation of microbolometers. Thin films of VO_x were deposited by Biased Target Ion Beam Deposition (BTIBD) (~ 85 nm thick). Electrical characterization of lateral resistor structures showed resistivity ranging from $104 \mu\Omega/\square$ to $2.1 \times 10^4 \mu\Omega/\square$, TCR varying from 4%/K to 5%/K, normalized Hooe parameter ($\rho H/n$) of 5×10^{-21} to 5×10^{-18} cm³. Thin films of Ge:H were deposited by plasma enhanced chemical vapor deposition (PECVD) by incorporating an increasing amount of crystal fraction in the growing thin films. Thin films of Ge:H having a mixed phase, amorphous + nanocrystalline, having a |TCR| > 6 %/K were deposited with resistivity $< 2,300 \mu\Omega/\square$ and a normalized Hooe's parameter ' $\rho H/n$ ' $< 2 \times 10^{-20}$ cm³. Higher TCR materials are desired, however, such materials have higher resistivity and therefore unacceptable large electrical resistance in a lateral resistor configuration. This work looks at an alternate bolometer device design which incorporates higher TCR materials in a vertically integrated configuration.

iv

Thin films of high TCR hydrogenated germanium (Ge:H, |TCR| > 6 %/K) and vanadium oxide (VO_x, TCR > 5 %/K) were integrated in lateral and through film configuration. The electrical performance of the vertically integrated devices is compared with lateral resistance structures. It was confirmed experimentally that the device impedance was significantly lowered while maintaining the signal to noise ratio of the lateral resistor configuration. The vertically integrated devices allow higher device currents without any increase in self heating. These structures may help reduce integration time and may result in higher frame rate.

Finally, one dimensional arrays were fabricated using both lateral and vertically integrated configurations and their performance was evaluated. It was found that the performance of the lateral devices was limited by noise floor of the measurement setup used. However, due to the lower impedance of the vertically integrated resistors, a higher signal and therefore higher signal to noise ratio could be obtained. These vertically integrated devices exhibited low RMS noise values of 12 mK.

The Pennsylvania State University
The Graduate School
Department of Engineering Science and Mechanics

**THIN FILM MATERIALS AND DEVICES FOR
RESISTIVE TEMPERATURE SENSING APPLICATIONS**

A Dissertation in
Engineering Science and Mechanics
by
Hitesh A. Basantani

© 2014 Hitesh A. Basantani

Submitted in Partial Fulfillment
of the Requirements
for the Degree of

Doctor of Philosophy

December 2014

The dissertation of Hitesh A. Basantani was reviewed and approved* by the following:

Mark W. Horn
Professor of Engineering Science and Mechanics
Dissertation Advisor
Chair of Committee

Thomas N. Jackson
Robert E. Kirky Chair Professor of Electrical Engineering

Susan Troler-McKinstry
Professor of Ceramic Science and Engineering

Michael T. Lanagan
Professor of Engineering Science and Mechanics

S. Ashok
Professor of Engineering Science

Judith A. Todd
P. B. Breneman Department Head
Head of the Department of Engineering Science and Mechanics

*Signatures are on file in the Graduate School

ABSTRACT

Thin films of vanadium oxide (VO_x) and hydrogenated amorphous silicon (a-Si:H) are the two dominant material systems used in resistive infrared radiation detectors (microbolometers) for sensing long wave infrared (LWIR) wavelengths in the 8–14 μm range. Typical thin films of VO_x ($x < 2$) currently used in the bolometer industry have a magnitude of temperature coefficient of resistance (TCR) between 2%/K – 3%/K. In contrast, thin films of hydrogenated germanium (SiGe:H) have $|\text{TCR}|$ between 3%/K to 4%/K. Devices made from either of these materials have resulted in similar device performance with $\text{NETD} \approx 25 \text{ mK}$. The performance of the microbolometers is limited by the electronic noise, especially 1/f noise. Therefore, regardless of the choice of bolometer sensing material and read out circuitry, manufacturers are constantly striving to reduce 1/f noise while simultaneously increasing TCR to give better signal to noise ratios in their bolometers and ultimately, better image quality with more thermal information to the end user.

In this work, thin films of VO_x and hydrogenated germanium (Ge:H), having TCR values > 4 %/K are investigated as potential candidates for higher sensitivity next generation of microbolometers. Thin films of VO_x were deposited by Biased Target Ion Beam Deposition (BTIBD) (~85 nm thick). Electrical characterization of lateral resistor structures showed resistivity ranging from $10^4 \Omega\text{-cm}$ to $2.1 \times 10^4 \Omega\text{-cm}$, TCR varying from $-4\%/K$ to $-5\%/K$, normalized Hooe parameter (α_H/n) of 5×10^{-21} to $5 \times 10^{-18} \text{ cm}^3$. Thin films of Ge:H were deposited by plasma enhanced chemical vapor deposition (PECVD) by incorporating an increasing amount of crystal fraction in the growing thin films. Thin films of Ge:H having a mixed phase, amorphous + nanocrystalline, having a $|\text{TCR}| > 6$ %/K were deposited with resistivity $< 2,300 \Omega\text{-cm}$ and a normalized Hooe's parameter ' α_H/n ' $< 2 \times 10^{-20} \text{ cm}^3$.

Higher TCR materials are desired, however, such materials have higher resistivity and therefore unacceptable large electrical resistance in a lateral resistor configuration. This work looks at an alternate bolometer device design which incorporates higher TCR materials in a vertically integrated configuration.

Thin films of high TCR hydrogenated germanium (Ge:H, $|\text{TCR}| > 6\%/K$) and vanadium oxide (VO_x , $\text{TCR} > 5\%/K$) were integrated in lateral and through film configuration. The electrical performance of the vertically integrated devices is compared with lateral resistance structures. It was confirmed experimentally that the device impedance was significantly lowered while maintaining the signal to noise ratio of the lateral resistor configuration. The vertically integrated devices allow higher device currents without any increase in self heating. These structures may help reduce integration time and may result in higher frame rate.

Finally, one dimensional arrays were fabricated using both lateral and vertically integrated configurations and their performance was evaluated. It was found that the performance of the lateral devices was limited by noise floor of the measurement setup used. However, due to the lower impedance of the vertically integrated resistors, a higher signal and therefore higher signal to noise ratio could be obtained. These vertically integrated devices exhibited low RMS noise values of 12 mK.

TABLE OF CONTENTS

List of Figures	vii
List of Tables	viv
Acknowledgements.....	xv
Chapter 1. Introduction and Goals	1
1.1. Introduction	1
1.2. Statement of Problem	2
Chapter 2. Introduction to Temperature Sensing	3
2.1. Contact Temperature Sensors	3
2.1.1. Thermocouples	3
2.1.2. Resistance Thermometer Detectors (RTD)	4
2.1.3. Semiconductor Thermometers	4
2.2. Non-contact Thermometers or Pyrometers	6
2.2.1. Thermopiles.....	6
2.2.2. Pyroelectric Detectors	7
2.2.3. Photoconductive Detectors.....	7
2.2.4. Photovoltaic Cells	7
2.2.5. Thermistor or Metal Bolometers	7
2.3. Resistive Infrared Imaging or Microbolometer	9
2.3.1. Figures of Merit.....	10
2.3.2. Choice of Resistive Material	15
2.3.3. Comparison of Material Performance	30
2.3.4. Readout Circuits used in Infrared Imaging Focal Plane Arrays	31
Chapter 3. Experimental Methods.....	36
3.1. Deposition of VO _x Thin Films: The LANS Biased Target Deposition System	36
3.1.1. Ion Source used in BTM: Broad Beam, Gridless Ion Sources.....	38
3.1.2. Hollow Cathode Electron Source	45
3.1.3. Summary of Operation of 4Wave LANS system	49
3.2. Deposition of Hydrogenated Ge:H Thin Films	49
3.3. Characterization Techniques	51
3.3.1. Grazing Incidence X-Ray Diffraction (GIXRD).....	51
3.3.2. Atomic Force Microscopy (AFM)	52
3.3.3. Rutherford Backscattering Spectroscopy (RBS)	52
3.3.4. Ellipsometry	53
3.3.5. Resistivity Measurements.....	54
3.3.6. Temperature Coefficient of Resistance Measurements	56
3.3.7. Measurement of Electrical Noise in Thin Films.....	57

Chapter 4. High TCR Thin Films of Vanadium Oxide (VO_x) and Hydrogenated Germanium (Ge:H)	68
4.1. Introduction	68
4.2. High TCR VO_x Thin Films	70
4.2.1. Experimental Details	70
4.2.2. Results and Discussion	71
4.3. High TCR Mixed Phase Thin Films of Ge:H	75
4.3.1. Experimental Details	75
4.3.2. Results and Discussion	75
4.4. Conclusion	89
Chapter 5. High TCR Bolometers Using Vertically Integrated Thin Film Resistors	93
5.1. Introduction	93
5.2. Theoretical Performance of Through Film Structures	95
5.3. Experimental Details	98
5.3.1. Lithographic Fabrication of Device Structures	99
5.3.2. Deposition of High TCR, High Resistivity VO_x Thin Films	101
5.3.3. Deposition of High TCR, High Resistivity Ge:H Thin Films	102
5.3.4. Electrical Characterization of Device Performance	102
5.4. Experimental Results	105
5.5. Conclusion	110
Chapter 6. Resistive Temperature Sensing Arrays	111
6.1. Introduction	111
6.2. Array Design and Fabrication	111
6.2.1. Design and Processing of 1-D VO_x Sensor Array	111
6.2.2. One Dimensional Testing Setup	116
6.3. Results and Discussion	119
6.4. Conclusion	129
Chapter 7. Summary and Future Work	130
7.1. Summary	130
7.2. Future Work	131
Bibliography	137

LIST OF FIGURES

Figure 2-1. Calculated spectral radiant emissive power of a black body (in $\text{W/m}^2 \cdot \mu\text{m}$) at different temperatures.	8
Figure 2-2. The electromagnetic spectrum and the opacity of the atmosphere at different wavelengths, from ref. [16].	9
Figure 2-3. A schematic of a single free standing microbolometer with the underlying read out integrated circuit (ROIC), from ref. [17].	10
Figure 2-4. Noise equivalent circuit of a resistor for a 1-Hz bandwidth with an ideal resistance of R_B and an RMS current noise source I_N , Total in parallel with the resistor.	15
Figure 2-5. TCR vs. resistivity of various materials explored as candidates for temperature sensing [3] [18] [19] [20] [21] [22] [23] [24] [25] [26] [27].	16
Figure 2-6. Comparison of Resistivity vs. TCR of VO_x thin films deposited by ion beam sputtering [8] [33] and magnetron sputtering [37].	21
Figure 2-7. Graph showing the effect of total deposition pressure on TCR and resistivity of deposited pm-Ge:H thin films from ref [57].	24
Figure 2-8. Growth evolution diagram for Ge:H thin films grown on native oxide on c-Si showing the thickness values at which crystallization becomes evident (re-plotted from ref [19]).	25
Figure 2-9. Summary of electrical properties (resistivity, TCR and normalized Hooge's parameter) for thin films of Ge:H thin films deposited at different dilution ratios [19].	26
Figure 2-10. Electrical properties of (a+nc)-Ge:H thin films grown at $R = 225$ for increasing thicknesses. The x-axis plots the total nanocrystalline fraction as it relates to the thickness [19].	27
Figure 2-11. Cross-sectional TEM dark field image of an $R = 400$ (a+nc)-Ge:H thin. The amorphous regions are uniformly illuminated, while the crystalline regions appear light or dark depending on their orientation. Two of the approximately ten discernible cones are oriented such that twinning can be seen [19].	28
Figure 2-12. Surface roughness evolution for Ge:H films deposited at different dilution ratios, R . Higher dilution ratios show an increase in surface roughness at smaller thicknesses, indicating film transformation from amorphous to a mixed phase thin film ref. [19].	29
Figure 2-13. Surface roughness evolution for films deposited at increasing substrate temperatures on to SiN_x substrates on c-Si. Lower substrate temperatures result in a quicker decrease in roughness, indicating a more a more prompt coalescence [19].	29

Figure 2-14. The readout circuit for a pulse biased VO_x based 160×128 bolometer array developed at FLIR [59].	32
Figure 2-15. Schematic of the L-3 EOS switched capacitor filter/integrating amplifier integrated in the unit-cell of each pixel as in ref [60].	34
Figure 3-1. Concept sketch of Biased Target Ion Beam Deposition system [61].	36
Figure 3-2. Schematic of the Laboratory for Alloying and Nano layer Sputtering by the 4Wave Inc. used in this work [62].	37
Figure 3-3. Schematic of a) Cross-section of one of the first ion sources, b) Electrical diagram of a basic ion source as it appears in ref. [64].	40
Figure 3-4. Various processes in an end-Hall ion source [66].	41
Figure 3-5. Voltage-current characteristics (between 5×10^{-5} Torr and 1×10^{-3} Torr) of an end-Hall ion source showing the various regimes of operation of its plasma discharge. The two curves show the voltage-current characteristics for a discharge current of $I_d = 5\text{A}$ and corresponding ion beam current of I_i [61].	42
Figure 3-6. An End-Hall ion source with a grooved anode and baffle to reduce anode “poisoning”/oxidation [61].	44
Figure 3-7. a) Angular retarding potential analysis of a modified KRI EH1000 ion source indicating most ions having energy $< 30\text{ eV}$. The measurements were made at a distance of 30 cm. b) Angular retarding potential analysis of a modified KRI End-Hall 1000 ion source as a function of distance from the ion source. The operating gas is Ar at a pressure of 1 mTorr. The discharge characteristics were 10 Amperes at 42 V with a gas flow of 70 sccm [68].	44
Figure 3-8. Spherical ion current density profiles for the KRI End-Hall 1000 ion source with the source at the center of the sphere. Source to target distance is 30 cm (12 in.). The working gas was 70 sccm of argon and the discharge characteristics were 10 A and 45 V [68].	45
Figure 3-9. Typical ion beam energy distribution for different neutralization ratios: $I_{em} (3.8\text{ A}) < I_d (4\text{ A})$, $I_m = I_d = 4\text{ A}$ and $I_{em} (6\text{ A}) > I_d (4\text{ A})$ [61].	46
Figure 3-10. Schematic and electrical circuit diagram of a hollow cathode assembly [71].	47
Figure 3-11. An end-Hall ion source showing the typical placement of a filament [68].	48
Figure 3-12. Schematic of the plasma enhanced CVD deposition chamber used to deposit the Ge:H of this work as it appears in ref. [72].	50
Figure 3-13. Schematic of a typical RBS experimental setup.	53
Figure 3-14. Typical configuration for ellipsometry measurement [75].	54
Figure 3-15. Transmission Line Method test structures showing features used in isolation of the TCR material and to deposit the metal contacts.	55

Figure 3-16. Plot of total resistance as a function of electrode spacing.....	56
Figure 3-17. Schematic images from the mask set used to extract the normalized Hooge's parameter. Each pattern has a different volume but the same resistor width to length ratio.	58
Figure 3-18. Schematic of lithographic processing of TCR material to extract resistivity, TCR and the normalized Hooge's parameter.....	59
Figure 3-19. Resistance fluctuation (drift) of a thin film resistor of vanadium oxide capped with SiO ₂	61
Figure 3-20. The recorded PSD for varying magnitudes of drift, C. The peak represents the 1/f noise (in this case at 10 Hz).	62
Figure 3-21. A schematic showing the process flow used in this work for the measurement of 1/f noise in thin films.	64
Figure 3-22. Frequency spectra representation of collected spectra showing two distinct regions: a) Region with 1/f noise and, b) Region with Johnson noise	65
Figure 3-23. Acquired Power Spectral Densities of a thin film for different volumes and different biases to confirm the Hooge–Vandamme relation and extract the materials normalized Hooge's parameter.	66
Figure 4-1. Deposition rate, resistivity and TCR of thin films of VO _x deposited by Biased Target Ion Beam Deposition as a function of partial pressure of O ₂ as it appears in ref. [79].....	69
Figure 4-2. Grazing incidence X–ray diffraction spectra associated with high resistivity VO _x thin films deposited at high partial pressure of oxygen using Biased Target Ion Beam Deposition showing amorphous thin film structure.....	72
Figure 4-3. Resistivity, temperature coefficient of resistance (TCR) and the normalized Hooge's parameter (α_H/n) of VO _x thin films deposited by BTIBD as a function of partial pressure of oxygen (pO ₂).	74
Figure 4-4. Resistivity and TCR of lithographically patterned samples of Ge:H as a function of thickness. The electrodes used for electrical measurements were evaluated to ensure ohmic contacts were obtained for all measurements.	76
Figure 4-5. The measured Power Spectral Density (PSD), S_I^2/I_{bias}^2 , for the 100 nm sample of Ge:H showing volume dependence as predicted by the Hooge-Vandamme relation.....	77
Figure 4-6. Extracted normalized Hooge's parameter ' α_H/n ' as a function of thickness for thin films of Ge:H each annotated with their corresponding value of TCR. Note that the 100 nm thin film had the lowest α/n value while having the highest TCR.	78
Figure 4-7. Grazing incidence x-ray diffraction pattern of a 200 nm thin film of Ge:H confirming the presence of diamond cubic crystal phase (as indexed).	79

Figure 4-8. Bragg-Brentano x-ray diffraction pattern of the 200 nm thin film of Ge:H used to extract the size of crystals to the first order using the Scherrer's formula.	80
Figure 4-9. Dark field TEM micrograph of a 250 nm thin film of Ge:H showing the presence of nanocrystallites in an amorphous matrix [published previously in ref. [19].	81
Figure 4-10. AFM micrographs of Ge:H thin films with thicknesses a) 7 nm and b) 200 nm presenting differences in surface morphology. The 200 nm thin film shows larger grains and larger peak-to-valley heights than the 7 nm thin film.....	82
Figure 4-11. A three dimensional AFM micrograph showing the peak-to-valley roughness associated with the large grain sizes for the 100 nm thin film of Ge:H deposited in this work.....	83
Figure 4-12. Peak to valley height (red) and RMS roughness (black) of thin films of Ge:H deposited in this work.	84
Figure 4-13. Surface roughness and nanocrystallite fraction for Ge:H on native oxide coated crystalline silicon (c-Si) obtained from two layer modeling and virtual interface analysis (VIA) of real time spectroscopic ellipsometry (RTSE) measurements. The nanocrystallite fraction profile used in the analysis of the single final set of spectra is also shown.....	85
Figure 4-14. Complex dielectric function, $\epsilon = \epsilon_1 + i\epsilon_2$, spectra for nanocrystalline Ge:H (nc-Ge:H) obtained in situ, in vacuum from virtual interface analysis of RTSE data and obtained ex situ, after atmospheric exposure.	87
Figure 4-15. Spectra in ϵ for nc-Ge:H obtained ex situ, after atmospheric exposure for nominally 100 and 200 nm thick films.	88
Figure 4-16. A comparison of Resistivity vs. TCR of thin films reported in literature to the thin films of Ge:H and VO _x deposited in this work.	90
Figure 4-17. A comparison of the Normalized Hooge's parameter of some common materials reported in literature vs. thin films deposited in this work. The dotted line represents a constant ratio of $\alpha_H/n : TCR^2$	91
Figure 5-1. The three bolometer design structures explored by Unewisse et al. in ref. [107].	94
Figure 5-2. Graph showing theoretically calculated values of the power dissipated (red) and the maximum attainable signal to noise ratio (black) for a thin film device with a resistivity of 20,000 Ω -cm and dimensions of 17 $\mu\text{m} \times 17\mu\text{m}$	98
Figure 5-3. Cross-sectional schematic of bolometer configurations explored: a) In-plane conductivity (top); b) Out-of-plane conductivity (bottom).	99
Figure 5-4. Lithographic processing for through film resistance structures.	100

Figure 5-5. Top view of a mask set showing the different layers used for fabricating the out of plane resistance structure.	100
Figure 5-6. Resistance vs. electrode spacing measurements used to extract the sensing material's resistivity and the contact resistance.	103
Figure 5-7. Top view of the mask set used for the measurement of resistivity of the sensing material.....	103
Figure 5-8. A plot of resistance vs. 1/Area used to extract the resistivity of the sensing material as measured from the structures in Figure 5-7. By dividing the slope of the line and the thickness of the film, the material's resistivity can be extracted.	104
Figure 5-9. Current density as a function of electric field applied across the thin film resistor.....	106
Figure 5-10. Lateral and through film resistivity of thin films of Ge:H thin films as a function of thickness. The through film resistivity increases dramatically for smaller thicknesses, indicating an insulating interfacial layer between the bottom metal and the resistive thin film.....	107
Figure 5-11. Resistance vs. temperature plots for thin films of VO _x and Ge:H fabricated in lateral and through film configuration showing orders of magnitude difference in resistance but similar TCR.	108
Figure 5-12. The measured Power Spectral Density (PSD), S_I^2/I_{bias}^2 for a 50 nm thin film of Ge:H showing good agreement with the Hooge's relationship, independent of device structure used (lateral or through film). Inset shows the PSD normalized for volume.....	109
Figure 6-1. Schematic showing the 1x8 temperature sensing array fabricated in this work. The top of the sensor is kept narrow while the leads are spread out to facilitate wire bonding.....	112
Figure 6-2. Schematic of the top of the 1 × 8 vertically integrated VO _x sensor array fabricated in this work. All through film sensors were electrically shorted during fabrication, dicing and wire bonding. Prior to measurement they were cut using a micromanipulator.	113
Figure 6-3. Equivalent circuit diagram showing VO _x resistors integrated with ZnO transistors as fabricated in this work.	114
Figure 6-4. Schematic of lateral VO _x sensors integrated with ZnO based transistors. To allow for low impedance, the width to length ratio of 200μm/5μm was designed for both the VO _x resistors (100 MΩ) and the ZnO transistors (4,000 Ω).....	115
Figure 6-5. Schematic of vertically integrated VO _x sensors with ZnO based transistors. The through film resistors had dimensions of 10 μm × 10μm × 100 nm (1.3 MΩ), while the ZnO transistors were fabricated with a width to length ratio of 450 μm/ 5μm (1,500 Ω).....	116

Figure 6-6. Equivalent circuit diagram of the 1x8 array fabricated in this work. The resistors can be lateral or vertically integrated, a Keithley 7075 general purpose multiplex card is used as the switch matrix while an HP4141B DC SMU is used for measuring the output current.....	117
Figure 6-7. Test setup for the measurement of the 1-D arrays. ACF bonded samples on a VWR heater block (left) and the sensor biasing hardware including the HP4141B DC SMU and the Keithley 707A mainframe consisting of the Keithley 7075 general purpose multiplex card (right).....	118
Figure 6-8. Screenshot of the C++ based program written to readout the 1D array by remote operation of the HP4141B DC SMU and the Keithley 7075 general purpose multiplex card. The program sets parameters for the array voltage bias, current measurement, the number of spot measurements to be performed and the wait time between each measurement.....	118
Figure 6-9. Current output for a lateral VO _x sensor with a resistance of $\approx 50 \text{ M}\Omega$ at 35 °C measured over 24 hours. The periodicity arises from the attempts of the heater block to stabilize to a set point of 35 °C. The measured RMS noise was found to be 160 mK.....	119
Figure 6-10. Current output of the 8 VO _x temperature sensor array measured at 35 °C on a VWR heater block at bias voltage of 1 V for 24 hours.....	120
Figure 6-11. Output current of vertically integrated VO _x sensors $10 \text{ }\mu\text{m} \times 10 \text{ }\mu\text{m} \times 85 \text{ nm}$ having a resistance of $1.3 \text{ M}\Omega$ at a temperature of 35 °C. The resistor was biased with a voltage of 100 mV. The measured RMS noise was found to be $\approx 35 \text{ mK}$	122
Figure 6-12. A plot of natural log of resistance as a function of temperature for lateral thin film resistors of VO _x having dimensions of $10 \text{ }\mu\text{m} \times 50 \text{ }\mu\text{m} \times 85 \text{ nm}$. The TCR extracted using activation energy was found to be $-4.4 \text{ \%}/\text{K}$	122
Figure 6-13. A plot of leakage current through the ribbon cables used during measurement.	123
Figure 6-14. Output current of vertically integrated VO _x sensors $10 \text{ }\mu\text{m} \times 10 \text{ }\mu\text{m} \times 85 \text{ nm}$ having a resistance of $1.3 \text{ M}\Omega$ at a temperature of 35 °C measured without a switch matrix using the HP4141B DC SMU. The resistor was biased with a voltage of 100 mV. The measured RMS noise was found to be $\approx 12 \text{ mK}$	124
Figure 6-15. Linear region $\log(I_D)$ versus V_{GS} of a ZnO based TFT with a linear region differential mobility of $10 \text{ cm}^2/\text{V}\cdot\text{s}$ for a V_{DS} of 1 V. The TFT dimensions are $W/L = 400 \text{ }\mu\text{m}/15 \text{ }\mu\text{m}$ and $t_{ox} = 32 \text{ nm}$. The R_{on} for this W/L ratio was $\approx 4,000 \text{ }\Omega$ for a V_{GS} of 10 V.	125
Figure 6-16. $\log(I_D)$ versus V_G for a ZnO based TFT with a vertically integrated with vertically integrated VO _x resistor ($1.6 \text{ M}\Omega$ at room temperature) on the transistor drain for a V_{DS} of 75 mV ($W/L = 450 \text{ }\mu\text{m}/5 \text{ }\mu\text{m}$, $t_{ox} = 32 \text{ nm}$).....	126
Figure 6-15. I_D versus V_{DS} of a ZnO based TFT with a vertically integrated with vertically integrated VO _x resistor ($1.6 \text{ M}\Omega$ at room temperature) on the transistor drain as a function of V_{GS} from -1 V to 5 V ($W/L = 450 \text{ }\mu\text{m}/5 \text{ }\mu\text{m}$, $t_{ox} = 32 \text{ nm}$). I_D - V_D at V_{GS} of	

4 V and 5 V are similar indicating a small impedance contribution from the ZnO TFT.....	127
Figure 6-16. I_D versus V_{DS} of a ZnO based TFT with a vertically integrated VO_x resistor (1.6 M Ω at room temperature) on the TFT drain as a function of temperature for a V_{GS} of 5 V ($W/L = 450 \mu\text{m}/5 \mu\text{m}$, $t_{ox} = 32 \text{ nm}$). Increasing temperature of the device leads to lower resistance of the VO_x thin film at higher temperatures which is evident from the increasing slopes of the I_D - V_D characteristics.....	128
Figure 6-17. \ln (Resistance) versus temperature of vertically integrated VO_x thin film resistors (1.6 M Ω at room temperature) integrated with ZnO TFT at a V_{GS} of 5 V ($W/L = 450 \mu\text{m}/5 \mu\text{m}$, $t_{ox} = 32 \text{ nm}$). The TCR extracted from the activation energy was found to be -4.4 %/K.....	128
Figure 7-1. Resistivity and TCR of thin films of VO_x deposited by pulsed DC magnetron sputtering using a pure vanadium target with a substrate bias of -250 V. The graph is a compilation of thin films deposited in previous work [44], and films deposited in this work.....	133
Figure 7-2. A schematic showing the layout of an 8×8 temperature sensor array with integrated TFTs for two dimensional temperature sensing applications.....	135

LIST OF TABLES

Table 1. Parameters for commonly used IR imaging layers [17] [18].	30
Table 2. Parameters used for deposition of VO _x thin films in this work	49
Table 3. Parameters and their values used for estimating the SNR ratio and the power dissipated as a function of applied bias.	97
Table 4. Summary of TCR and ' α_H/n ' values in lateral and through film configuration deposited in this work.	109
Table 5. Typical parameters used for the deposition of VO _x thin films for this chapter	113
Table 6. Assumed parameters for SNR calculation	121

ACKNOWLEDGEMENTS

The proverb, “It takes a village to raise a child” is certainly true of my time in graduate school. This work would not have been possible without the encouragement and support in both professional and personal capacity by numerous people who I would like to acknowledge. Firstly, I would like to thank the U.S. Army Research Office and U.S. Army Research Laboratory for funding this work.

I would like to thank my advisor Dr. Mark Horn for giving me this opportunity, for providing guidance, constant support, and for always encouraging thought-provoking discussions. Secondly, I would like to acknowledge Dr. Thomas Jackson for being an excellent advisor and a tremendous role model. I would like to thank him for treating me as his graduate student and providing me with limitless resources without which this work would not have been possible.

I would like to thank the Penn State Nanofabrication facility, especially William Drawl who mentored me when I was a superuser for the group. Bill is an excellent teacher with a lot of patience. Without his trust, encouragement, and mentorship I would have never been able to develop the hands on skills which will be valuable as I grow in my career.

I would like to thank Dr. David Saint John for introducing me to PECVD hydrogenated germanium and taking the time to assist in the thin film depositions of this work. I would also like to thank Dr. Nikolas Podraza and Dr. Michael Motyka for teaching me valuable skills related to ellipsometry and for helping with data analysis. In addition, I would also like to thank fellow graduate students, Yao Jin, Myung-Yoon Lee, Israel Ramirez and Haoyu Li for many useful discussions and assistance.

I would like to thank my family, Arjun, Meena and Perna for their unconditional love and support, without which I would have given up a long time ago; and finally my fiancée Jennifer Ober, for her constant love, support and unlimited patience, especially over the last year of this doctorate.

Chapter 1. Introduction and Goals

1.1. Introduction

Temperature sensing is the measure of the heat of a body. There are two types of thermal sensors, contact and non-contact sensors. The contact sensors touch the object being measured, while the noncontact sensors measure the temperature by measuring the infrared radiation emitted by that object. The second chapter provides background on temperature sensing and compares the different types of temperature sensors available in order to put in perspective the work done in this thesis.

Noncontact thermal imaging systems, also known as infrared imaging arrays, have seen a marked increase in the last decade and find applications in both military and civil applications. These systems consist of arrays of micromachined sensors, known as microbolometers, based on an electrical response from resistors, capacitors, etc. Resistive thin films of VO_x and $\text{Si}_{1-x}\text{Ge}_x\text{:H}$ are the imaging materials that are the most dominant types of infrared imaging systems. The second chapter also provides an overview of the state-of-the-art resistive microbolometer technology based on VO_x and $\text{Si}_{1-x}\text{Ge}_x\text{:H}$ thin films, and discusses important figures of merit and the read out circuits used in such devices. These discussions will help understand why detectors based on materials with vastly different electrical properties lead to similar detector sensitivity.

Chapter 3 provides an overview of experimental aspects of this thesis including the processing and characterization techniques used in this work. Relevant literature on the thin film deposition techniques is reviewed in this section. Details on thin film lithographic processing, electrical characterization, X-ray diffraction (XRD), atomic force microscopy (AFM), spectroscopic ellipsometry (SE), Rutherford backscatter spectroscopy (RBS) are also discussed in context with this chapter.

1.2. Statement of Problem

The performance of thin films of VO_x and $\text{Si}_{1-x}\text{Ge}_x\text{:H}$ has remained relatively unchanged since the first literature appeared detailing their use. For years, much of the effort to improve the detector performance was focused towards improvement of the performance in the underlying read out circuits. However, as the need for higher density pixel arrays increases, the performance of these infrared systems is being limited by the signal to noise ratio of existing thin films. This motivated the study of high TCR materials having reasonably low electrical noise, which has been explored in Chapter 4 of this work. Thin films of VO_x and Ge:H have been explored with a focus on depositing and characterizing thin films having $|\text{TCR}|$ values $> 3\%/K$.

Although numerous materials have a high TCR, the accompanying large resistance in a lateral pixel configuration makes integration with existing readout circuits difficult. Chapter 5 investigates an alternate pixel geometry so as to reduce the device resistance and facilitate integration of high TCR materials.

Finally, the high TCR thin films of VO_x were exploited in temperature sensors arrays fabricated on glass substrates. Chapter 6 describes the fabrications of these thin film sensor arrays using both the lateral and the vertically integrated configuration. Two dimensional arrays were also fabricated and were multiplexed using integrated ZnO transistors fabricated on the underlying circuits. The resulting devices were characterized for their performance.

Chapter 2. Introduction to Temperature Sensing

Temperature is a measure of heat of an object. The concept of temperature invokes the physiological experience of touching an object and describing them as cold, cool, warm, hot, etc. Warmer objects transfer heat to colder objects till both their temperatures have reached equilibrium.

Temperature is an important physical parameter which influences all physiological, and thermal processes. Proper functioning of these processes requires accurate measurement of the corresponding temperature. There is a vast and an ever-growing number of methods for temperature sensing, however, the measurement techniques best suited for the application must be chosen in order to obtain readings which are as precise as required by that application.

Temperature sensors (or thermometers) can be classified based on heat transfer mechanisms as either contact or non-contact sensors.

2.1. Contact Temperature Sensors

The most accurate type of contact sensors are the electrical response contact sensors. In these types of sensors, the temperature response is converted into an electrical signal. Some commonly used electric contact sensors are discussed below:

2.1.1. Thermocouples

The thermocouple is based on the phenomenon known as the Seebeck effect. Named after the T. Seebeck who first observed this effect, he noted that there is a current flow in a closed loop of two dissimilar metals if their junctions are kept at two different temperatures. The corresponding voltage associated with this effect is known as the thermal electromotive force. A device which uses the Seebeck effect for the measurement of temperature is known as a thermocouple.

A thermocouple consists of two wires of dissimilar conductors (metals, alloys or semiconductors) connected at one end. The connected end is placed at the point of measurement, while the unconnected

end is the reference junction and can be used to readout the electromotive force developed using a voltmeter. Depending on the material used, these thermocouples can have an operation range of up to 3000 °C [1]. The most sensitive thermocouples are based on two alloys made from Nickel-chromium or Nickel-copper [1]. Thermocouples made from these alloys can achieve a sensitivity of 6.32 mV/ 100°C and have an operating range of 0°C to 1100°C [1]. The accuracy of such thermocouples is $\approx \pm 1$ °C [1].

2.1.2. Resistance Thermometer Detectors (RTD)

Resistance thermometers consist of thin wires of a metal or an alloy whose resistance changes linearly as a function of temperature. Platinum, Nickel, Copper and alloys of Rhodium-Iron are some commonly used materials in resistance thermometers [1] [2]. Nickel has the largest temperature response that of 0.62 %/K while Platinum has the highest range of operation between –260 K to 1100 K [1]. Due to the low resistivity of these materials, they are usually thin, long wires wound into a small form factor. The typical accuracy of measurement of RTDs in this form factor is $\approx \pm 0.2$ °C. Typical limitations include a relatively large form factor, cost associated with platinum wires and a high response time associated with the large thermal mass of the wires. Thin films have also been fabricated using these materials and thus have the advantage of miniaturization and the ability to fabricate temperature sensing arrays.

2.1.3. Semiconductor Thermometers

Semiconductor thermometers are made from semiconductor materials and can be divided into two main groups: bulk effect and junction effect sensors. In these types of temperature sensors, the conductivity of the semiconductor material changes due to a change in temperature of that material.

2.1.3.1. Thermistors

In these types of materials the resistance of the material changes as a function of temperature. This change in resistance can be readout electrically to give the change in temperature of the body under investigation. The resistance change of a thermistor is non-linear and follows a thermally activated behavior described by the Arrhenius equations such that:

$$R_T = R_0 e^{-E_a/k_B T^2} \quad \text{Equation 1}$$

Where R_T is the temperature of the thermistor at a temperature T . R_0 is the temperature at room temperature, k_B is the Boltzmann's constant, and E_a is the activation energy which is a material property of the thermistor.

The temperature response or the temperature coefficient of resistance (TCR) of the thermistor can then be estimated as:

$$TCR (in \% / K) = \frac{-E_a}{k_B T^2} \times 100 \quad \text{Equation 2}$$

Thermistors are typically made using ceramic manufacturing techniques from oxides of Mn, Ni, Co and Cu; they are pressed at high pressures and sintered at temperatures up to 1000 °C [1] [3]. Typical TCR values of thermistor lie between $-2 \% / K$ to $-6 \% / K$ [1]. This temperature response makes these thermistors some of the most sensitive types of temperature detectors with temperature errors as low as ± 0.1 °C [1] [4]. Limitations of thermistors include a lower and a smaller temperature range of operation (typically between -100 °C and 200 °C) and the non-linearity of the electrical response [5].

2.1.3.2. Diode and Transistor Based Thermometers

The output characteristics of a junction are dependent on its temperature of operation such that:

$$I_d (T) = I_S \left(e^{\frac{V_D}{n V_T}} - 1 \right) \quad \text{Equation 3}$$

Where I_d is the forward current of the diode, I_S is the reverse saturation current, V_D is the forward bias voltage, n is the ideality factor and V_T is the thermal voltage associated with temperature T (26 mV at 300 K). The change in V_T associated with the change in temperature can be used to calculate the temperature of the object with respect to a reference. Commercial temperature sensors based on junction effect are available and have a sensitivity of -2 mV/°C for silicon based diodes and -1.25 mV/°C for germanium

based diodes [1]. In addition, sensitivity as high as 40 mV/°C has been demonstrated using ZnO based transistors [6].

2.2. Non-contact Thermometers or Pyrometers

Pyrometers or infrared detectors are thermometers which measure the temperature of the object based on the emitted thermal radiation of that object. Pyrometers are commonly used in applications such as infrared imaging [7] [8] [9], temperature sensors for biological applications [10] [6], aerodynamics and space exploration [11], monitoring industrial processes, etc.

According to the Stefan-Boltzmann's law, the total radiant intensity W_0 of a black body depends on its temperature T [1]:

$$W_0 = \sigma_0 T^4 \quad \text{Equation 4}$$

σ_0 is the Stefan-Boltzmann's constant and has a value of $5.67 \times 10^{-8} \text{ W/m}^2\text{K}^4$

The spectral radiant flux distribution is given by [1]:

$$W_{0\lambda} = \frac{c_1 \lambda^{-5}}{e^{c_2/\lambda T} - 1} \quad \text{Equation 5}$$

where $W_{0\lambda}$ is the spectral radiant flux distribution of a black body in $\text{W/m}^2\mu\text{m}$, T is the temperature of the black body in K, $c_1 = 3.7415 \times 10^{-16} \text{ W.m}^2$ and $c_2 = 14,388 \mu\text{m.K}$.

There are numerous detectors that can be used for detection of thermal radiation. Some common detector types are discussed in detail in the following subsections.

2.2.1. Thermopiles

A thermopile is a series connection of numerous thermocouples whose hot junction is in contact with a black body which absorbs the incident radiation. Since a single thermocouple produces a small

electromotive force, a series of such thermocouples can produce thermometers with high sensitivity. Such devices have demonstrated sensitivity of several hundred $\mu\text{V/K}$. Detailed descriptions of state-of-the-art thermopiles can be found elsewhere in refs. [3] [12].

2.2.2. Pyroelectric Detectors

Pyroelectric detectors are based on the principle that the dipole moments in a pyroelectric material change their orientation as a function of temperature. Materials such as lead zirconium titanate (PZT), triglycine sulphate (TGS) and barium strontium titanate (BST) have a large pyroelectric coefficient response $> 2 \times 10^{-8} \text{ C-cm}^{-2}\text{-K}^{-1}$ [1] [3]. Thin film temperature sensing arrays have been fabricated using pyroelectric materials, the details of which can be found in ref. [3] [13] [14].

2.2.3. Photoconductive Detectors

Photoconductive detectors are made from materials whose electrical conductivity changes due to the generation of carriers in the material as a function of incident radiation. Depending on the choice of material, the detector can have a different spectral response. For example, CdS has a spectral response in the visible spectral region while PbS is in the $0.5 \mu\text{m}$ – $4 \mu\text{m}$ wavelength range.

2.2.4. Photovoltaic Cells

A photovoltaic device generates a voltage depending on the incident infrared radiation. The photovoltaic material absorbs radiation, exciting valence band electrons into its conduction band. Similar to other photoelectric detectors, the spectral response depends on the choice of material. InAs has a spectral response between $1 \mu\text{m}$ – $3.8 \mu\text{m}$ while InSb has a maximum sensitivity to radiation of wavelength $8 \mu\text{m}$.

2.2.5. Thermistor or Metal Bolometers

Bolometers based on thermistors or metal bolometer arrays are thermometers based on the temperature coefficient of resistance of the thermistors or metals. However, in these non-contacting detectors, the heating of the resistor takes place by absorption of the infrared radiation by the material or by an absorber layer for non-absorbing thermistor materials [3]. These types of detectors are by far the

most popular for imaging in the 8 μm –14 μm range [15]. Bolometers, especially microbolometers are the focus of this work and are discussed in greater detail in the subsequent sections.

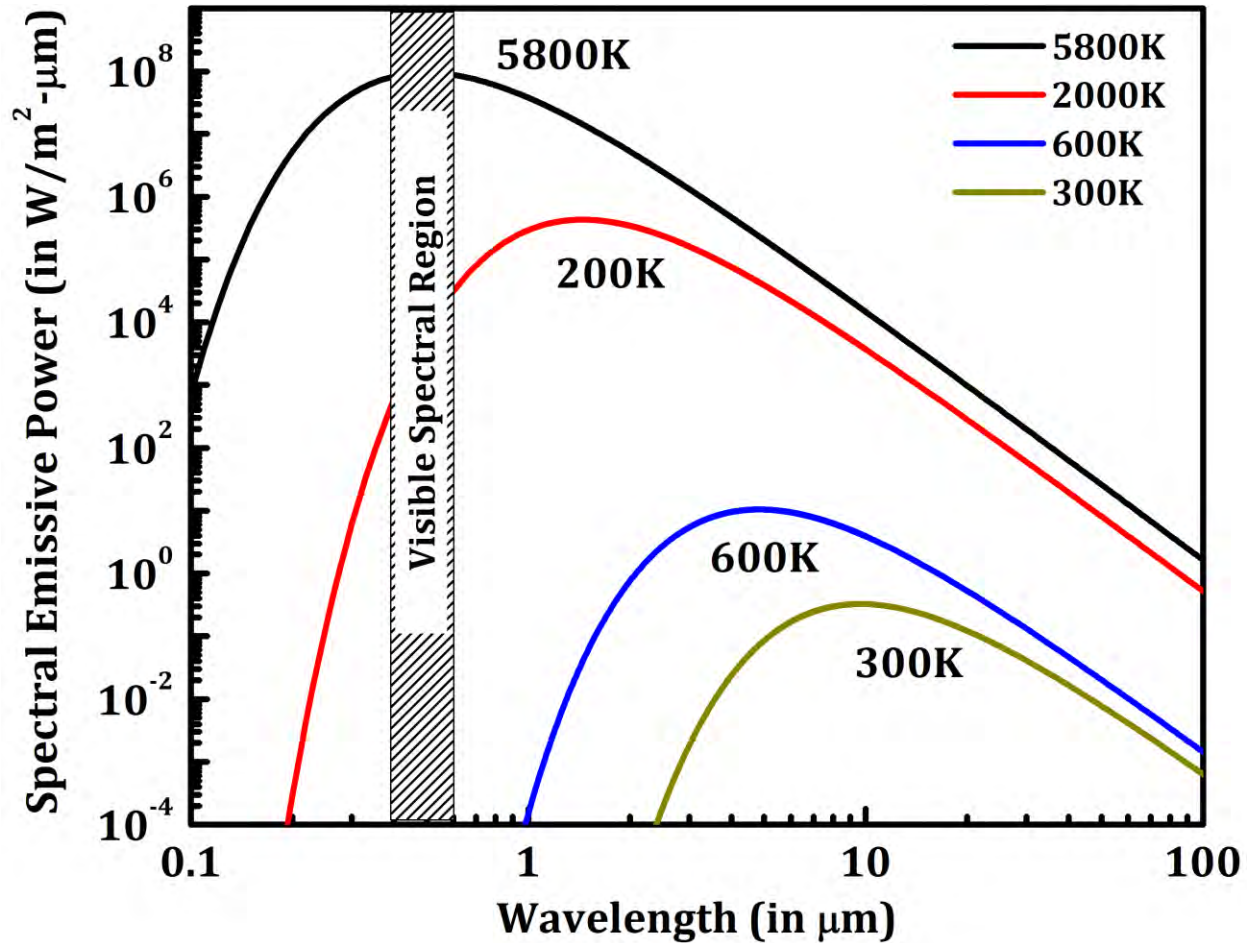


Figure 2-1. Calculated spectral radiant emissive power of a black body (in $\text{W}/\text{m}^2 \cdot \mu\text{m}$) at different temperatures. The maximum emissive power for objects $\approx 300\text{ K}$ lies between 8 and 14 μm .

Figure 2-1 shows the spectral emissive power of a black body in accordance with Equation 5 at different temperatures of the object. The choice of infrared detector depends on the desired temperature range of measurement. One of the biggest applications for temperature sensing is room temperature imaging of objects at temperatures between $-40\text{ }^\circ\text{C}$ and $120\text{ }^\circ\text{C}$. Today, the most common type of detector for room temperature infrared imaging is based on thermistor materials whose resistance changes as it heats up due to incident infrared. This imaging technique is described in the subsequent subsections in further detail.

2.3. Resistive Infrared Imaging or Microbolometer

A bolometer is a temperature-sensitive electrical resistor whose resistance changes due to an increase in temperature caused by incident infrared radiation. The magnitude of the resistance change is proportional to the temperature of the black body emitting the incident radiation. Two dimensional arrays of miniaturized resistors (microbolometer) can be used for mapping the thermal field of the scene under investigation.

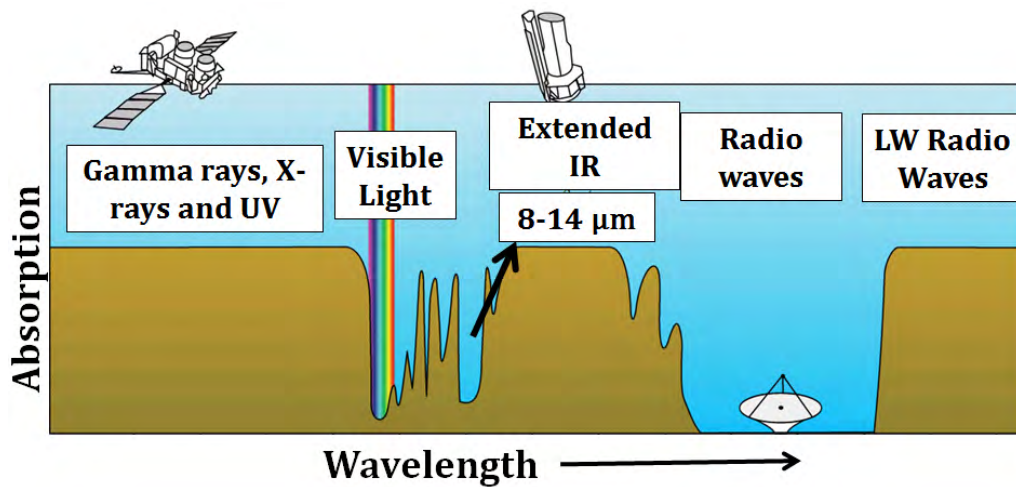


Figure 2-2. The electromagnetic spectrum and the opacity of the atmosphere at different wavelengths, from ref. [16].

Since a microbolometer is a non-contact temperature sensor, the infrared radiation must travel through the atmosphere before it reaches the detector element. H_2O and CO_2 molecules present in the atmosphere absorb certain wavelengths of radiation, as can be seen in Figure 2-2 [16]. Radiation in the 3–5 μm range (Mid-Wavelength IR or MWIR) and 8–14 μm range (Long Wavelength IR or LWIR) is transmitted through the atmosphere and can be used for detecting infrared radiation. Due to the higher intensity of radiation in the 8–14 μm band at 300K (Figure 2-1), LWIR detectors are preferred. However the choice of detector depends on the specific application at hand.

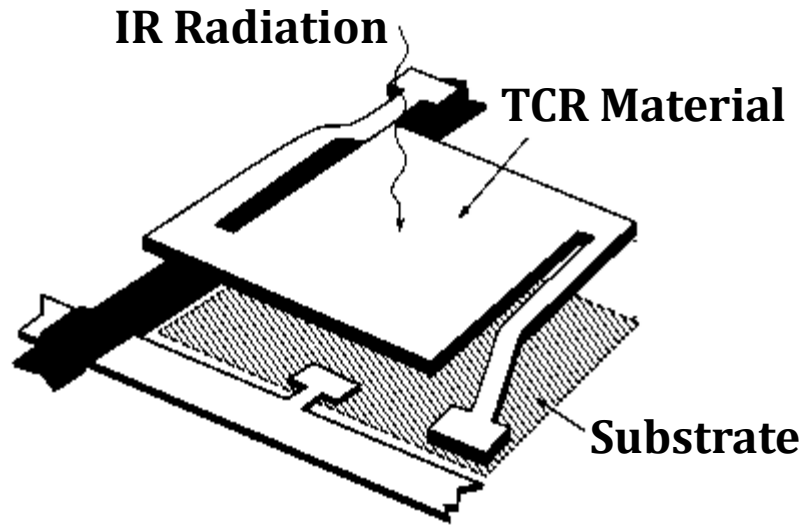


Figure 2-3. A schematic of a single free standing microbolometer with the underlying read out integrated circuit (ROIC), from ref. [17].

The actual sensor used for infrared imaging is a monolithic structure prepared by silicon micromachining, originally developed by Honeywell [8]. A simplified schematic of such a pixel structure is shown in Figure 2-3. The detecting area is a thin film of the temperature sensitive material employed (metal or semiconductor) having a temperature coefficient of resistance (TCR) of α , atop a thin free standing membrane, usually Si_3N_4 [17] [3]. The membrane is supported by legs which have a low thermal conductance to maximize thermal isolation from the environment. The legs also have a thin film of metal which serve as electrical contacts to the resistive thin film. In addition, the underlying substrate has a reflective thin film which causes the unabsorbed radiation to reflect back to the resistive layer [17] [3]. It was found that the reflection is at a maximum when the spacing between the reflective layer and the suspended resistor is one quarter of the wavelength being sensed [3] [17].

2.3.1. Figures of Merit

The performance of a microbolometer depends on two important properties which are discussed in further detail in the following subsections.

2.3.1.1. Temperature Coefficient of Resistance (TCR)

The performance of a microbolometer depends on several factors, one of which is the temperature coefficient of resistance or TCR. The temperature coefficient of resistance is defined as the percentage change in resistivity of the material per degree Kelvin of increase in its temperature. TCR can be negative or positive. While metals have a positive TCR, semiconductors have a TCR which is typically negative. In general, TCR can be defined using Equation 6:

$$TCR (\alpha) = \frac{1}{\rho} \frac{d\rho}{dT} \quad \text{Equation 6}$$

where α is the TCR of the material, ρ is the resistivity and $d\rho$ is the change in resistivity of the material associated with a change in its temperature dT .

The resistivity of a material is given by Equation 7:

$$\rho = \frac{1}{ne\mu} \quad \text{Equation 7}$$

where n is the free carrier concentration, μ is the mobility of carriers and e is the charge of an electron.

There are two factors which may contribute to a change in the resistivity of the material with temperature as observed in Equation 7, namely, the free carrier concentration (n) and the mobility (μ). Metals show little change in the free carrier concentration as a function of temperature. However, the mobility of the charge carriers decreases with increasing temperature, resulting in a positive TCR, which is constant as a function of temperature. On the other hand, in the case of intrinsic semiconductors, both the free carrier concentration and mobility of the material changes with temperature, this usually results in a TCR which is negative. The resistivity of semiconductors changes as a result of thermally activated charge carriers across the band gap such that:

$$\rho = \rho_o \exp \left(\frac{\Delta E_a}{kT^2} \right) \quad \text{Equation 8}$$

where, ΔE_a is the activation energy, k is the Boltzmann's constant. Thus it follows that for a semiconductor, the TCR is given by:

$$\alpha = \frac{1}{\rho} \frac{d\rho}{dT} = -\frac{\Delta E_a}{kT^2} \quad \text{Equation 9}$$

Since all the work discussed in this thesis is based on uncooled infrared detection, T is taken to be room temperature (300 K) when reporting the TCR of a material.

Given this relationship, it is easy to calculate the theoretical TCR which can be achieved by using some common semiconducting materials such as silicon and germanium. For single c-silicon, the activation energy is roughly half of the band gap ($E_g/2$) and is equal to 0.55 eV, which results in a |TCR| of 7.2%/K. However, in the case of single c-germanium, whose activation energy is 0.335 eV, a |TCR| of 4.3%/K can be achieved. Although, higher TCR materials are desired, increasing activation energy (and therefore increasing bandgap) results in a decrease in the free carrier concentration; this results in high material resistivity (from Equation 7). Undoped crystalline silicon has a resistivity of $3.2 \times 10^5 \Omega\text{-cm}$, whereas crystalline germanium has a resistivity of 50 $\Omega\text{-cm}$. Unfortunately high resistivity materials tend to have higher noise [3] [18] [19] [20] [21] [22] [23] [24] [25] [26] [27], which is another figure of merit for a detector, as we will see in the subsequent sections. In addition, single crystal materials such as c-Ge are hard to integrate with standard MEMS fabrication protocol.

2.3.1.2. Electrical Noise

Device performance of microbolometers does not solely depend on TCR of the thin film. For example, although thin films of SiGe:H have $|TCR| > 5\%/K$, they inherently have higher resistivity and higher electrical noise. Electrical noise is an important limiting factor in the sensitivity of a semiconductor-based temperature sensor. An important figure of merit that relates thin film properties directly to the device performance is the Noise Equivalent Temperature Difference or NETD. In terms of the sensing material properties, the NETD can be derived [17]:

$$NETD \propto \frac{I_{noise, total}}{I_{bias} \times TCR} \quad \text{Equation 10}$$

where I_N is the noise current due to the thin film, I_{bias} is the bias current due to the applied voltage bias ($I_{bias} = \frac{V_{bias}}{R_b}$) and TCR is the temperature coefficient of resistance of the sensing material.

The ratio $\frac{I_{bias}}{I_N}$ is also known as the signal to noise ratio and is given by the ratio:

$$SNR = \frac{I_{bias}}{\sqrt{I_{noise, total}^2}} \quad \text{Equation 11}$$

where $I_{noise, total}$ is the total noise current due to the detector material and is comprised of mainly two components, the Johnson noise ($I_{noise, J}$) and the flicker noise or 1/f noise ($I_{noise, 1/f}$).

Johnson noise

Johnson noise is the electrical noise generated as a result of thermal agitation of carriers and is related to the resistance and the temperature of that resistor. Depending on the bias conditions, Johnson noise can manifest itself as either current noise or voltage noise. The current noise is given by [17]:

$$I_{noise, J}^2 = \frac{4k_b T (f_2 - f_1)}{R_d} \quad \text{Equation 12}$$

where, K_b is the Boltzmann's constant, T is the temperature of the bolometer, R_d is the resistance of the device, while the bandwidth of measurement extends from f_1 to f_2 . The voltage Johnson noise is given by [17]:

$$V_{noise, J}^2 = 4k_b T R_d (f_2 - f_1) \quad \text{Equation 13}$$

From the above two equations it can be seen that the Johnson noise is independent of the frequency but depends on the temperature and the resistance of the device as well as the bandwidth of measurement.

Equation 12 describes the current Johnson noise contribution to the detector signal. Due to the inverse relationship between the current Johnson noise and the detector resistance, the Johnson noise decreases with increasing device resistance. This inverse relationship allows for small Johnson noise contributions in constant bias bolometers even though high resistance thin films are used [18]. It is for this reason that

most bolometer designs use a voltage bias with current as the output signal. Further discussions on electrical noise will focus on current noise.

Flicker noise or 1/f noise

1/f noise is the fluctuation in conductance with a power spectral density proportional to $f^{-\gamma}$ where $\gamma = 1 \pm 0.1$ [28]. The current 1/f noise is given by empirical relationships proposed by F. N. Hooge [28]:

$$I_{noise, 1/f}^2 = I_{bias}^2 \frac{\alpha_H}{nVf} \quad \text{Equation 14}$$

Where I_{bias} is the bias current as a result of the applied voltage, V is the volume of the sample; f is the frequency range of measurement; α_H is Hooge's parameter; and n is the carrier concentration.. For a bandwidth of measurement between f_1 and f_2 , the corresponding 1/f noise becomes [3]:

$$I_{noise, 1/f}^2 = I_{bias}^2 \frac{\alpha_H}{nV} \int_{f_1}^{f_2} \frac{1}{f} df = I_{bias}^2 \frac{\alpha_H}{nV} \ln\left(\frac{f_2}{f_1}\right) \quad \text{Equation 15}$$

The two components, Johnson noise and 1/f noise, combine to produce a total mean square microbolometer current noise given by:

$$\overline{I_{noise, total}^2} = \overline{I_{noise, J}^2} + \overline{I_{noise, 1/f}^2} \quad \text{Equation 16}$$

Figure 2-4 shows an equivalent circuit diagram for a resistor which consists of an ideal resistance of value R_B and a current noise source in parallel with the ideal resistor.

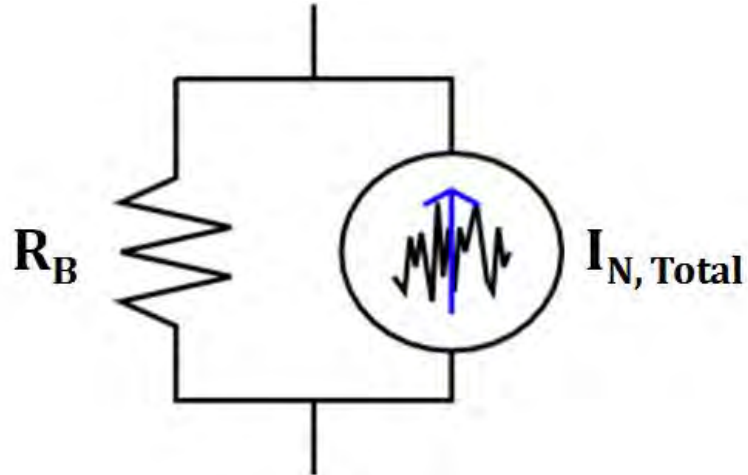


Figure 2-4. Noise equivalent circuit of a resistor for a 1-Hz bandwidth with an ideal resistance of R_B and an RMS current noise source $I_{N, Total}$ in parallel with the resistor.

2.3.2. Choice of Resistive Material

Figure 2-5 shows a plot of resistivity versus TCR of selected temperature sensitive materials which have been explored for use in infrared imaging [3] [18] [19] [20] [21] [22] [23] [24] [25] [26] [27]. These materials are metals, their alloys, semiconducting materials, and thermistor materials such as spinels of manganese, cobalt and nickel oxides.

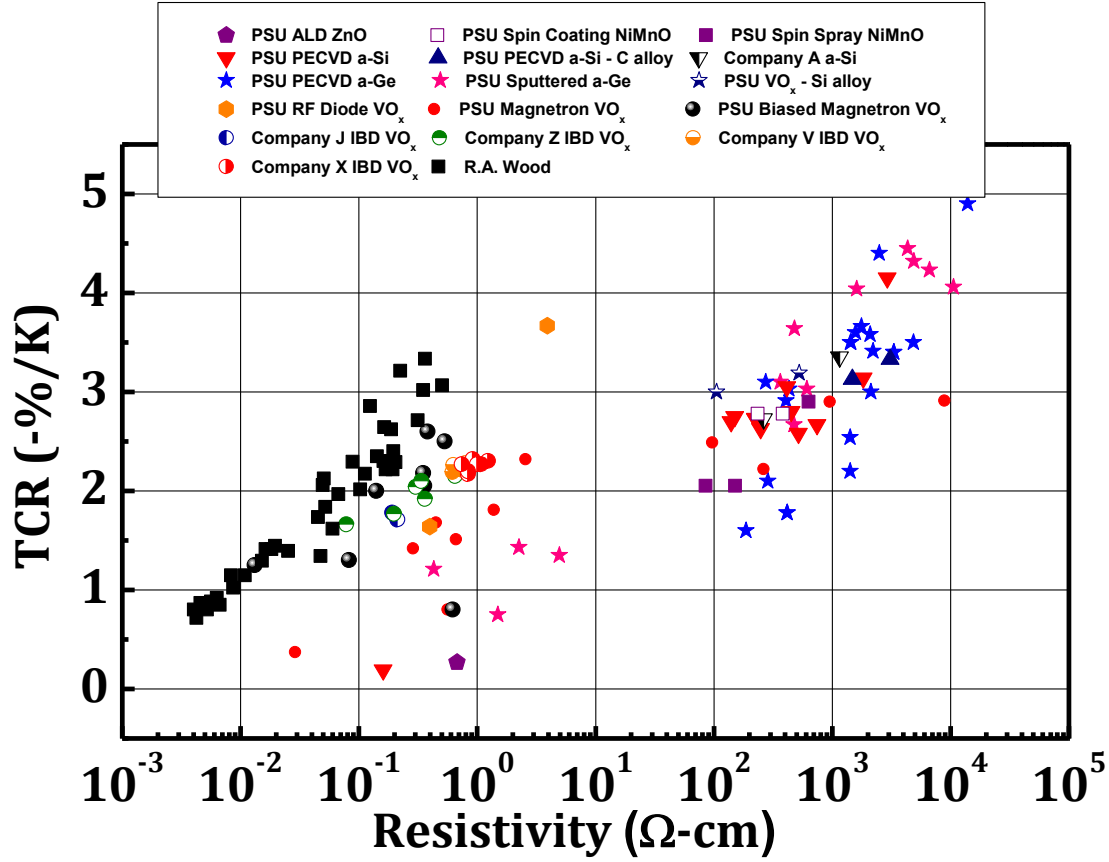


Figure 2-5. TCR vs. resistivity of various materials explored as candidates for temperature sensing [3] [18] [19] [20] [21] [22] [23] [24] [25] [26] [27].

2.3.2.1. Metals

In the low resistivity range of Figure 2-5, metals and alloys such as titanium (0.43%/K), platinum (0.18%/K) and Ni-Fe alloys (0.23 %/K) dominate [17]. Although metals and their alloys have low TCR values, their resistivity and therefore the inherent noise is extremely low, making them potential candidates for infrared imaging. In addition, processes exist for controllable, repeatable deposition of metal thin films. In fact, some of the first microbolometers were made using sputter deposited metals on Si_3N_4 membranes [3]. Because the resistivity of metals is low, very long serpentine resistors were fabricated to form the bolometer resistors [17]. Numerous metals and their alloys were explored as potential candidates; however in the early 1990s, semiconductor materials having five to ten times larger TCR replaced metals as the choice for bolometer materials.

2.3.2.2. Vanadium Oxide (VO_x) Thin Films

Most of the vanadium oxide microbolometer work was classified research and was kept secret until 1991, when Wood et al. at Honeywell Inc. filed a patent on the development of thin films of mixed phase vanadium oxides (VO_x) which had a TCR value of up to five to ten times higher than those of metals [8]. However, because of the United States International Traffic in Arms Regulations (ITAR) restrictions [33], the first public disclosure of the work, including details of materials and bolometer design was not published until 1994 by Wood et al. [8]. The performance of VO_x thin films achieved using the patented method was sufficient and surpassed other candidates for infrared imaging. The resistivity of these films was moderately higher than those of metals, at around 0.01 – 1 Ω-cm [8]. Thin films could be repeatedly deposited by ion beam sputtering at room temperatures on to commonly used substrates such as Si₃N₄ coated Si wafers [8] [30]. For these reasons, VO_x thin films have dominated the microbolometer industry in the 1990s to early 2000s [30]. All VO_x thin films were made either at Honeywell or were made using technology licensed from Honeywell [31] [32]. All literature, including the Honeywell patent, gave little to no description of the microstructure of the thin films obtained [8].

By the early 2000s, the underlying read out circuit technology had matured and the detector sensitivity had reached limits imposed by the electrical noise of VO_x thin films. To facilitate the development of VO_x thin films, the Pennsylvania State University was awarded a grant sponsored by the Army Research Office. One of the goals of the research initiative was to develop an understanding of the relationship between the electrical and microstructural properties of the VO_x thin films. In addition, alternate deposition methods were also explored to improve the throughput limitation imposed by ion beam deposition.

VO_x thin films can be deposited by various sputtering methods including ion-beam sputtering [3] [33] [34], RF sputtering [35], direct current (DC) [36] and pulsed DC sputtering [37] [38] [39]. However, films deposited by ion-beam deposition exhibited better film properties, i.e. higher TCR and lower 1/f noise for comparable resistivity values with other deposition techniques [23]. Most references to

industrially manufactured vanadium oxide thin-films for use in infrared imaging, to date, call for reactive ion-beam sputtering as the primary method of deposition [3] [8] [33] [34] .

Some of the first published work on developing an understanding between the structure–property relationships for VO_x thin films was done by Kerry Wells at the Pennsylvania State University by pulsed DC magnetron deposition of thin films of VO_x using a V₂O₃ target. Thin films deposited using this method resulted in films which were voided and mostly amorphous with some nano crystalline grain growth for thicker films [40]. It was also shown that different processing parameters such as, partial pressure of oxygen during sputtering and total sputtering pressure, produced films with different microstructure and electrical properties. In general, the resistivity and TCR of films was found to increase with an increase in the oxygen partial pressure, as well as with an increase in the total sputtering pressure. TCR values between –1 %/K and –3%/K were achieved; however the resistivity was orders of magnitude higher than those of films deposited by ion beam deposition [40].

Dr. Chandrasekaran Venkatasubramaniam investigated the use of metallic vanadium target for depositing microbolometer grade vanadium oxide thin films. Dr. Venkatasubramaniam characterized the inherent process hysteresis associated with the reactive pulsed Direct Current (DC) magnetron sputtering of the metallic vanadium target. Thus, thin films with resistivity and TCR values comparable to those of films deposited by ion beam deposition were grown [20] [41]. It was found that the room temperature resistivity of films increased with increase in total flow rate as well as with the increase in the oxygen partial pressure during sputtering [20] [42].

Films with good electrical characteristics (high TCR with moderately low resistivity) were deposited at low total flow rates and low oxygen partial pressures [20] [42]. These films showed the presence of nano-crystallites in an amorphous matrix in films, with high levels of porosity, which was confirmed by both transmission electron microscopy (TEM) and grazing incidence x-ray diffraction methods (GIXRD) [20].

Post deposition annealing experiments were also performed in oxygen and nitrogen environments in an attempt to improve the trade-off between TCR and resistivity. Films annealed in oxygen were driven towards higher oxides of vanadium, which have unacceptably high resistivity at room temperature. Annealing the thin films in nitrogen ambient yielded better results; for example, for films annealed at 300° C in nitrogen, the resistivity dropped by an order of magnitude, without significant deterioration of the film TCR. Structural analysis by XRD, Rutherford backscattering spectroscopy (RBS), Raman spectroscopy, scanning electron microscopy (SEM), TEM, and atomic force microscopy (AFM) did not reveal any significant changes between the annealed and the un-annealed films [20]. It was speculated that the improvement in thin film characteristics was due to reordering between the amorphous and nanocrystallite phases or due to grain growth. Nick Fieldhouse investigated the effects of substrate heating during reactive deposition of vanadium oxide thin films using a metallic vanadium target. The thin films obtained were mixed phase with VO and V₂O₃ crystallites in an amorphous matrix with moderate improvement in the film's electrical properties [42].

B. D. Gauntt extensively studied the microstructure-property relationships by altering processing parameters during pulsed DC magnetron deposition of VO_x thin films. It was found that all thin films deposited either by ion beam deposition or by pulsed DC sputtering resulted in one of three microstructures: an amorphous often voided columnar structure, a polycrystalline structure with nanometer-sized grains, or a nano-composite structure composed of columnar or conical nanocrystallites of vanadium oxide in an amorphous matrix. Gauntt concluded that thin films of VO_x exhibiting the best electrical properties were found to contain conical/columnar grains in an amorphous matrix and were deposited by ion beam deposition [43].

H. A. Basantani attributed the superior electrical properties of thin films deposited by ion beam deposition to the energetics associated with the process. To replicate the results with pulsed DC sputtering, substrate bias was applied during deposition. The electrical properties of the thin films deposited were superior (higher TCR with lower electrical noise) to those obtained with ion beam

deposition [37]. The films obtained were mixed phase with V_2O_3 nanocrystallites in an amorphous matrix. The x value in VO_x was between 1.5–2 [37]. In general, the microstructure of the thin films obtained was similar to the ones obtained with ion beam deposition; however these films had a higher density ($> 4.2 \text{ gm/cm}^3$ versus 3.8 gm/cm^3 for ion beam deposited thin films).

The best films of that work had a TCR of $-2.6\%/K$ with a resistivity of $0.6 \Omega\text{-cm}$ [37]. Attempts to increase the TCR further resulted in an abrupt increase in the resistivity which was not of interest for that work [44]. Venkatasubramaniam and Gauntt explored the parameter space during deposition by pulsed DC magnetron sputtering and obtained high TCR VO_x thin films having very large resistivities [20] [21]. Figure 2-6 compares the electrical properties of VO_x thin films deposited by pulsed DC magnetron sputtering and ion beam deposition from numerous references [3] [33] [42] [37]. It is interesting to note that although the obtainable range of TCR is between $-0.2\%/K$ and $-5\%/K$, there are two ranges of resistivity between 10^{-3} to $1 \Omega\text{-cm}$ and 10^3 to $10^5 \Omega\text{-cm}$. At the time of writing this dissertation, thin films having intermediate resistivity between $1 \Omega\text{-cm}$ and $10^3 \Omega\text{-cm}$ have not been successfully deposited.

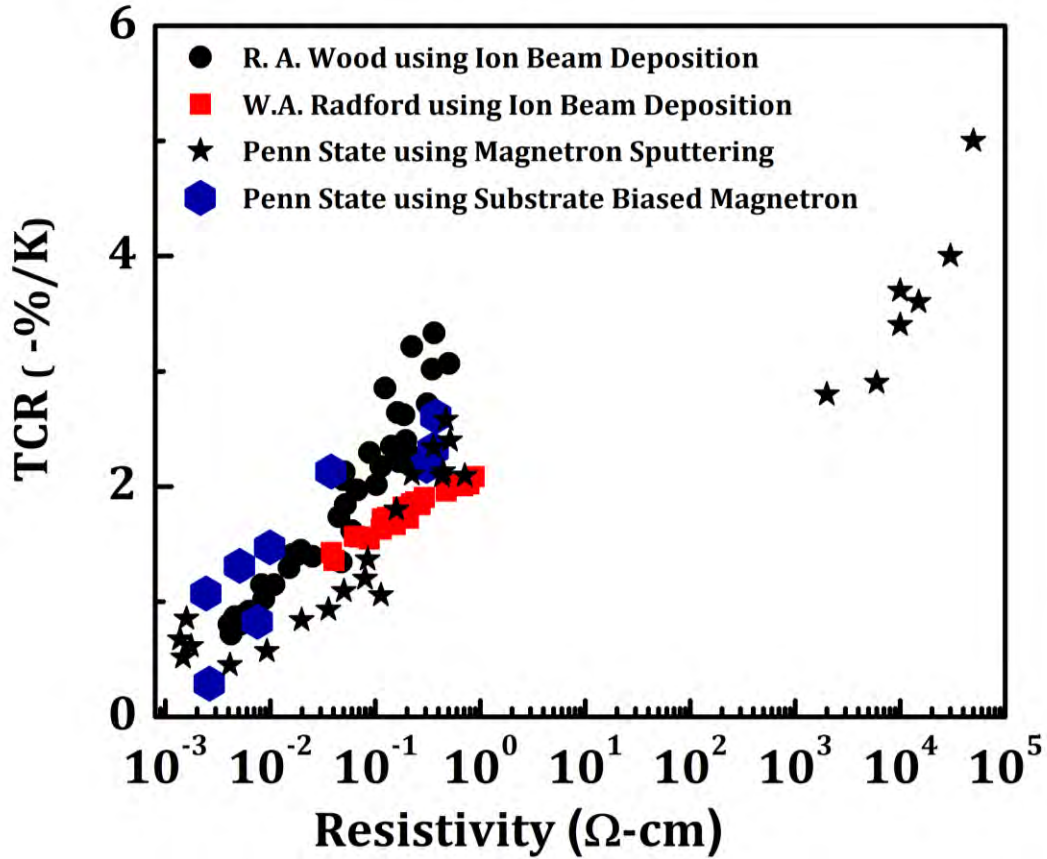


Figure 2-6. Comparison of Resistivity vs. TCR of VO_x thin films deposited by ion beam sputtering [8] [33] and magnetron sputtering [37].

There are fundamental differences between VO_x thin films belonging to the two distinct resistivity ranges. While thin films having resistivity between $10^{-3} \Omega\text{-cm}$ and $1 \Omega\text{-cm}$ are mixed phase, films with higher resistivity and high TCR are x-ray amorphous [21] [37]. The high resistivity films typically have x-values in VO_x between 2 – 2.5, compared with 0.8 – 2 for films with resistivity $< 1 \Omega\text{-cm}$ [45]. The resistivity and the inherent $1/f$ noise of thin films with $|\text{TCR}| > 4\%/K$ was found to be too high for use in existing read out circuit technology at the time [3].

Both deposition techniques, ion beam deposition and magnetron sputtering, are limited in deposition rates to $\sim 1 \text{\AA/s}$ [44] [46]. Deposition rates in ion beam deposition is limited by ion current density of the ion source, whereas in magnetron sputtering the deposition rate is limited by the process

window associated with reactive deposition and therefore the throw distance associated with the reactive deposition [42].

In order to increase through-put, industry is looking for alternate deposition techniques that would result in higher deposition rates. One such candidate is the biased target ion beam deposition which is capable of achieving deposition rates $> 10 \text{ \AA/s}$. VO_x thin films deposited by this deposition technique were investigated in this work [47].

2.3.2.3. Hydrogenated Silicon Germanium Alloys ($\text{Si}_{1-x}\text{Ge}_x\text{:H}$)

A considerable research effort has been made in the development of thin films of amorphous hydrogenated silicon (a-Si:H) and hydrogenated silicon germanium alloys ($\text{Si}_{1-x}\text{Ge}_x\text{:H}$) for use in large area devices such as solar cells, liquid crystal displays and most recently as sensing material for infrared detection [48] [49] [50]. In particular, alloys of Si and Ge have been heavily investigated because the optical band gap of the deposited material can be tailored between 1.1 eV and 1.7 eV depending on the composition of the alloy. However, the success in developing SiGe alloys for microbolometer applications having superior electrical properties has been rather limited.

Although VO_x thin films have been demonstrated to be useful microbolometer TCR materials, their maximum TCR is limited to about $-5\%/K$. Mark Unewisse and Jean Tissot in 1996 demonstrated amorphous hydrogenated silicon–germanium (SiGe:H) thin films having TCR values larger than those of VO_x , around $-2.5\%/K$ to $-8\%/K$ [50] [50]. Although TCR values as high as $-8\%/K$ were attainable, Liddiard et al. concluded that the electrical properties were accompanied by unacceptably high $1/f$ noise [17].

An analogous material system lying on the other extreme of the spectrum, consisting of amorphous hydrogenated germanium (a-Ge:H), has also been investigated [51] [52] [53] [54] [55]. However, these thin films could not compete with the performance of Si:H/SiGe:H systems for photovoltaic or thin film transistor applications. While Si:H and SiGe:H have dark resistivity between

$10^{11} - 10^{13} \Omega\text{-cm}$ with light resistivity as low as $10^4 \Omega\text{-cm}$, Ge:H thin films show smaller dark resistivity of $10^7 \Omega\text{-cm}$ with smaller thermal activation [49] [52] [53] [54] [55]. However, the lower resistivities of Ge:H thin films make them good candidates for further investigation as infrared imaging materials.

Electrical properties of hydrogenated germanium have been investigated for over three decades. Numerous research groups have demonstrated thin films of amorphous Ge:H having $|\text{TCR}|$ as large as 5%/K and having resistivity of the order of $10^5 \Omega\text{-cm}$ [51] [52] [53] [54] [55] 4]. Campinas et al. studied the effect of deposition conditions on the electronic quality of a-Ge:H and a-Ge thin films deposited by RF sputtering [53]. Plasma enhanced chemical vapor deposition (PECVD) technique which had proved to be very effective in producing a-Si:H thin films, was also used to deposit Ge:H. The highest $|\text{TCR}|$ obtained was 4.6 %/K with a resistivity of $10^5 \Omega\text{-cm}$ [55].

Ambrosio et al. demonstrated thin films of a-Ge:H and a-SiGe:H, deposited using GeF_4 diluted in H_2 having $|\text{TCR}|$ as high as 5%/K with moderately low resistivity of $20,000 \Omega\text{-cm}$ [56]. These publications contained no information on the underlying microstructure or the inherent $1/f$ noise properties of the films obtained. Further improvements on the electrical properties came in 2012, when Moreno et al. published information on polymorphous thin films of Ge:H [57].

In the work by Moreno et al., growth of nanocrystallites was encouraged by varying the total pressure of deposition from 600 mTorr to 2500 mTorr [57]. Cross sectional TEM of the thin films revealed that the films contained nanocrystals of size 2–4 nm in an amorphous matrix [57]. As a function of pressure, Moreno claimed that the grain size grew and its value reached a maximum at around 2,000 Torr before decreasing for 2.5 Torr [57].

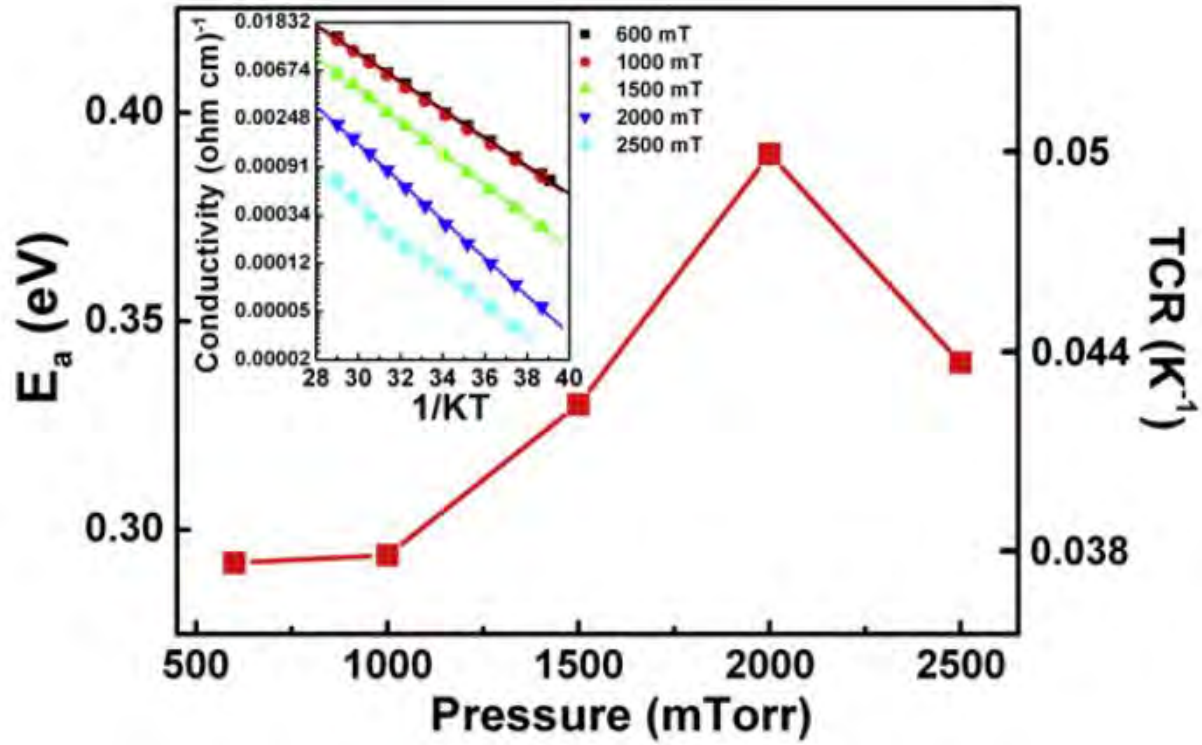


Figure 2-7. Graph showing the effect of total deposition pressure on TCR and resistivity of deposited pm-Ge:H thin films from ref [57].

Figure 2-7 shows the resistivity and TCR data of deposited thin films as a function of deposition pressure from reference [57]. Thin films deposited in this work showed $|TCR|$ between 3.8 %/K and 5 %/K with resistivity between 1,100 $\Omega\text{-cm}$ and 20,000 $\Omega\text{-cm}$ [57]. This resistivity – TCR tradeoff was amongst the best reported in the literature for thin films of hydrogenated germanium [57]. No 1/f noise properties were reported for these thin films.

Around the same time Saint-John et al. also investigated if the electrical properties of the Ge:H thin films can be improved by introducing small amounts of nanocrystalline Ge:H material during the natural growth evolution [51] [19]. It was hypothesized that addition of nanocrystalline germanium, which has a resistivity of 50 $\Omega\text{-cm}$, would help reduce the resistivity and the electronic noise while keeping the high TCR associated with the amorphous Ge:H material [57].

The dilution ratio (given by $R = [H_2]/([GeH_4] + [H_2])$) used during PECVD is an important parameter in the nucleation of crystallites [19] [51]. Similar to PECVD deposition of Si:H and SiGe:H

thin films, thin films of Ge:H also show a decrease in the thickness of amorphous bulk layer prior to the nucleation of crystallites [51] [58]. Figure 2-8 shows the skeletal growth evolution diagram which was developed by Saint-John for Ge:H, similar to the microstructural evolution associated with PECVD deposited Si:H, to confirm the location of the transition regions between amorphous, amorphous and nanocrystalline, and nanocrystalline microstructures [19].

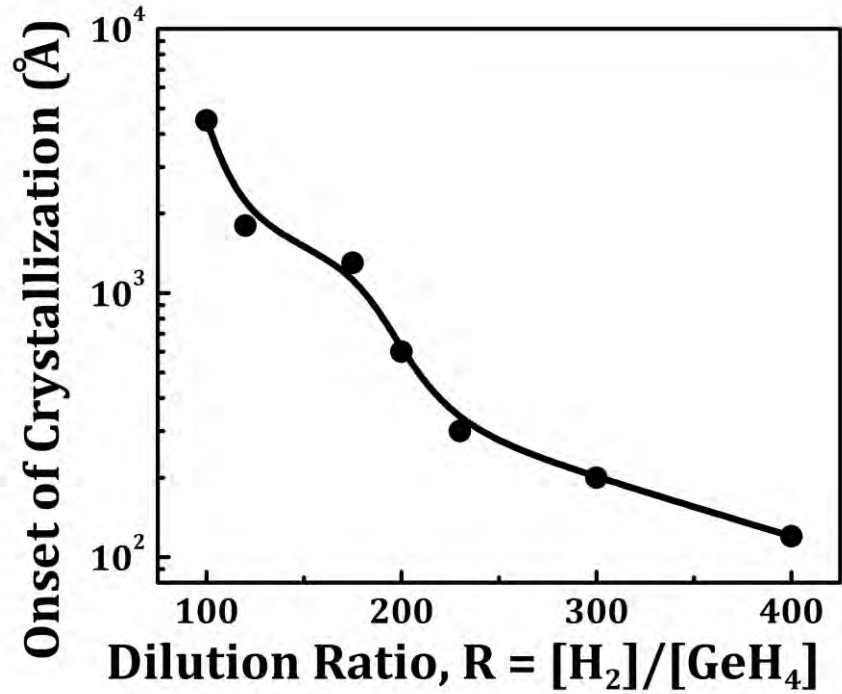


Figure 2-8. Growth evolution diagram for Ge:H thin films grown on native oxide on c-Si showing the thickness values at which crystallization becomes evident (re-plotted from ref [19]).

By depositing thin films at different dilution ratios of the growth evolution diagram, Saint-John's work aimed to assess the electrical property of the thin films as a function of microstructure. Figure 2-9 summarizes the electrical properties of thin films obtained in that work [19].

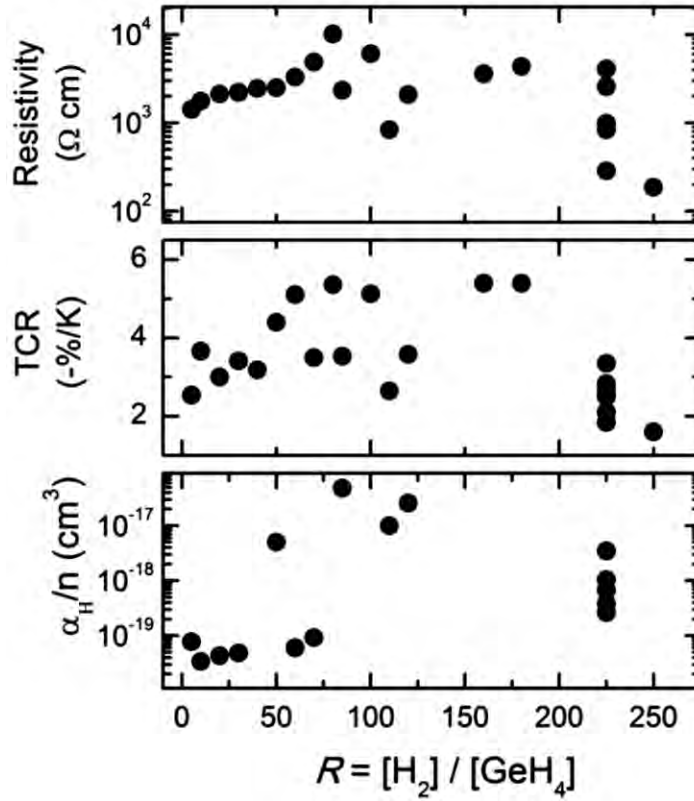


Figure 2-9. Summary of electrical properties (resistivity, TCR and normalized Hooke's parameter) for thin films of Ge:H thin films deposited at different dilution ratios [19].

TCR values between -2 %/K and -5 %/K were obtained with resistivity between 10^3 Ω -cm and 10^4 Ω -cm and α_H/n values between 10^{-20} and 10^{-17} cm^3 [19]. However, no obvious trend in the electrical properties could be inferred as a function of R . Part of the reason could be that there are several factors involved. For example, the plot compares electrical properties of films having different thicknesses and therefore different microstructures. Thus it is hard to get a true sense for a relationship between the microstructure and electrical properties.

Figure 2-10 shows the electrical properties of thin films as a function of crystal fraction obtained by growing thin films of increasing thicknesses at a dilution ratio of $R = 225$. Saint-John noticed a decrease in the resistivity for small crystal fractions following which both the resistivity and TCR increased while α_H/n values remained around 10^{-18} cm^3 [19]. The largest TCR value of -3.5 %/K was obtained for the thin film with a crystal fraction of 55 % for a film thickness of 200 nm [19]. Thin films

with larger crystal fractions were not deposited in this work, and so it is unclear if larger TCR values could be obtained for films with higher crystal fractions.

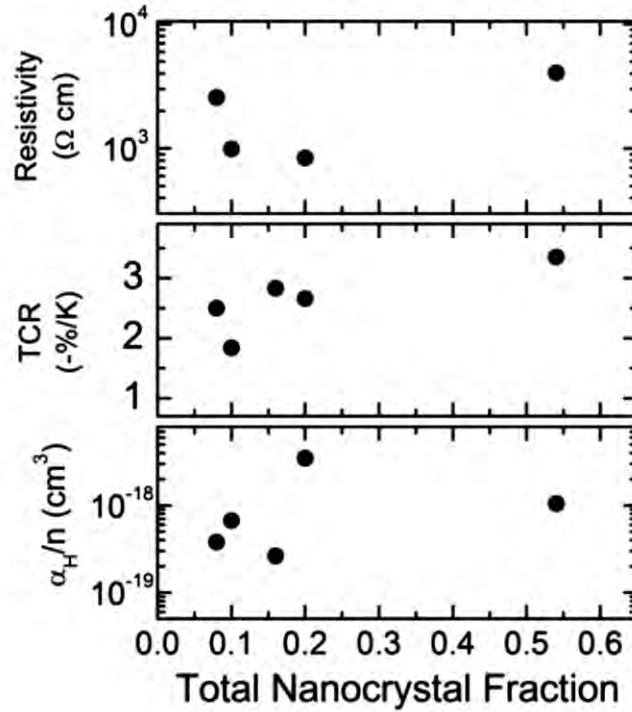


Figure 2-10. Electrical properties of (a+nc)-Ge:H thin films grown at $R = 225$ for increasing thicknesses. The x-axis plots the total nanocrystalline fraction as it relates to the thickness [19].

Saint John noted that to obtain thin films with a larger crystal fraction for a dilution of $R = 225$, thin films must be thicker than 200 nm [19]. However, for bolometric applications, these thicker films have an unacceptably high thermal mass, thereby limiting the bolometer's performance.

To induce grain growth at small thicknesses, Saint-John observed the microstructural evolution in thin films deposited at a much higher dilution of $R = 400$. Figure 2-11 shows the microstructure of a 200 nm thick thin film deposited on to native oxide on c-Si [19]. Saint-John observed that thin films deposited at this dilution were dense and the microstructure was nanocrystalline with planar twinning defects on the order of ~ 1 nm [19]. Despite the unique microstructure, the films were not characterized for their electrical properties because they were not deposited on insulating substrates.

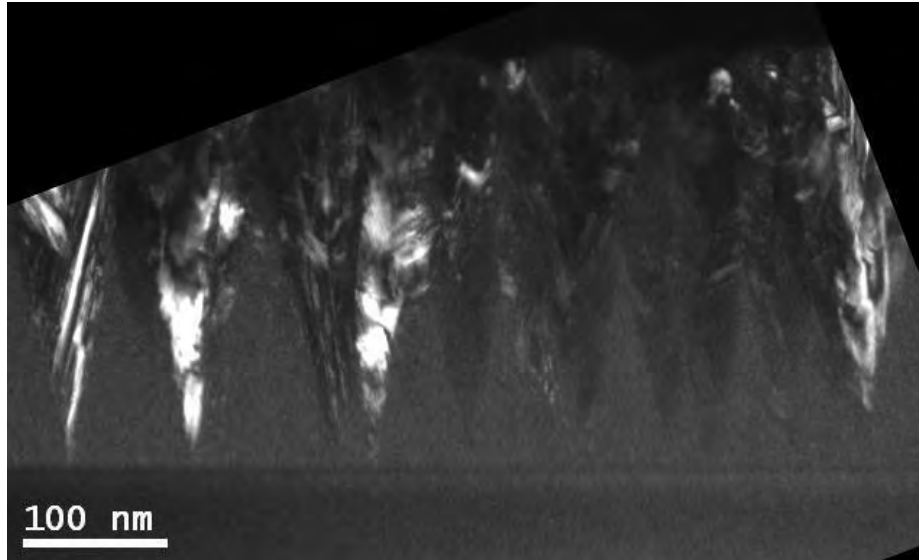


Figure 2-11. Cross-sectional TEM dark field image of an R = 400 (a+nc)-Ge:H thin. The amorphous regions are uniformly illuminated, while the crystalline regions appear light or dark depending on their orientation. Two of the approximately ten discernible cones are oriented such that twinning can be seen [19].

Saint John also observed the surface roughness evolution of thin films deposited at various dilutions and related it to the microstructural evolution of a growing thin film. He observed that for thin films deposited at higher dilutions, the surface roughness increased rapidly and at lower thicknesses, indicating a faster transition from an amorphous to an amorphous + nanocrystalline material [19]. He also observed that the roughness peaked at smaller thicknesses and then decreased. The peak in roughness was attributed the value of film thickness at which the grains coalesced and the film became predominantly nanocrystalline [19].

Saint John also observed that further acceleration of the microstructural evolution is made possible by lowering the substrate temperature used during deposition [19]. Figure 2-12 shows the surface roughness evolution of Ge:H thin films deposited at substrate temperatures of 140 °C, 200 °C and 260 °C [19]. The thin film deposited at 140 °C showed a prompt coalescence at a thickness of 85 nm [19].

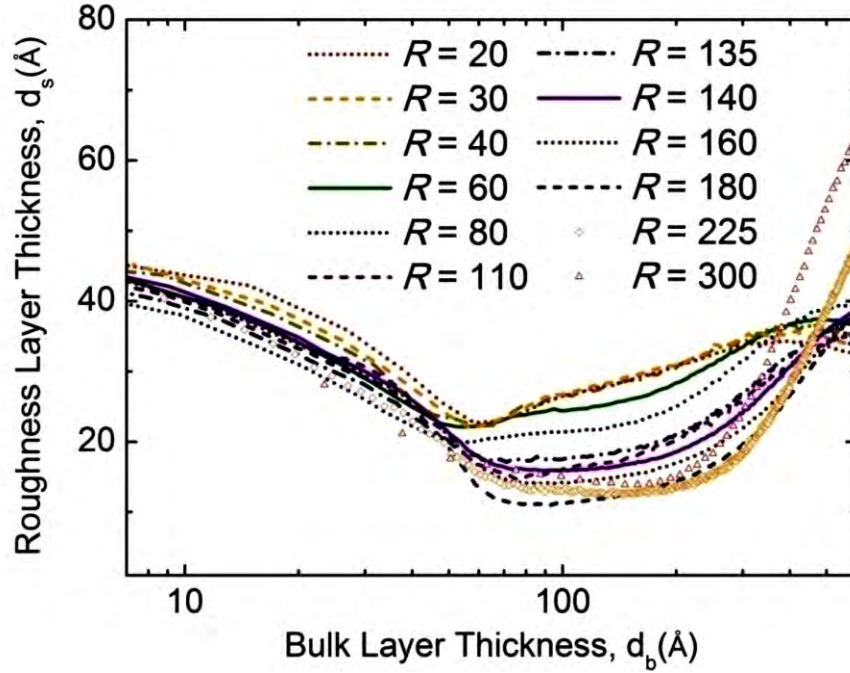


Figure 2-12. Surface roughness evolution for Ge:H films deposited at different dilution ratios, R . Higher dilution ratios show an increase in surface roughness at smaller thicknesses, indicating film transformation from amorphous to a mixed phase thin film ref. [19].

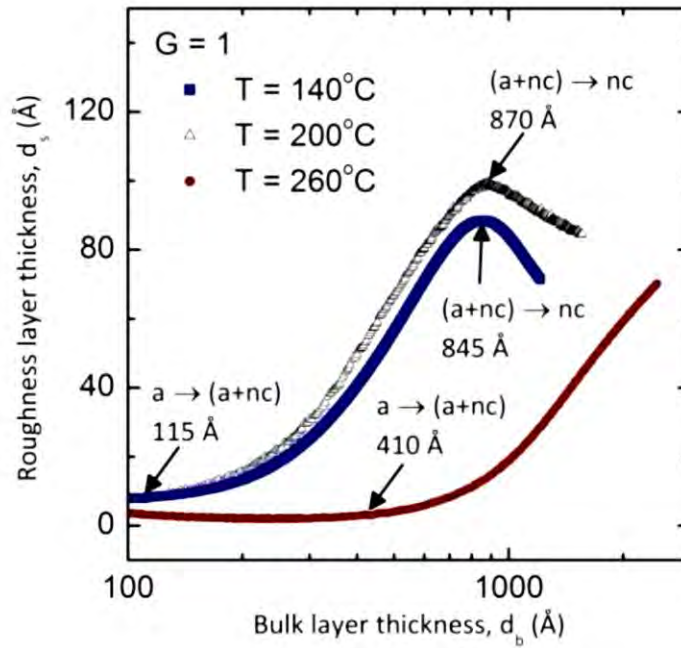


Figure 2-13. Surface roughness evolution for films deposited at increasing substrate temperatures on to SiN_x substrates on c-Si. Lower substrate temperatures result in a quicker decrease in roughness, indicating a more a more prompt coalescence [19].

2.3.3. Comparison of Material Performance

The total noise due to the sensing thin film depends on the bias current, but can be calculated based on values known from the industry [18] [19]. Due to their lower resistance, thin films of VO_x are pulsed biased with a current of $\sim 10 \mu\text{A}$. SiGe:H thin films, which have a much higher resistance in comparison, are biased using a constant current of $\sim 40 \text{ nA}$. The noise contribution of the two material systems can then be calculated from the above equations and have been summarized in Table I below.

Table 1 lists relevant thin film parameters and the calculated noise current in VO_x and SiGe:H thin films.

Table 1. Parameters for commonly used IR imaging layers [17] [18].

Parameter	Value (VO_x Thin Film)	Value (SiGe:H Thin Film)
Resistance (T_{room})	100 K Ω	> 100 M Ω
Bias Current (I_{bias})	10 μA	40 nA
Bandwidth (B)	15 KHz – 0.0001 Hz	7.8 KHz – 0.0001 Hz
TCR (α)	–2.4 %/K	–3.9 %/K
Normalized Hooge' Parameter (α_{H}/n)	10^{-21} to 10^{-23} cm^3	10^{-18} to 10^{-20} cm^3
Thickness	50 nm	50 nm
Cell Area	17 $\mu\text{m} \times 17 \mu\text{m}$	17 $\mu\text{m} \times 17 \mu\text{m}$
Johnson Noise	50 pA	1 pA
1/f Noise	0.072 nA to 7.2 nA	21 nA
Total Noise	75 pA to 7.2 nA	21 nA

It can be seen that SiGe:H thin films can have lower Johnson noise values, yet much higher 1/f noise in comparison with VO_x thin films. Recent advances in the underlying read out integrated circuits (ROIC) have made a-SiGe based thin films competitive for use in microbolometer devices, as shown in the following section.

2.3.4. Readout Circuits used in Infrared Imaging Focal Plane Arrays

As it can be seen from Table 1 above and Figure 2-3, there are many deposition techniques and numerous materials that can yield thin films that can be used as sensing materials in infrared imaging. Thin films of VO_x, and SiGe:H have all been used for infrared imaging, yielding similar device performances [9] [18]. This begs the question, how can materials having orders of magnitude difference in resistivity and five to ten times difference in TCR result in similar sensitivity of the fabricated microbolometer array? The answer lies in the resistivity of the material and the underlying readout circuitry associated with that resistivity.

2.3.4.1. Low Resistivity Materials and Pulse Biasing

In the case of materials with resistivity < 1 Ω-cm, the device resistance is typically < 10⁵ Ω. When a bias is applied to the thin film resistor on a substrate membrane of SiN_x, the film undergoes Joule heating which leads to a rise in temperature at a rate of [3]:

$$\Delta T = \frac{V_{bias} I_{bias}}{c} \quad \text{Equation 17}$$

where c is the thermal capacity of the detector. For a bias of 1 Volt this results in the rate of rise of temperature of 50,000 °C/second. To avoid a large rise in temperature, the bias time is limited to about 100 μsec, which limits the temperature rise to about 5 °C [3]. Following the pulse duration, the detector is left unbiased for 29.8 msec such that the thin film cools and reaches the substrate temperature and is ready for the next bias pulse [3]. The total pixel readout time is 30 msec which results in a frame rate of ≈ 30 Hz [9] [3].

Figure 2-14 shows the schematic of the Readout Integrated Circuit (ROIC) developed at FLIR Inc. to multiplex a VO_x based bolometer array [59]. The entire array is read in batches of 20 × 128 devices at a time with 8 channels to read out the entire array of 160 × 128 [59]. Each channel contains an on-chip bias compensation to provide a uniform output over a wide range of operating temperatures. This allows the operation of the bolometer without the need for thermoelectric cooler stabilization [59].

The pulse biasing scheme described above has been used for low resistivity materials such as VO_x and metallic thin films such as permalloy (Ni-Fe) and titanium.

2.3.4.2. High Resistivity Materials and Constant Biasing

For materials with high resistivity ($> 1,000 \Omega\text{-cm}$), the pulse bias method is not necessary and in fact limits the sensitivity of the bolometer array. As discussed in the previous sub-section, these high resistivity materials have a high TCR but also high $1/f$ noise. For thin films belonging to the SiGe:H material system, the ' α_H/n ' value is around 10^{-20} cm^3 ; as seen in Table 1 this leads to a $1/f$ noise value of 20 nA, a value roughly half that of the current signal. At these noise levels, it would be impossible to manufacture bolometer arrays with sensitivities anywhere close to those achieved by low resistivity material.

In the early 2000s, Level-3 Communications designed a unique ROIC which allowed for a dramatic reduction in noise by averaging the continuously biased signal [60]. The ROIC technology contains an in-pixel bias subtraction as well as an in-pixel switched capacitor filter/integrating amplifier to maximize signal integration and signal gain and enables simultaneous signal integration on every pixel [60]. Hanson et al. claim that the novel ROIC design enables the possibility of increasing the array size by adding rows, does not impact the array performance and theoretically allows for multi-megapixel sized FPAs with high performance [60]. A simplified version of the unit cell switched capacitor filter integrating amplifier design is shown in Figure 2-15 [60].

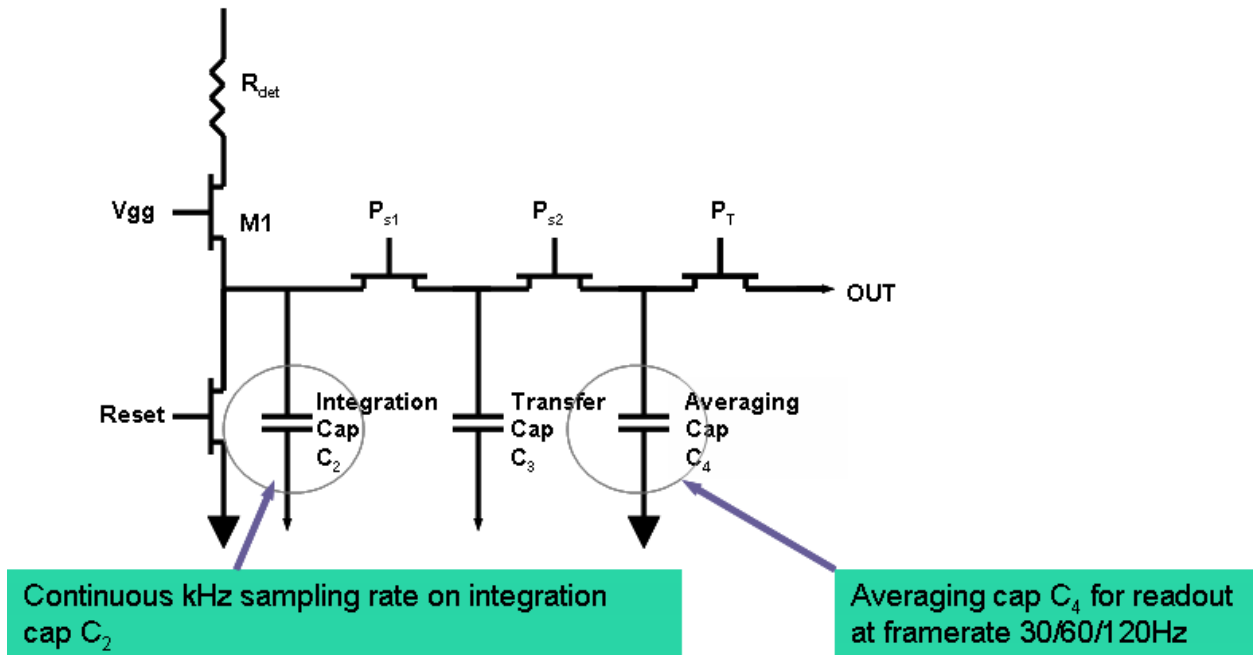


Figure 2-15. Schematic of the L-3 EOS switched capacitor filter/integrating amplifier integrated in the unit-cell of each pixel as in ref [60].

The operation of the readout circuit has been described in ref [60]: in Figure 2-15, the detector pixel is represented by a resistor (R_{det}). Detector signal current is injected through the input field effect transistor (FET M1) by biasing its gate V_{gg} . The detector current is sampled continuously on the integrating capacitor C_2 at a rate of ~ 7.8 KHz. The continuously sampled current signal is filtered by the switched capacitor filter network through a transfer capacitor C_3 and averaged on capacitor C_4 . It is at this capacitor, C_4 , where the signal is averaged and the $1/f$ noise reduced. For example, for a desired frame rate of 60 Hz, the sample can be averaged over 130 times resulting in $1/f$ noise reduction by a factor > 11 . The processed signal on capacitor C_4 is sampled and read out at the desired frame rate. Hanson points out that the FPA sensitivity is not dependent on frame rate but rather on the KHz rate at which signal is integrated on C_2 . Although a high integration frequency would help further reduce $1/f$ noise, the Johnson noise value would then increase. The sweeping frequency is chosen in a way that $1/f$ noise and the Johnson noise contribution is minimized. The filter network is chosen such that the noise bandwidth is significantly lower than the Nyquist frequency. The noise bandwidth is substantially lower than the filter Nyquist frequency.

Hanson claims that for the above mentioned reasons, L-3 ROIC's performance is independent of frame rate making frame rates of 60Hz, 120Hz, and beyond achievable without performance loss [60].

Chapter 3. Experimental Methods

3.1. Deposition of VO_x Thin Films: The LANS Biased Target Deposition System

Thin films of VO_x were deposited by a novel sputtering technique known as Biased Target Ion Beam Deposition (BTIBD) or simply Biased Target Deposition (BTD) (manufactured by 4Wave Inc. based in Sterling, VA).

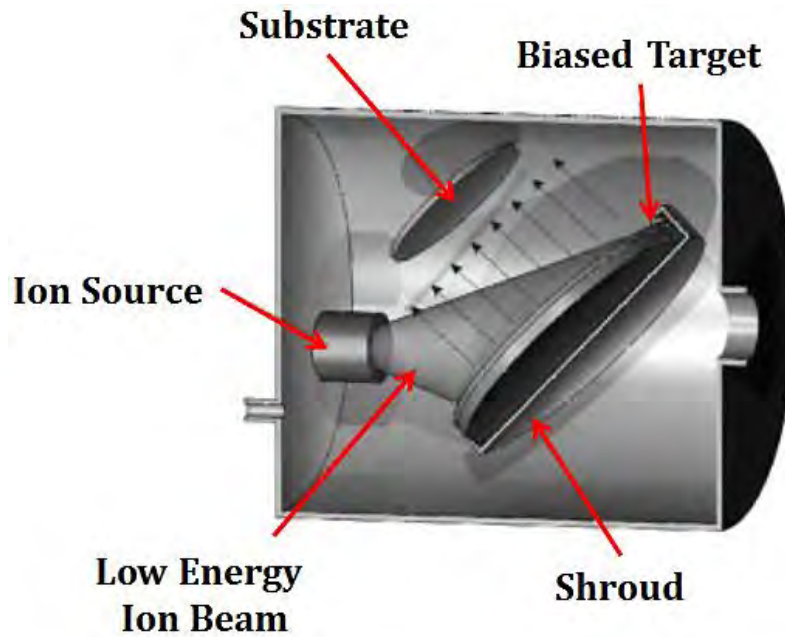


Figure 3-1. Concept sketch of Biased Target Ion Beam Deposition system [61].

A concept sketch of this technique can be seen in Figure 3-1 [61]. The operation principle of the technique has been discussed elsewhere and is summarized [47]: In this deposition technique, a low energy, broad beam ion source (Energy of ions < 25 eV) is used to illuminate the target. No attempt is made to focus the ion beam on to the target material. The ion energy of the beam is low compared (< 40 eV) and so the sputter yield of materials in the chamber from this beam is minimal.. Once a stable ion beam has been established, a negative bias is applied to the target. This negative bias establishes a sheath in front of the target which accelerates the positively charged ions from the ion beam to cause sputtering.

The deposition system used in this work is detailed in Figure 3-2. This system is sold as the LANS BTIBD tool. In this geometry, the low energy ion-beam producing ion gun is facing the substrate and illuminating three targets. Targets are biased using a single programmable pulsed DC power supply source. The pulsed DC power source is connected to the three targets in parallel configuration to allow for simultaneous sputtering of up to three targets. Therefore the control of adatom arrival rate and the adatom energies is accomplished threefold by:

1. Sputter yield is controlled by the ion current established by the ion source.
2. Sputtering rate is additionally controlled at each target by controlling the pulse frequency and the duty cycle.
3. The adatom energy is decided by the operating pressure. .

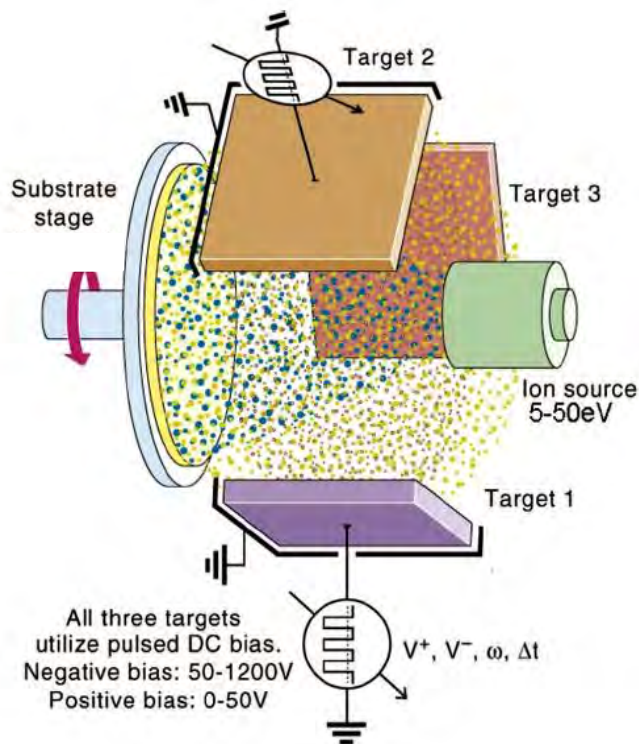


Figure 3-2. Schematic of the Laboratory for Alloying and Nano layer Sputtering by the 4Wave Inc. used in this work [62].

3.1.1. Ion Source used in BTB: Broad Beam, Gridless Ion Sources

A broad-beam ion source is defined as a beam of ions whose diameter (length of transverse direction) is much larger than the physical dimensions of its optics or the Debye length of the accelerating voltage [63]. These sources are much more interesting as ion sources for thin film processing applications than other types such as Von Ardenne type ion source (mainly used for high energy thin beam of ions carrying high energy and multiple charges), Electron Cyclotron Resonance Type (ECR) ion sources, electron beam ion sources, laser ion sources and vacuum arc ion sources. Broadly speaking, there are two types of ion sources commercially used in thin film processing, gridded and gridless type [63]. The fundamental difference between the two types of sources is that while gridded ion sources produce ions with a narrow energy distribution, gridless ion sources produce ion beams that are unfocused and have a broad energy distribution [63] [64]. This section is aimed at discussing the fundamental theory of operation of the ion source in the context of this work.

The Hall-current ion sources operate on the principle of significantly increasing the plasma's electrical resistance and the electron lifetime in the plasma using a magnetic field [63] [64] [65]. The increased electron lifetime allows for an increase in the interaction time of the electrons with the neutral atoms/working gas which is being expelled from within the ion source.

In the ion source discharge channel, the electrons are magnetized. If ω_e is the electron cyclotron frequency and τ is the average time between collisions with other particles and the chamber walls, then $\omega_e \tau \gg 1$ [61] [63] [64]. These magnetized electrons move from their source of origin (cathode/electron source) to the anode (ion source discharge channel) in a helical path prescribed by the electrical and magnetic fields. Under optimum conditions, the ions are usually not magnetized, i.e. $\omega_i \tau \ll 1$ (where ω_i is the ion cyclotron frequency in the magnetic field and τ is the average time between the ion collisions with other particles and the chamber walls) [61] [63] [64]. The ions move between their source of origin (anode discharge channel) and the cathode along the electrical field. During this path, the plasma picks up

the necessary number of electrons for neutralization, resulting in a quasi-neutral beam of ions and electrons known as the ion beam [61] [63] [64].

Unlike in gridded ion sources where the ion beam experiences space charge limitations due to limitations imposed by Child's law, the Hall-current sources do not have any limitation for the ion beam current that can be extracted [63].

Schematics of the geometry and the electrical circuit of the most popular type of ion source are shown in Figure 3-3a and Figure 3-3b. A detailed description of the operation of the ion source can be found in reference [61] but is briefly discussed here: Figure 3-3b shows the electron emission from the cathode is controlled by the use of an AC power supply connected to the electron source. The anode potential is determined by the anode current, the magnetic field strength and the gas flow. The power supply to an electromagnet impresses a variable magnetic field on the electrons being emitted from the cathode. For a known regime of operation, a permanent magnet can replace the electromagnet, thereby eliminating the use of an extra power supply. A mass flow controller is used to control the amount of gas being introduced into the system, and thereby control the conductivity of the plasma. This gas flow dictates the discharge voltage of a particular ion beam discharge current. The cathode used in normal operation is either a filament type or a hollow cathode type.

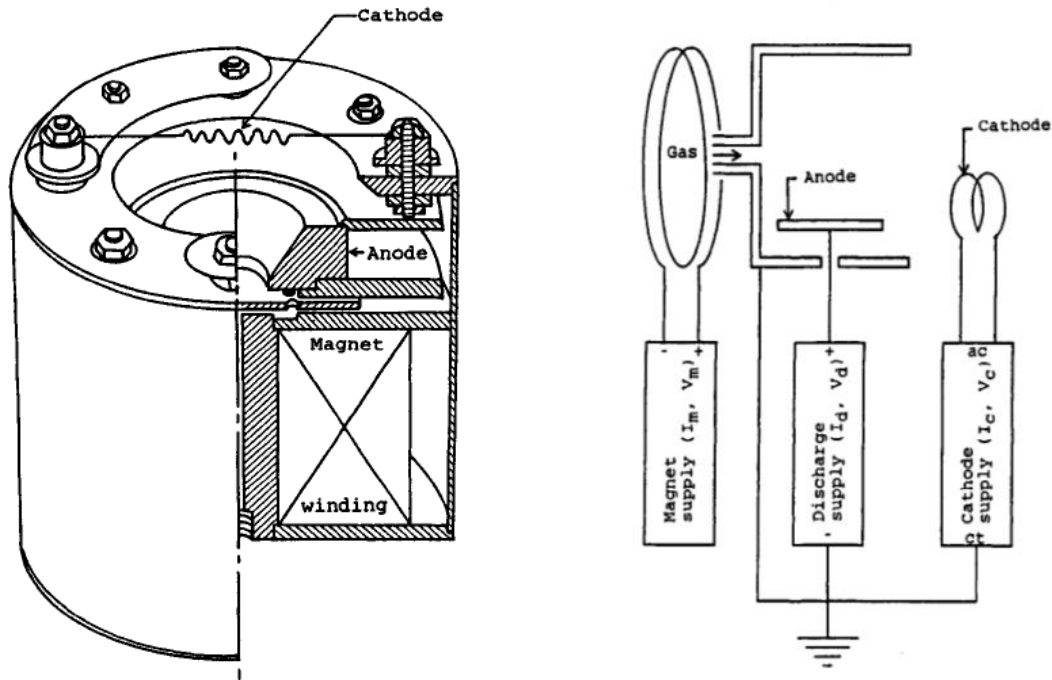


Figure 3-3. Schematic of a) Cross-section of one of the first ion sources, b) Electrical diagram of a basic ion source as it appears in ref. [64].

3.1.1.1. Ion Generation Mechanisms

The operating principle and various processes of the anode are discussed as follows and are pictured in Figure 3-4. The neutral atoms/gas molecules are introduced using a mass flow controller (1). Electrons (2) generated at the cathode, crossed between electric field and magnetic field lines follow the path given by (3) in a helical manner towards the discharge chamber of the anode. These electrons strike the neutral atoms/molecules (4) and ionize them (5). A combination of electrons (2) and ions (5) forms the plasma which is directed downstream by the radial and axial components of the electric field as well as a gas distributor/reflector.

Due to the conical axisymmetric shape of the discharge chamber and the positive charge enforced on the anode, the ions that are created near the discharge chamber are accelerated away from the anode in the axial direction. The velocity acquired by these ions and the positive potential on the other side of the axis forces the ions to crisscross the axis multiple times and undergo several collisions [66]. The positive space-charge and the current due to the ions are neutralized by electrons generated from the electron gun

(7). These processes result in a divergent, neutral beam comprised of ions (6) and electrons (7) of ions being generated and directed downstream from the discharge chamber.

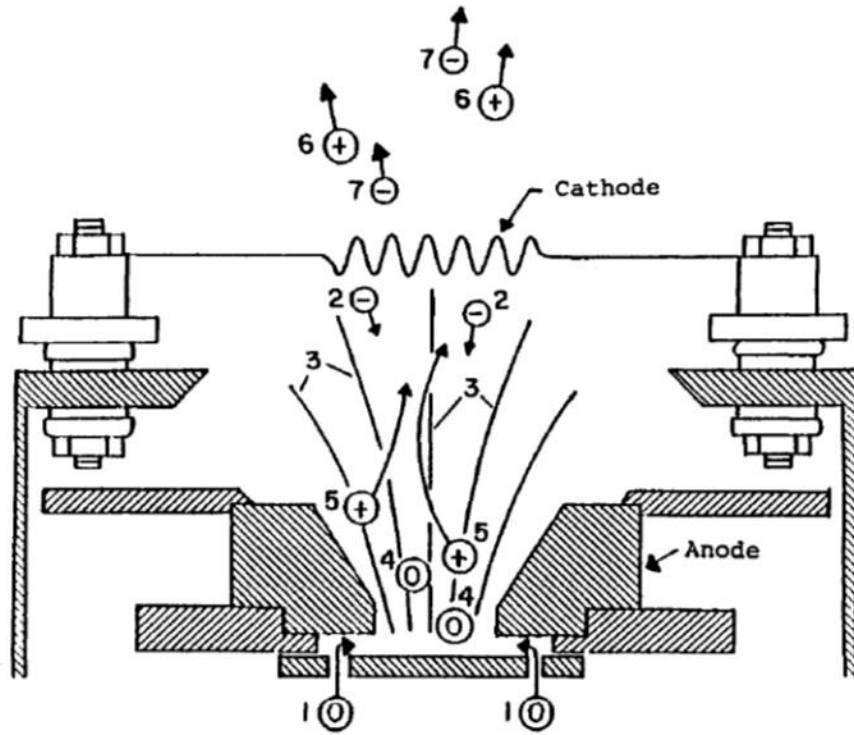


Figure 3-4. Various processes in an end-Hall ion source [66].

It should be noted that discharge current of the anode and the cathode does not equal the electron and ion currents in the quasi-neutral beam. In fact, the current to the anode is almost entirely composed of electrons – both the electrons from the electron source, and secondary electrons generated during ionization. The excess electron generation from the cathode is usually sufficient to current-neutralize the ion beam with electron emission from the anode when the cathode current is set to the anode current [66]. However, the cathode current is usually set in excess of this current.

3.1.1.3. Electric Discharge and Voltage-Current Characteristics

Since, typical thin film processing/modification pressure ranges from 10^{-5} Torr and 5×10^{-3} Torr (Figure 3-5), ion sources must be operated in this region for ion assist modifications. Ion beam operation

in this pressure range exists in primarily two modes of operation, a) a self-sustained discharge and b) a non-self-sustained discharge.

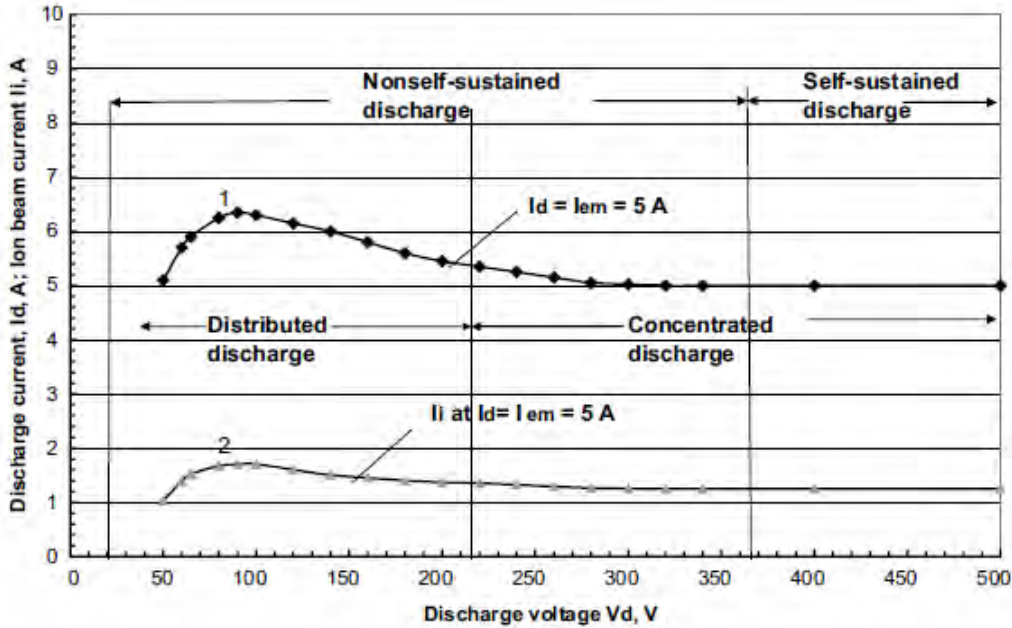


Figure 3-5. Voltage-current characteristics (between 5×10^{-5} Torr and 1×10^{-3} Torr) of an end-Hall ion source showing the various regimes of operation of its plasma discharge. The two curves show the voltage-current characteristics for a discharge current of $I_d = 5$ A and corresponding ion beam current of I_i [61].

In the self-sustained discharge region, the plasma is comprised of ions generated by the ion source and a number of electrons equaling the total positive charge in the plasma [61]. These electrons are generated when a plasma discharge voltage of $V_d \geq 300 - 350$ V is applied between the anode (ion source) and any surface that can act as a conductor in the vacuum chamber (chamber walls, flanges, bellows, etc.). These surfaces can potentially serve as the cathode materials from which a sufficient number of electrons can be generated from the ion bombardment. Because no external source of electrons is needed, this discharge is known as a self-sustained discharge [61].

However, at discharge voltages between 50 V and 300 V, the discharge voltage by itself does not produce enough secondary electrons to sustain the discharge [61] [64]. This region of operation is called a non-self-sustained discharge. In this type of discharge, an external source of electrons is needed to

generate and maintain stable plasma. The source of electrons is either a hot filament (HF) or a hollow cathode (HC), and will be discussed in the next section.

The voltage-current characteristics of a Hall current ion source depend on several factors such as [61]:

1. Pressure at the discharge channel. Higher the pressure, the lower the discharge voltage.
2. Magnetic field value atop the gas reflector at the anode. In general, the lower the magnetic field, the lower the ignition voltage (However, this leads to a lower ion beam current)
3. System geometry, anode dimensions and the relative placement of the electron source.

3.1.1.4. The Ion Source for the LANS BTB System

For this thesis, an ion source is required which produces ions with energy less than the sputter threshold of all material in the deposition chamber. In addition, the ion source required must be rugged for operation in a reactive environment. The EH-1000 compares well to the required specifications (Figure 3-6). Some key features are as follows [63] [67]:

1. A hollow cathode was used to as the source of electrons to prevent cathode oxidation during reactive sputtering.
2. The anode was grooved (Figure 3-7) to prevent the oxidation/deposition of dielectric materials that prevents operation at a low discharge voltage.
3. The discharge voltage was reduced to < 30 V by reducing the strength of the magnetic field in the discharge chamber. The ion source was custom designed for this sputter system by Kauffman and Robinson Inc. The magnetic field was established using an Alnico magnet whose field intensity was reduced to 400 G (versus the original 550 G) atop the gas reflector. This reduced magnetic field strength was measured using a F.W. Bell Gaussmeter, Model 410 and compared with quoted values from the product technical specifications.

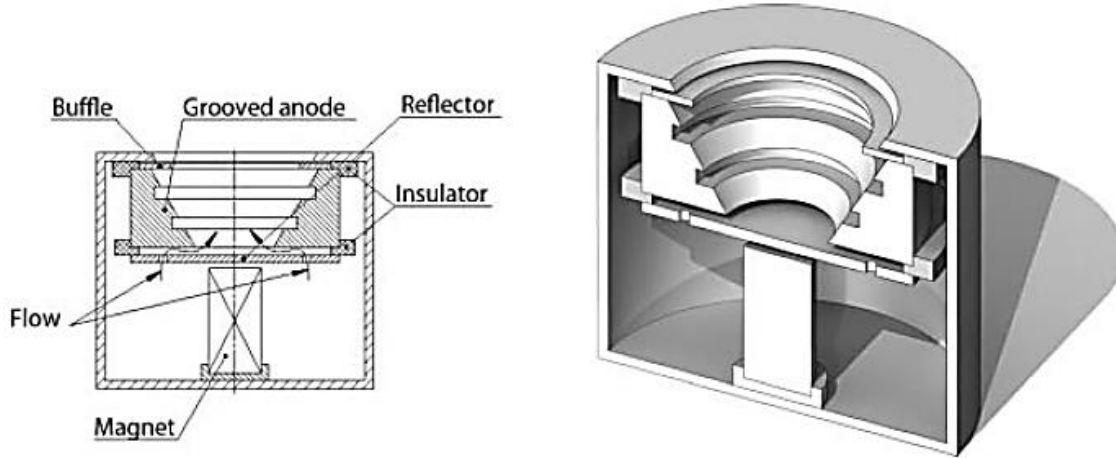


Figure 3-6. An End-Hall ion source with a grooved anode and baffle to reduce anode “poisoning”/oxidation [61].

A retarding potential analysis (Figure 3-7) at different angles at a distance of 30 cm from the center of the ion source shows that > 90% of the ions have energies < 30 eV, which is less than the sputter threshold of most materials in the deposition chamber [61] [68].

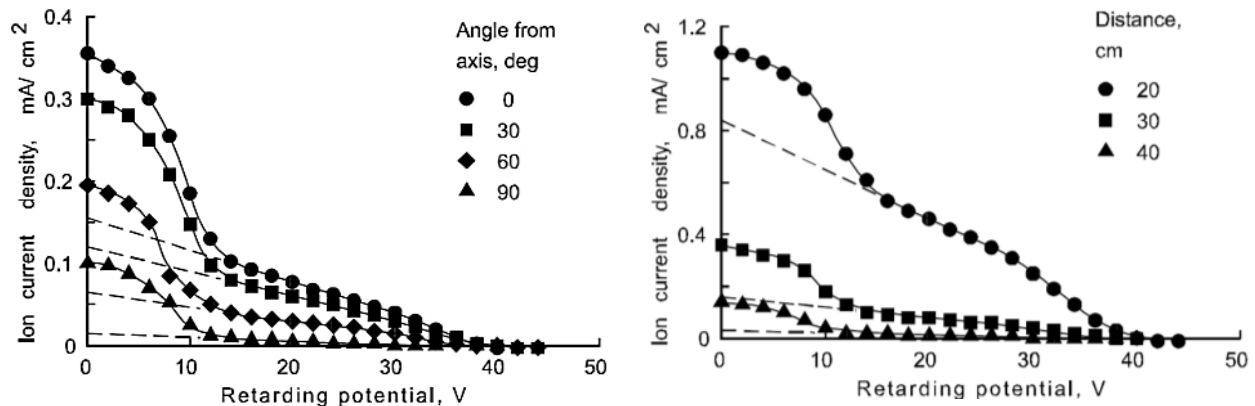


Figure 3-7. a) Angular retarding potential analysis of a modified KRI EH1000 ion source indicating most ions having energy < 30 eV. The measurements were made at a distance of 30 cm. b) Angular retarding potential analysis of a modified KRI End-Hall 1000 ion source as a function of distance from the ion source. The operating gas is Ar at a pressure of 1 mTorr. The discharge characteristics were 10 Amperes at 42 V with a gas flow of 70 sccm [68].

Because End-Hall ion sources are unfocussed ion generators, it is important to understand the angular distribution of ion current produced by the ion sources. Figure 3-8 shows the angular distribution of ion current density at a distance of 30 cm from the ion source, as is the case in the 4Wave’s LANS System [68].

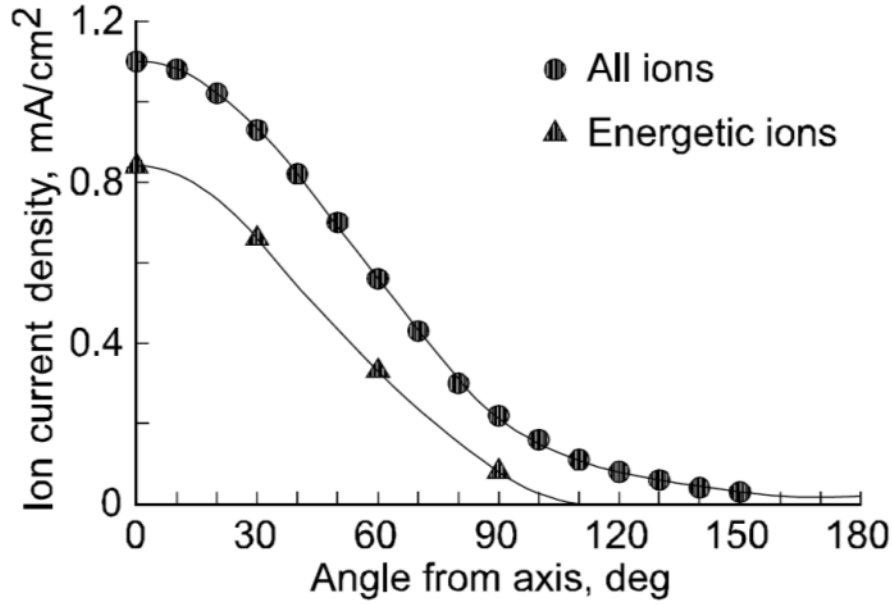


Figure 3-8. Spherical ion current density profiles for the KRI End-Hall 1000 ion source with the source at the center of the sphere. Source to target distance is 30 cm (12 in.). The working gas was 70 sccm of argon and the discharge characteristics were 10 A and 45 V [68].

3.1.2. Hollow Cathode Electron Source

As discussed in the previous sections, the ion source's mode of operation of interest lies in the non-self-sustained discharge region: an external source of electrons is required for ionization and neutralization of the space charge region of the ion beam. Without an external source of neutralization the plasma is under neutralized and extracts electrons from any object in the deposition chamber [61] [64]. This extraction manifests itself in the form of an undesirable arc that could last for a several microseconds and whose frequency of occurrence may depend on the degree of under neutralization of the ion beam.

In an ion source, the discharge current is given by the sum of the ion current and electron current produced by the discharge:

$$I_d = I_{i,d} + I_{e,d}$$

In the case of a non-self-sustained discharge $I_{i,d} > I_{e,d}$, the neutralizer should provide the difference between the ion and electron current such that the net neutralization electron current is equal to the ion current. This can be expressed as:

$$I_d = I_n = I_{e,n} + I_{e,d}$$

Therefore the ion source discharge current is the sum of ion current and the current from an electron neutralizer as:

$$I_d = I_{i,d} + I_{e,n}$$

Typically the electron current from the neutralizer is set to a value higher than the ion source discharge current. The effect of under neutralization can be seen in Figure 3-9. The additional electron current not only facilitates the ionization of the working gas in the ion source discharge chamber but also to produce an ion beam with low energy spread as shown in Figure 3-9.

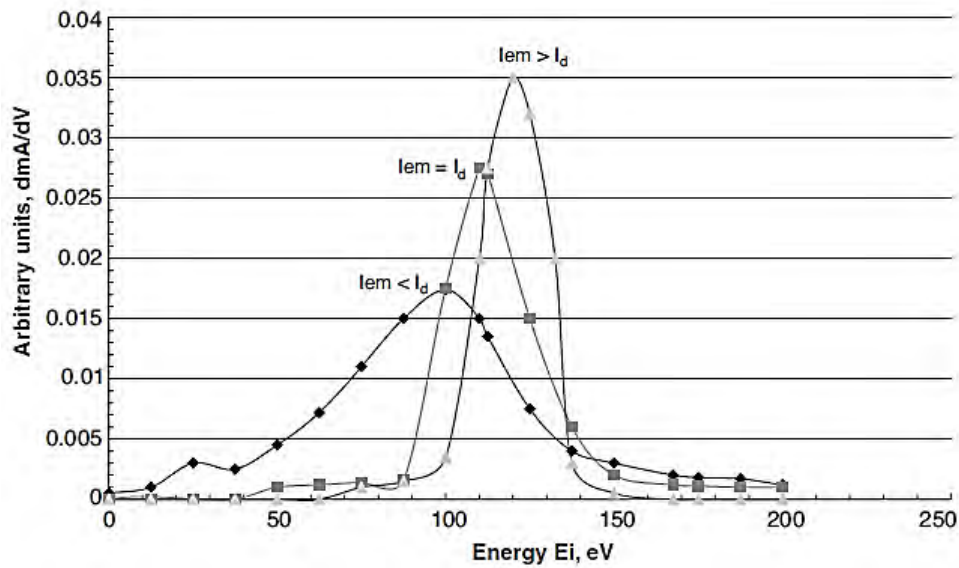


Figure 3-9. Typical ion beam energy distribution for different neutralization ratios: I_{em} (3.8 A) < I_d (4 A), $I_m = I_d = 4$ A and I_{em} (6 A) > I_d (4 A) [61].

There are two main types of electron sources: the Hot Filament type (HF) or the Hollow Cathode type (HC). Due to the limited lifetime of HF type source in thin film deposition, HC type electron sources are commonly used.

Hollow cathode electron sources are an alternative source of electrons that overcome the shortcomings of the hot filament type electron sources as described in the previous section. In these types

of sources, a refractory metal tube is negatively biased to create argon ion bombardment. This ion bombardment causes significant heating, leading to thermionic emission from the refractory metal (tungsten) [61] [66] [69]. Because of the low pressure regime of operation of these electron sources (< 0.01 Torr), these electron sources are operated by maintaining a constant flow of ionizable gas through them [61] [66] [69].

Thermoelectron emission current of a material with a square potential barrier is governed by the Richardson-Dushman equation [70]. For a conductor at temperature T and a work function ϕ , the emission current density is given by:

$$j = A_0 T^2 e^{-\phi/kT} \quad \text{Equation 18 [70]}$$

Where $A_0 = 4\pi mek^2/h^3 = 120.4 \text{ A/cm}^2\text{K}^2$ is the Richardson constant for a tungsten filament, T is the temperature of operation ($\approx 2500\text{K}$) for the tungsten filament and k is the Boltzmann's constant, $k = 1.38 \times 10^{-23} \text{ J/K}$. This gives a typical current density of $\approx 0.65 \text{ A/cm}^2$ [61].

One of the first hollow cathode assemblies was described by [69]. Since its invention, there have been numerous performance improvements. One such iteration of the hollow cathode is manufactured by the Kaufman & Robinson Inc. and is shown in Figure 3-10 [71].

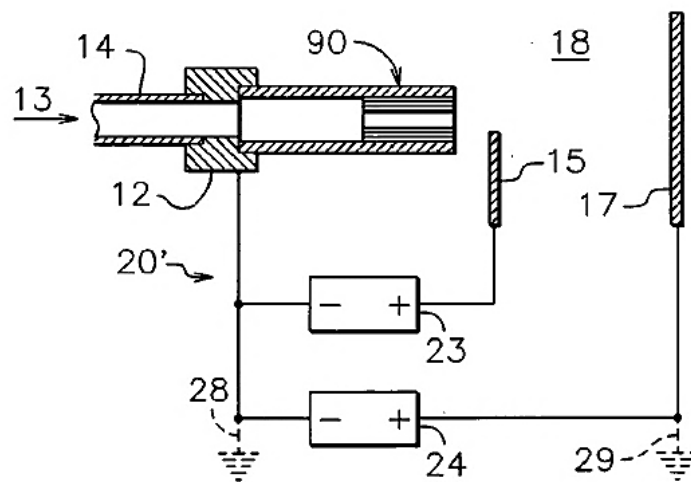


Figure 3-10. Schematic and electrical circuit diagram of a hollow cathode assembly [71].

The operation of this Hollow Cathode is described in reference [68] and is summarized here: Prior to operation of the hollow cathode, a flow > 75 sccm is maintained to purge contamination physisorbed in the hollow cathode assembly. This high flow rate also produces a large number of electrons which facilitates to strike the plasma. To start the hollow cathode electron source (HCES), a voltage of several hundred volts is applied between the keeper 17 and the cathode body 90. Once a plasma is established between the keeper and the cathode, the keeper current should rise to ≈ 1.5 A (for LHC-1000). At this point sufficient argon ions are generated in the gas 13, flowing out of the cathode tip to start thermionic emission of the cathode. A current controlled power supply can be used to supply a positive to the assembly body with respect to the tip 90, thereby causing ion bombardment of the tip.



Figure 3-11. An end-Hall ion source showing the typical placement of a filament [68].

The hollow cathode design adopted in the biased target deposition of this work is one of such iterations detailed in a 2010 patent filing (Figure 3-11) and realized as LHC-1000 electron source by Kaufman & Robinson Inc. [71]. Figure 3-11 shows the ion and electron source assembly. The electron source is physically mounted on the ion source in the direction of the ion beam propagation.

3.1.3. Summary of Operation of 4Wave LANS system

The key points that are to be kept in mind when setting parameters for deposition in this tool are:

1. The ultimate requirement for deposition with this technique is obtaining a large flux of ions in the deposition chamber
2. A large amount of electrons must be generated for igniting and sustaining ion generation of low energies
3. The gridless type ion source produces ions with different energies whose distribution is angular.

The ions along the axis carry the highest energy and can be used for secondary conditioning of the growing thin film with minimal contamination from the sputtering of the chamber walls.

Table 2 gives the parameters used for deposition in this work. The only variable in this work is the partial pressure of oxygen whose values will be given in subsequent chapters in which VO_x thin films were deposited.

Table 2. Parameters used for deposition of VO_x thin films in this work

Hollow cathode (HC) Ar flow rate: 10 sccm		Ion Source Ar flow rate: 60 sccm		O₂ flow: Varies based on oxygen partial pressure	
Keeper V/I: 20 V/1.5 A		Bias V/I: 23 V/8 A		Source V/I: 38 V/8 A	
Target Material(s)/Gun(s): 3 Vanadium Targets		Spin: 20 rpm Time: 30 min.	V/I (Gun 1): –800 V +5 V	V/I (Gun 3): –800 V +5 V	V/I (Gun 5): –800 V +5 V
Pulse Width #1: 1 μsec	Period #1: 100 μsec	Pulse Width # 3: 1 μsec	Pulse # 3: 100 μsec	Pulse Width # 5: 1 μsec	Pulse # 5: 100 μsec
P_{Total}: 5.8 × 10^{–4} Torr		P_{H2O}: < 2 × 10^{–7} Torr		P_{O2}: Varies	
				P_{H2}: < 1×10^{–7} Torr	

3.2. Deposition of Hydrogenated Ge:H Thin Films

Thin films of Hydrogenated Germanium (Ge:H) were deposited using a research scale Plasma Enhanced Chemical Vapor Deposition (PECVD) with 13.56 MHz RF power capacitively coupled to the two electrodes of the system as can be seen in Figure 3-12. The thin films of Ge:H were deposited using

the carrier gas germane (GeH_4) gas diluted with hydrogen before entering the deposition chamber by a variable dilution ratio. The dilution ratio $\{R = [\text{H}_2]/([\text{H}_2]+[\text{GeH}_4])\}$ is programmable by means of varying the gas flow using a mass flow controller. The dilution can be increased or decreased by increasing the amount of GeH_4 to H_2 .

The deposition of thin films of hydrogenated SiGe alloys using PECVD is well known with numerous reports detailing the process. In CVD, a source gas is used in the fluid-flow regime (High pressure). Briefly, during the PECVD deposition of Ge:H, the carrier gas for germanium (GeH_4) is mixed with hydrogen gas (H_2) and introduced into the chamber through a mass flow controller (MFC) which is programmable for a certain dilution ratio. Figure 3-12 shows a schematic of the chamber used in this work. A low power plasma is struck with a power density of 0.08 W/cm^2 , using an inductively coupled plasma at a radio frequency of $f=13.56 \text{ MHz}$. By electron impact ionization, the gas disassociates to produce a variety of ions, radical species and primary and secondary electrons. These species may adsorb onto the surface of the substrate to form a thin film.

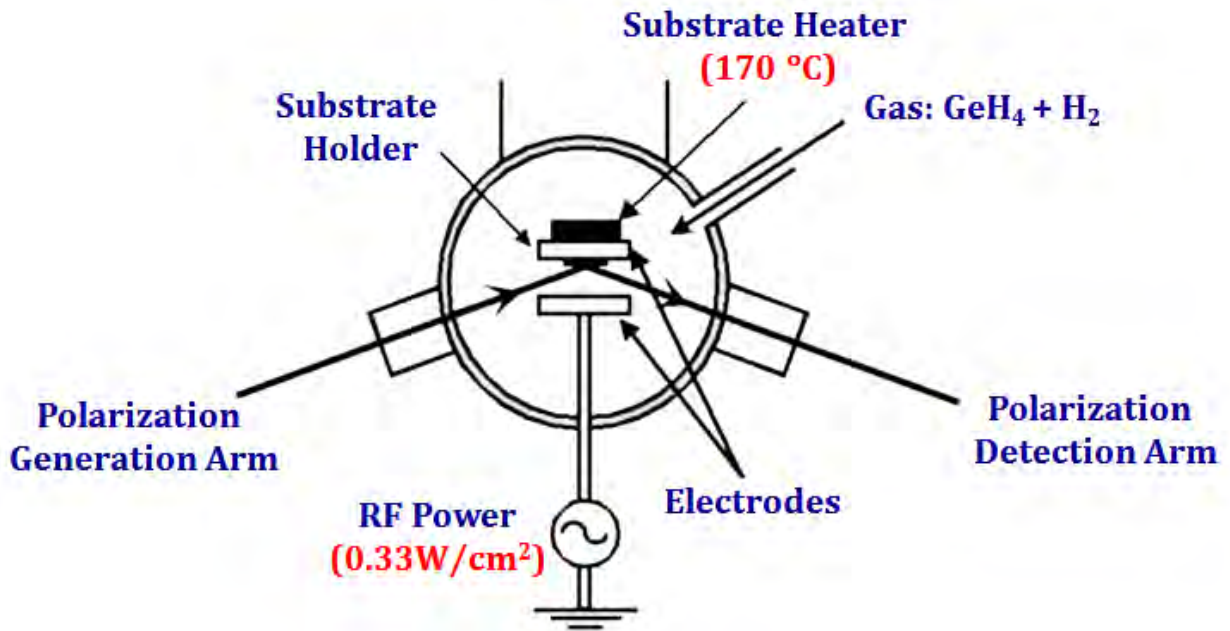


Figure 3-12. Schematic of the plasma enhanced CVD deposition chamber used to deposit the Ge:H of this work as it appears in ref. [72].

The spacing between the electrodes and the plasma power density are used to control the plasma kinetics and therefore the ion bombardment experienced by the growing thin film. The substrate temperature on the other hand influences the surface reactions on the substrate. Low substrate temperatures may lead to a low density, disordered thin film because the impinging species may not have enough adatom mobility. On the other hand a high substrate temperature may lead to reduced hydrogen incorporation, which may leave the growing thin film unpassivated.

The total flow rates and the pressure for deposition, as with any vapor deposition, decides the residence time of the disassociated species created during the RF plasma. Large deposition pressures may lead to significantly reduced mean free paths. This in turn leads to an increase in gas phase reactions and produces an undesirable number of particles.

In the case of Si:H deposition, the process parameters have been optimized for infrared imaging applications over many years of active investigation [53] [73]. The substrate temperature is usually kept at 200 °C, the total pressure is around 0.5 Torr and a low plasma is applied (plasma density $\sim 0.08 \text{ W/cm}^2$) [74]. These deposition conditions optimized for Si:H were found to be non-optimal for thin films of Ge:H [53].

3.3. Characterization Techniques

3.3.1. Grazing Incidence X-Ray Diffraction (GIXRD)

Grazing-incidence diffraction is a scattering geometry that combines the Bragg condition with the conditions for x-ray total external reflection from crystal planes to identify the crystalline phase of the sample under investigation. This configuration uses small angle of incidence and reduces the penetration depth of the x-ray by up to three orders of magnitude (typically from 1-10 μm to 10-100 $^\circ\text{\AA}$).

Grazing incidence x-ray diffraction was done using a PANAnalytical PRO X'Pert MPD with Cu K α 1 ($\lambda = 1.54 \text{ \AA}$) radiation, to analyze the structure of the deposited thin film. Diffraction patterns were

collected for 2θ values between 10° and 85° , and a scan rate of $1.2^\circ/\text{min}$. The crystalline phase and the lattice parameter were determined by comparing the peak positions and intensities and their corresponding 2θ values to that of standards using MDI Jade V9.0 software.

3.3.2. Atomic Force Microscopy (AFM)

Atomic force microscopy is a form of surface probe microscopy technique in which a sharp tip is scanned across the surface and the surface-tip interaction force is used to infer the surface morphology of the surface under investigation. For measurements in this work, measurements were made using the peak force tapping method using instrumentation developed by Bruker Icon.

3.3.3. Rutherford Backscattering Spectroscopy (RBS)

Rutherford Backscattering Spectroscopy (RBS) was used in this work to determine the stoichiometry of the VO_x thin films. RBS operates on a phenomenon that occurs when a high-energy primary ion (typically He^{++} ions with energies in the order of MeV) is elastically scattered. The energy and angle of the scattered ion yields information about the mass of the scattering atom in the sample. This information then can be used for composition analysis of thin films.

All RBS data described herein was collected at the Tandem Accelerator at the Department of Physics and Astronomy, Rutgers University. Figure 3-1 describes the schematic used for RBS experiments. All measurements were performed in a standard RBS chamber under a vacuum of 10^{-6} Torr using two Si surface barrier detectors: one at 155° and other at 100° scattering angle. A 2 MeV He^{++} ions from a 1.7MV tandem accelerator was used with an ion current of 2-3nA and a beam spot of 2mm.

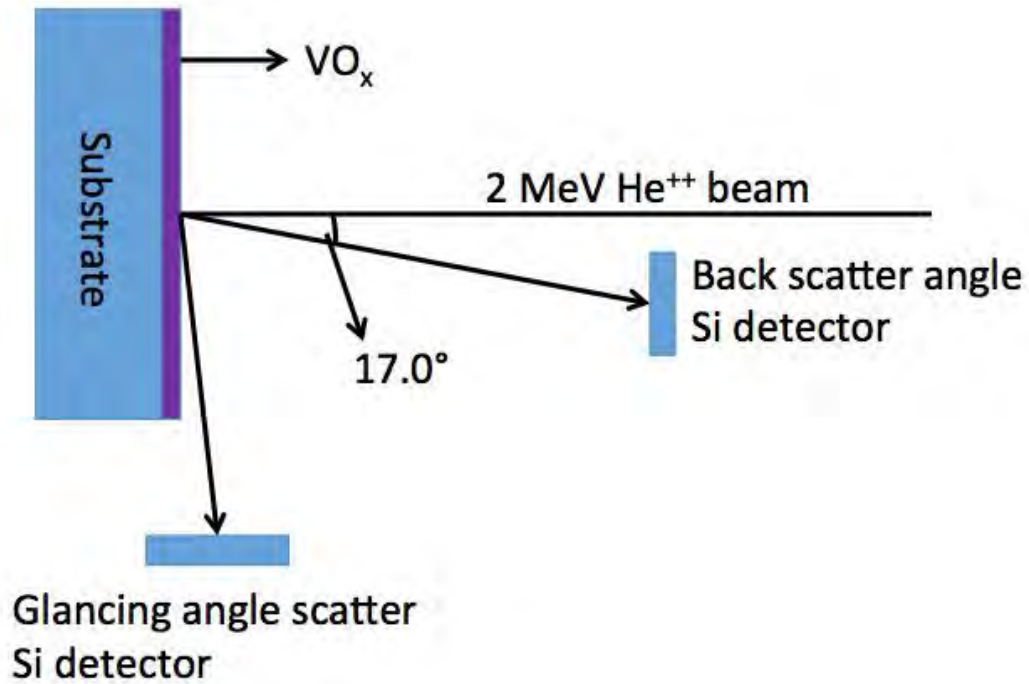


Figure 3-13. Schematic of a typical RBS experimental setup.

This ion beam is deflected into the RBS chamber, where it is incident on the sample under investigation. The He^{++} ions that are deflected are backscattered and their intensity is measured at a Si surface barrier detector which is placed at a 17° angle with respect to the incoming incident radiation. Data was collected till $10\mu\text{C}$ of charge was accumulated (typically 15 minutes).

3.3.4. Ellipsometry

Ellipsometry is a non-destructive technique which measures the change in polarization of a reflected beam of light from the sample's surface with a known polarization state. The change in the polarization of light depends on the structural and the optical properties of the sample under investigation. Unlike x-ray diffraction, ellipsometry is a portable and versatile tool that can be used to monitor in-situ the growth of thin films. Ellipsometric measurements in this work were conducted by using a J.A. Woollam Co. M2000-DUV variable angle rotating-compensator multichannel spectroscopic ellipsometer. This instrument uses two light sources, a Xe lamp and a Quartz Tungsten Halogen (QTH) lamp. By combining both light sources, the attainable ellipsometric spectra from the RC2 instrument spans over the

0.73 – 5.15 eV (1700 – 240 nm) spectral range. Figure 3-14 shows the schematic of an ellipsometry configuration. The measured response is a function of optical properties and the thickness of the thin film.

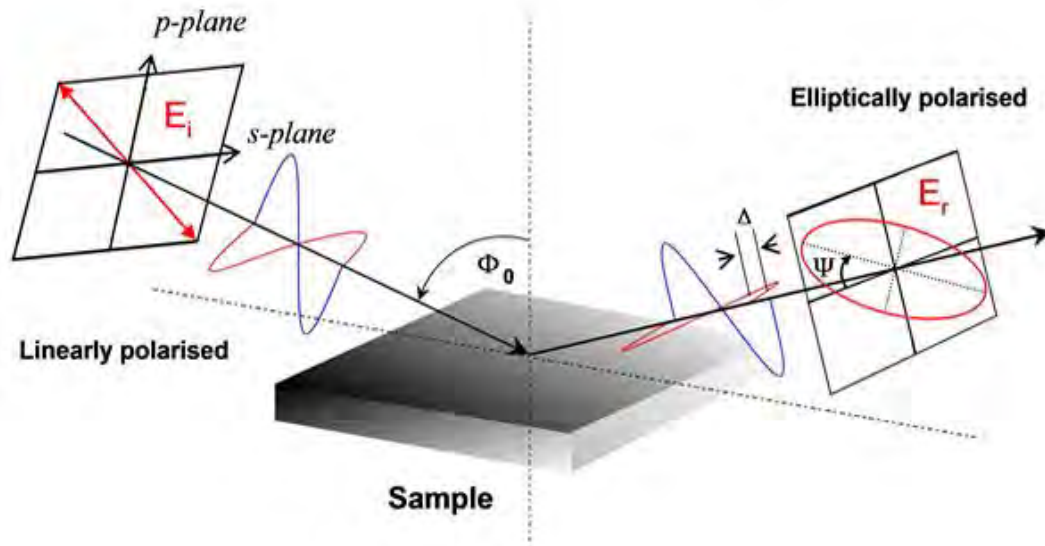


Figure 3-14. Typical configuration for ellipsometry measurement [75].

3.3.5. Resistivity Measurements

The resistivity of the thin film deposited was measured by using the Transmission Line Method (TLM). The TLM method gives a complete characterization of the contact by providing the sheet resistance, the contact resistance, and the specific contact resistivity. For top contacts to VO_x thin films, 100 nm of titanium was deposited using the Perkin Elmer sputtering system. Bottom contacts to VO_x thin films were obtained using only Vanadium as the bottom metal. The mask set used to extract resistivity values is shown in Figure 3-15. It consists of two layers, the first of which is used to isolated the TCR material so as obtain an accurate value of resistivity; the second layer consists of a series of five electrodes for metal contacts with spacings of 10 μm , 30 μm , 70 μm , 150 μm and 310 μm respectively.

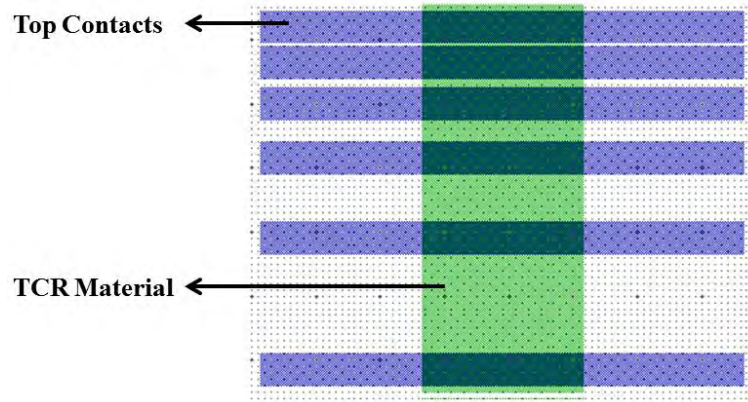


Figure 3-15. Transmission Line Method test structures showing features used in isolation of the TCR material and to deposit the metal contacts.

Current–Voltage (I–V) characteristics were measured by sweeping voltage using a Hewlett Packard 4140B pA meter/ DC Voltage source and the resistance was recorded. A LabVIEW program was used to collect the data. The I–V curves were examined to ensure ohmic behavior of the resistance structures. The resistance of each resistor with different spacing is plotted as in Figure 3-16. The Y–intercept gives the contact resistance. Apart from ensuring ohmic contacts, another important parameter used to assess the quality of the contacts is the transfer length [76]. Half the value of the x–intercept gives a value known as the transfer length. Transfer length is defined as the distance at which ‘1/e’ of the current is transferred from the semiconductor to the electrode or vice-versa. Thus an accurate measurement of the transfer length helps to determine the minimum spacing of electrodes (therefore the size of the active region) that can be used to extract electrical properties from the sample with minimal contribution from the contact resistance itself.

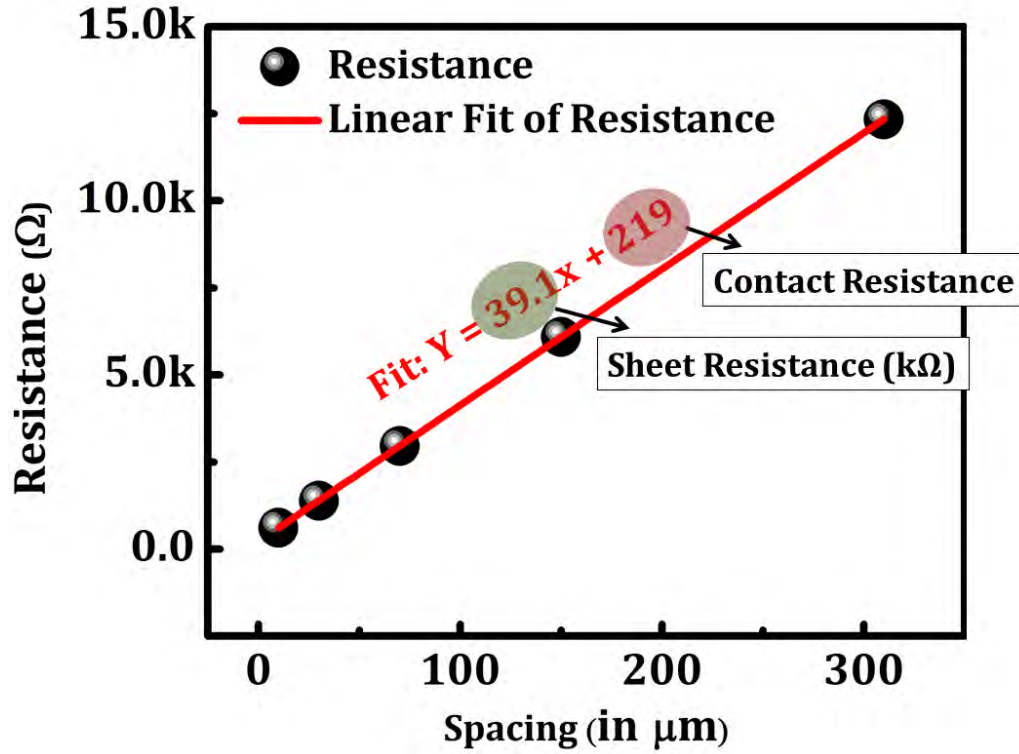


Figure 3-16. Plot of total resistance as a function of electrode spacing.

3.3.6. Temperature Coefficient of Resistance Measurements

As a prerequisite to measurements, electrical contacts must be made to the thin films. Metal contacts were deposited onto the thin film whose electrical properties need to be measured. Prior to the measurement, the contact quality is evaluated to ensure that Ohmic contacts were obtained. An HP4141B picoammeter was set up to source voltage and bias the thin film resistors, the resultant current was recorded. These I-V measurements were performed as a function of temperature from 30°C to 65°C at 5 °C increments. The data was exported into excel and the resistance was calculated at each temperature step. The resistivity is a function of temperature and can be described by:

$$\rho = \rho_0 e^{\frac{-E_a}{k_B T^2}} \quad \text{Equation 19}$$

$$\text{Or,} \quad \ln(\rho) = \frac{-E_a}{k_B T^2} + \ln(\rho_0) \quad \text{Equation 20}$$

A \ln resistance versus ' $1/k_B T^2$ ' plot was used to extract the activation energy of the thin film. The TCR can be calculated using the formula:

$$TCR = \frac{-E_a}{k_B T^2} \quad \text{Equation 21}$$

3.3.7. Measurement of Electrical Noise in Thin Films

As discussed in the previous chapter, the electrical noise in a thin film is comprised of two components, the Johnson noise and the 1/f noise. While the Johnson noise is a function of device resistance and the bandwidth of the measurement, the origin of 1/f noise, on the other hand, depends on the value of Hooge's parameter and the carrier concentration. Therefore in order to compare the inherent noise of a thin film the parameter ' α_H/n ' or the normalized Hooge's parameter must be extracted.

If the parameters V , f , I_{bias} and the measured I_{noise} are known, ' α_H/n ' (units: cm^3) can be extracted from Equation 14 such that:

$$\frac{\alpha_H}{n} = \frac{I_{N,1/f}^2}{I_{bias}^2} V f \quad \text{Equation 22}$$

Thin film samples were patterned using lithographic processing to define a known volume of the sample area. Figure 3-17 shows the patterns used to extract the normalized Hooge's parameter.

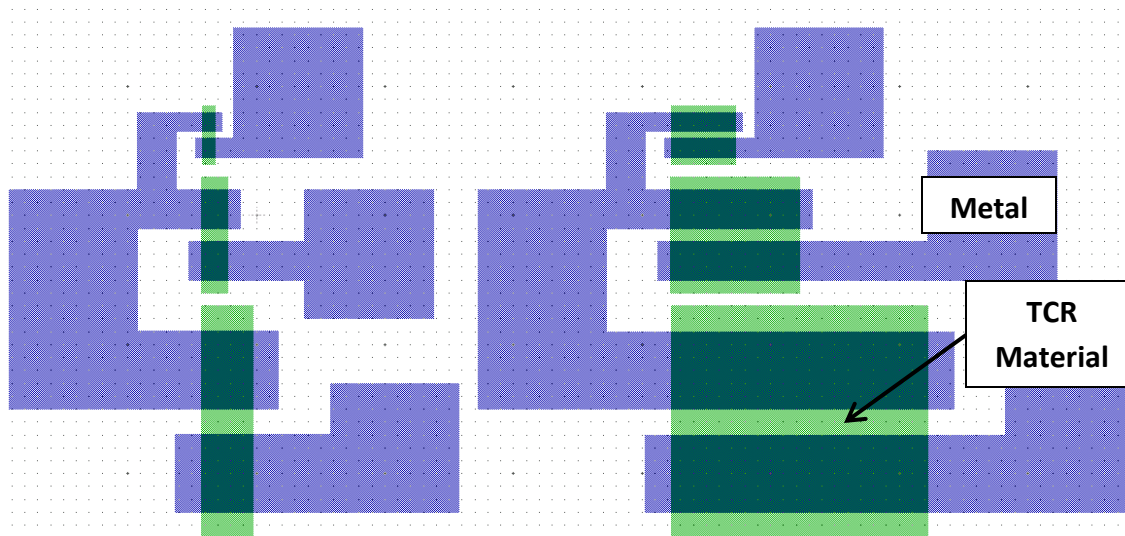


Figure 3-17. Schematic images from the mask set used to extract the normalized Hooge's parameter. Each pattern has a different volume but the same resistor width to length ratio.

Each pattern in Figure 3-17 contains three distinct volumes; however for each volume the aspect ratio (width to length ratio) is maintained the same. The similar aspect ratios allows for interrogation of different volumes while the thin film resistance remains the same. The lithographic patterning was done as shown in Figure 3-18 using Shipley Microposit 1800 series photoresist and Poly(methyl methacrylate) or PMMA C4. The active material was patterned using either dry or wet etching techniques. Thin films of Ge:H were etched in 30% hydrogen peroxide (H_2O_2). Since VO_x thin films are etched in the developer we used (Microposit 351), a double layer lithography technique was used with PMMA C4, as the underlying layer since PMMA can be developed in toluene (non-aqueous) post-exposure. A dry etch recipe was developed which utilized CF_4/O_2 plasma (100 mTorr, 25 sccm CF_4 : 100 sccm O_2 , -100V self-bias at a power of 100W). For high resistivity VO_x the etch rate was found to be ≈ 40 nm/min.

It was observed that for vertically integrated (through film) devices of VO_x , dry etching caused the thin film of VO_x to break down, and so, a wet etch recipe was also developed. High resistivity thin films of VO_x were found to be etched in dilute solutions of H_2O_2 (1:2,000) at an etch rate of 200 nm/min.

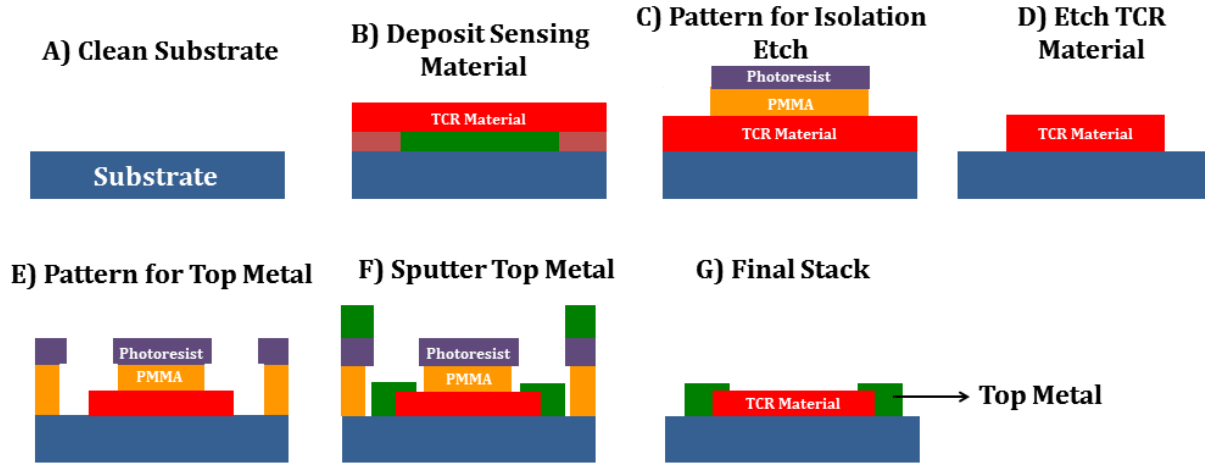


Figure 3-18. Schematic of lithographic processing of TCR material to extract resistivity, TCR and the normalized Hooge's parameter.

Once the sensing material was patterned, top electrodes were deposited using double layer lithography using PMMA as the liftoff resist. 100 nm of chromium was sputtered for making ohmic contacts to Ge:H, while 100 nm of sputtered titanium was used for thin films of VO_x .

Since the $1/f$ noise of a device also depends on the electrical contacts to the semiconductor [77], it is necessary to evaluate the contact quality and choose a device geometry from which the contribution from the contact resistance is minimized. Transmission line measurements were made and the contact resistance was evaluated. Electrical noise measurements were made on patterns such that the total contact resistance was significantly less than the total device resistance under consideration.

Previous attempts to measure $1/f$ noise of thin films have been through the measurement of a current power spectral density (PSD) at a specific volume and a reference frequency using a known electrical bias. Such spot measurements are performed using a dynamic signal analyzer (DSA) and are limited to one data point per measurement and could include unwanted contributions from the system noise, Joule heating, temperature fluctuation of ambient air, etc.

In this work, a custom-built $1/f$ noise measurement system and the technique to extract the $1/f$ noise of thin films is described which isolates the material $1/f$ noise from other noise sources. Some advantages to this noise measurement system over previous methods include: a large frequency range of

data acquisition obtained in a single measurement, a user controlled bandwidth of measurement, digitization of the output signal for post-measurement processing of the data, and low frequency drift correction for accurate measurement of the thin film's $1/f$ noise. The construction of the automated $1/f$ noise measurement system was mostly developed by Myung-Yoon Lee from the department of Electrical Engineering at the Penn State University.

3.3.7.1. Effect of Low Frequency Drift for the Measurement of Noise in Thin Film Resistors

Some devices consist of materials sensitive to temperature fluctuations while others may contain materials whose electrical property drifts due to physical changes associated with aging of the thin film in ambient. In such devices, the electrical output of the film drifts over time [77]. During their regular operation, these thin films are isolated from the ambient by vacuum packaging and temperature stabilization. However, these provisions are not feasible in laboratory desktop style measurement system in which numerous samples deposited using various deposition conditions need to be analyzed. Figure 3-19 shows the drift in resistance of a thin film of vanadium oxide measured over more than 45 hours. The resistance change manifests itself in the measured current as a sinusoidal variation with a long, non-constant time period (low frequency) which we refer to herein as 'drift'.

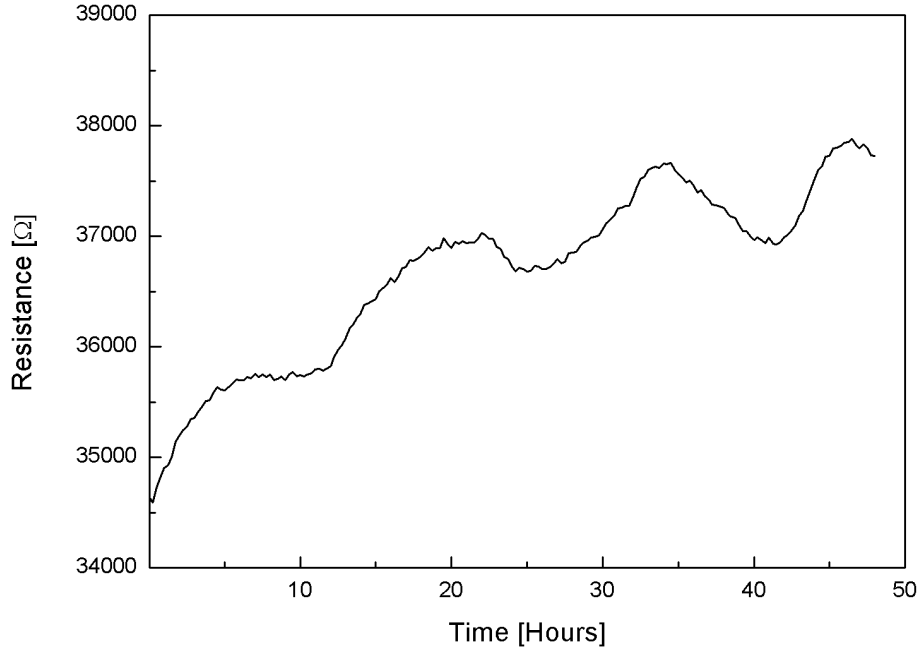


Figure 3-19. Resistance fluctuation (drift) of a thin film resistor of vanadium oxide capped with SiO₂

This drift causes variations in the measurement which makes both data acquisition and data analysis difficult. When the acquired time–signal data is converted into the frequency domain, this low frequency drift causes a shift in the acquired spectra and makes the $1/f$ noise of the thin film appear larger than its true intrinsic value.

In the measurement system developed for this work; the low frequency drift has been subtracted using post-measurement data processing. A voltage offset correction has been applied whose value as calculated as follows. Let us assume that the measured voltage output can be modeled by a sinusoidal signal using the following equation:

$$V = X \sin(2\pi ft) + Y + Zt \quad \text{Equation 23}$$

Where V is the voltage noise modeled, X is the amplitude of $1/f$ noise, Y is a constant voltage offset required to subtract the bias voltage, Z is the magnitude of the drift effect, f is the frequency and t is the discrete time which has a range of 0 sec to 10 sec for our measurement, so that the lower limit of frequency is 0.1Hz. When the acquired time domain signal is converted into frequency domain, the

obtained result is shown in Figure 3-20. The noise PSD displays a sharp peak given by the $1/f$ noise at a frequency f of 10Hz.

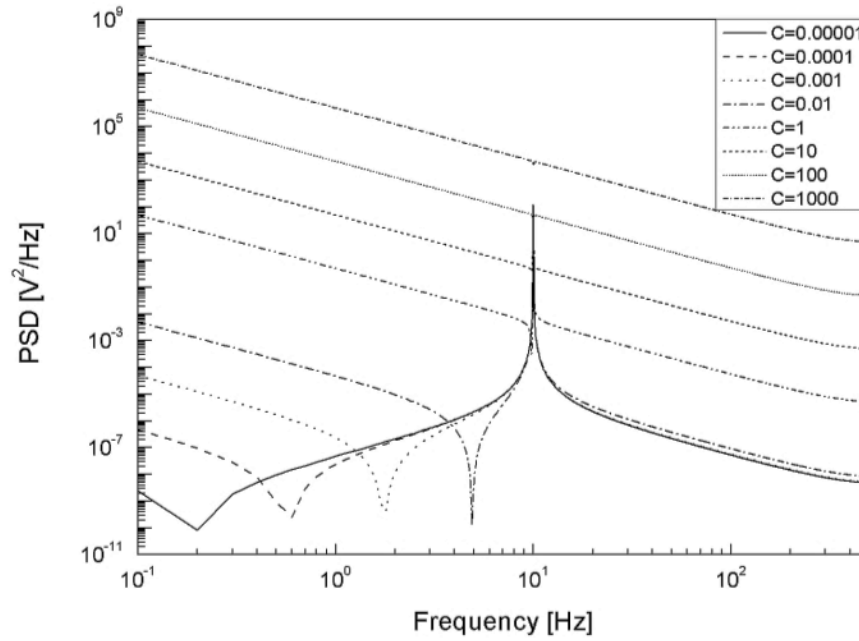


Figure 3-20. The recorded PSD for varying magnitudes of drift, C . The peak represents the $1/f$ noise (in this case at 10 Hz).

We observed no change in the spectra with the magnitude of the offset value used; which implies that the $1/f$ noise is not affected by the offset of the amplifier at least when offset value is within the input range of filter or the measurement instrument. On the other hand, the plotted $1/f$ noise spectrum of Figure 3-20 is strongly affected by the drift of resistance of the thin film which appears as a linear function of f^{-2} . As the drift effect gets larger, the Z value increases and can even surpasses the $1/f$ noise of the material seen here for large values of C and for smaller frequencies. However, due to the difference in their frequency dependence, (Drift has a $1/f^2$ dependence, while flicker noise has a $1/f$ dependence), they can be separated from each other. The noise measurement system developed in this work consists of drift filtering to obtain a noise spectral density that follows Hooge's empirical relationship and has a slope of negative unity. It must be noted that since we attribute this drift to self-heating of the resistor, we find this drift particularly large when a large power is dissipated across the resistor.

A schematic flow chart of the noise measurement setup is shown in **Error! Not a valid bookmark self-reference.** The setup consists of three instruments: A low noise current amplifier (A Stanford Research SR-570), a dual channel filter and a data acquisition hardware (DAQ) card which is controlled by a personal computer. The SR570 contains an RS-232 interface which allows for remote control of each operation eliminating the need for a manual operation. The SR570 has internal batteries capable of providing up to 5V. To avoid the need for microscope and a probe station, and hence make the setup simpler, a 16 pin ceramic dip package is used along with Al or Au wires. The dip package is placed in a faraday's cage (a small Al box) to isolate the sample from the environment. A second shielding box is used to isolate the entire shielding assembly and the measurement setup from the environment. In addition, all assemblies and instruments are grounded using a heavy copper wire. A floating table is used to isolate the measurement assembly from all sources of vibration.

Using a LabVIEW program, the wire bonded samples were biased using the internal battery of the SR-570. Prior to data acquisition at the DAQ, proper filtering of the acquired data is necessary. A low pass filter of 1 KHz is used as an anti-aliasing filter to remove the high frequency signal, which may affect the lower frequency noise. In addition a high pass filter of frequency 0.1 Hz is necessary to remove any low frequency drift which leads to erroneous values of the thin film's inherent $1/f$ noise. To avoid aliasing, sampling rate of DAQ should exceed Nyquist rate. We have used a sampling rate of 20 KHz, much higher than the Nyquist rate which is set to be ≈ 2 KHz ($2 \times (1 \text{ KHz} - 0.1 \text{ Hz})$). The acquisition time is set to 20 seconds, and the data collected is averaged over 20 samples. At the end of the measurement, the sample is connected to a pico ammeter (HP 4140B DC SMU) and the current bias is recorded.

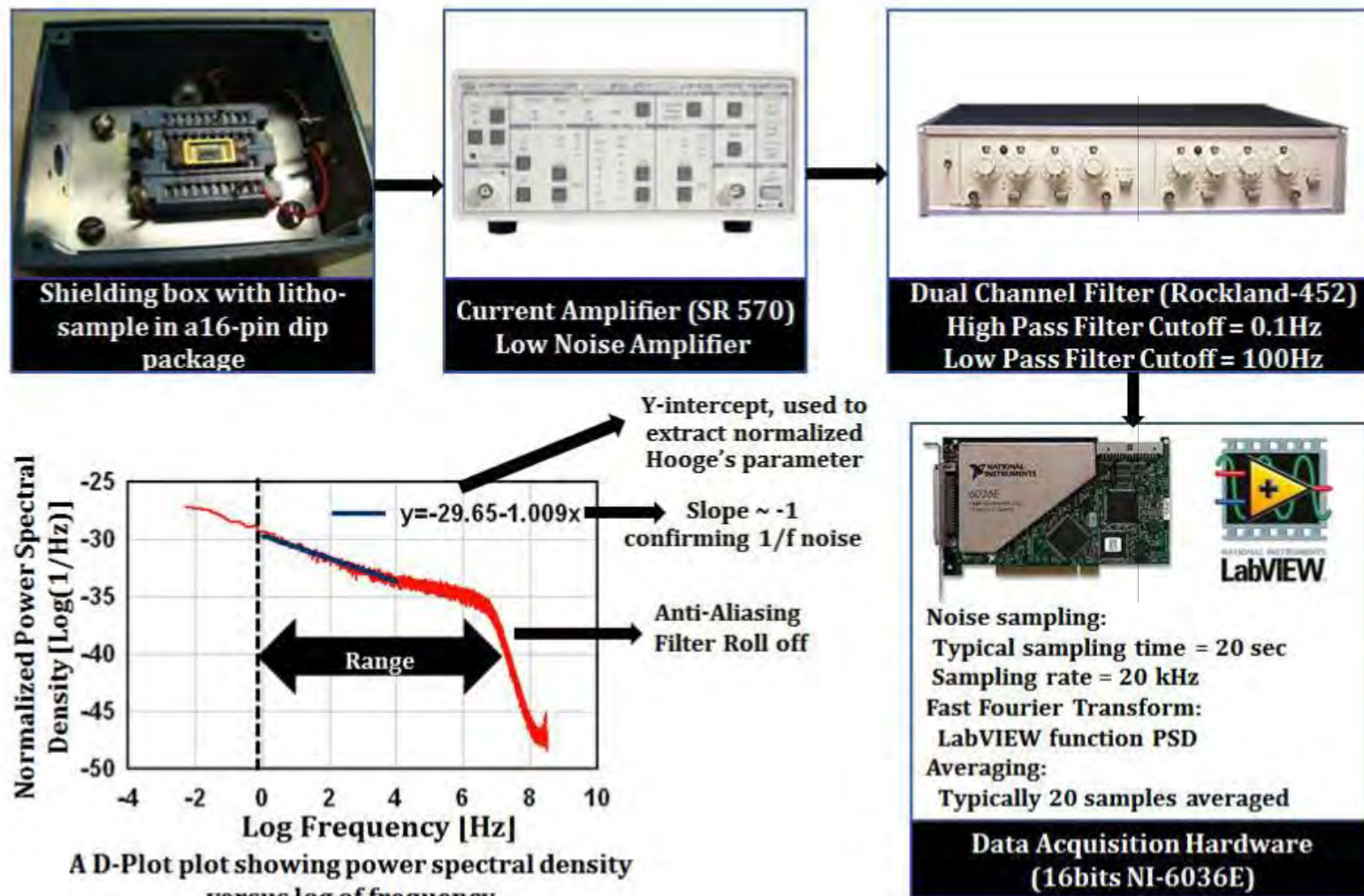


Figure 3-21. A schematic showing the process flow used in this work for the measurement of 1/f noise in thin films.

The averaged time varying signal is converted into the frequency domain using the LabVIEW's Fast Fourier transform function. This power spectral density (PSD) is plotted as a function of frequency such that the resultant graph resembles the schematic representation of Figure 3-22.

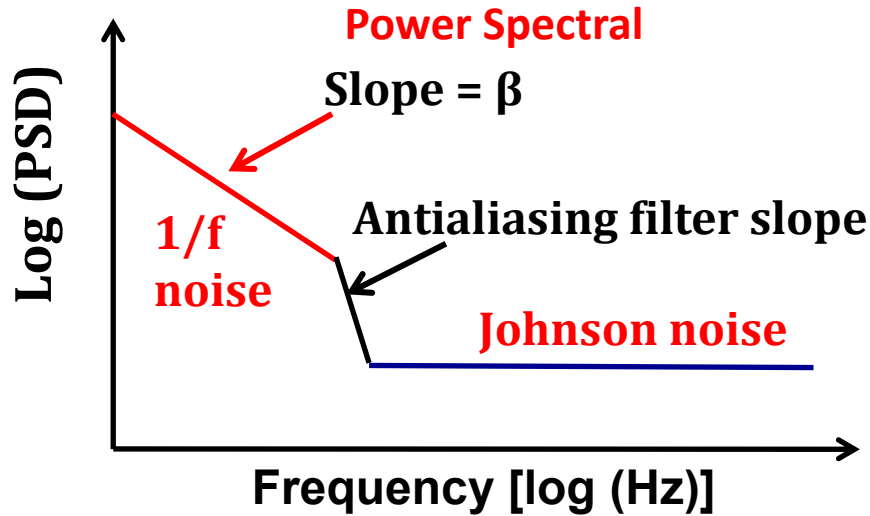


Figure 3-22. Frequency spectra representation of collected spectra showing two distinct regions: a) Region with 1/f noise and, b) Region with Johnson noise

If the magnitude of the 1/f noise is higher than the Johnson noise, the lower frequency of the spectra is a line with a slope of ‘-1’ in a log-log scale. An anti-aliasing filter roll off appears at 1 KHz which is associated with the low pass filter; whereas the Johnson noise appears as ‘white’ because it is independent of the frequency. Depending on which noise contributor is larger the recorded power spectral density (PSD) may differ from Figure 3-22. If the device resistance is high, the total noise may be dominated by Johnson noise and the 1/f noise may be suppressed in the spectra. In such a case, an alternate aspect ratio of the same thin film must be measured such that the device resistance and therefore the Johnson noise is lower than the thin film’s 1/f noise.

In summary, In order to successfully extract the normalized Hooge's parameter it is necessary to ensure that the Hooge–Vandamme relationship is satisfied. As Equation 22 suggests, the intensity of the recorded PSD depends on:

1. f^{-1} (1/frequency) of measurement,
2. The volume of the device interrogated,
3. The bias applied to the device and
4. The normalized Hooge's parameter or ' α_H/n '.

Thus if everything but normalized Hooge's parameter is known, it can be estimated by using Equation 22. Figure 3-23 shows the acquired PSD of the data with decreasing volume of the sample and with increasing bias applied to the sample. If the sample bias is kept constant and the volume is halved, the magnitude of PSD is doubled. Similarly if the volume is kept constant and the applied bias is doubled, the magnitude of PSD is also doubled.

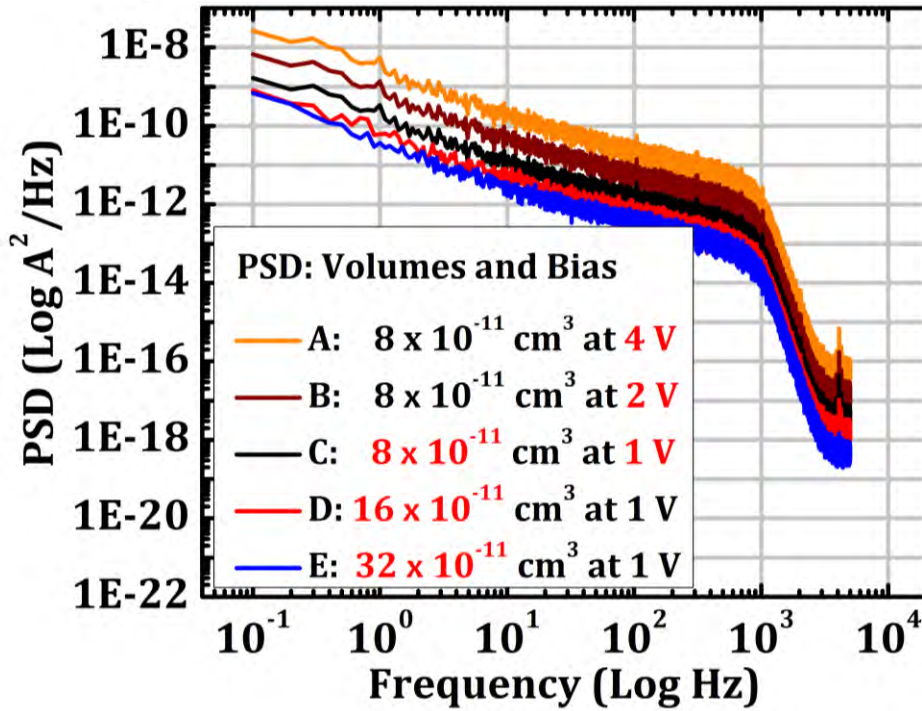


Figure 3-23. Acquired Power Spectral Densities of a thin film for different volumes and different biases to confirm the Hooge–Vandamme relation and extract the materials normalized Hooge's parameter.

Chapter 3 has provided an overview of the experimental methods used in this work. Detailed specifics are added in the following chapters as necessary. Having discussed all the tools required for characterization of thin films, the next chapter looks at high TCR thin films of VO_x and Ge:H for use as infrared imaging materials.

Chapter 4. High TCR Thin Films of Vanadium Oxide (VO_x) and Hydrogenated Germanium (Ge:H)

4.1. Introduction

Thin films of vanadium oxide (VO_x) and hydrogenated amorphous silicon (a-Si:H) are the two dominant material systems used in resistive infrared radiation detectors for sensing wavelengths in the 8–14 μm range. While thin films of VO_x ($x < 2$) currently used in the bolometer industry have a magnitude of temperature coefficient of resistance (TCR) between 2%/K – 3%/K, the magnitude of TCR of a-Si:H thin films lies between 3%/K to 4%/K [8] [30] [78] [18]. Although high TCR materials are desired, increasing the activation energy (and therefore the effective band gap) results in a decrease in the mobile carrier concentration and therefore resistivity [30]. This is evident from the fact that while VO_x thin films have a resistivity between 0.1 – 1 $\Omega\text{-cm}$, a-Si:H used in microbolometers have a resistivity between 200 and 2,500 $\Omega\text{-cm}$ [8] [30] [78] [18].

Unfortunately high resistivity materials are also associated with high Johnson and 1/f noise. The fundamental differences in resistivity and electrical noise of VO_x and a-Si:H thin films used in the microbolometer industry requires two distinctly different read out circuits [18] [60] [59]. To overcome the higher noise in a-Si:H thin films, the devices are constantly biased and averaged numerous times at the pixel level so that the noise contribution can be reduced dramatically [18] [60]. Such a constant bias readout circuit cannot be used for thin films of VO_x due to the self-heating associated with their lower resistivity [30] [59]. In 2013, Jin et al. demonstrated thin films of VO_x having the lowest resistivity of all previously deposited VO_x thin films with $|\text{TCR}| > 5 \text{ \%}/\text{K}$ (Figure 4-1) [79]. In this work, thin films with $|\text{TCR}|$ as high as $-5\%/K$ were deposited having resistivity as low as 10,000 $\Omega\text{-cm}$ [79]. The obtained TCR and resistivity values made these films potential candidates for use in constant bias bolometer systems. However, this work did not contain any information on the inherent 1/f noise properties of these thin films.

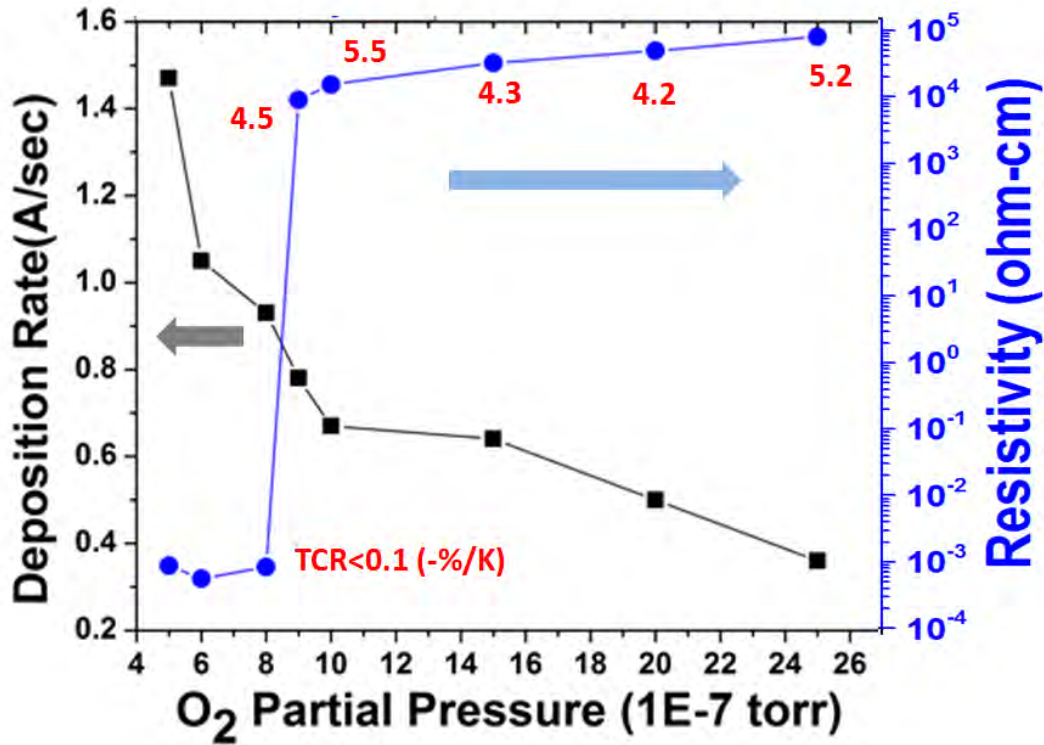


Figure 4-1. Deposition rate, resistivity and TCR of thin films of VO_x deposited by Biased Target Ion Beam Deposition as a function of partial pressure of O₂ as it appears in ref. [79].

Another material system, consisting of amorphous silicon germanium alloys (Si_{1-x}Ge_x:H) has also been investigated for use in constant bias bolometer systems. The motivation for its use stems from a considerable research effort in the development of thin films of amorphous hydrogenated silicon (a-Si:H) for use in large area devices such as solar cells and as transistors in liquid crystal displays and for use as sensing material for infrared detection [73] [80] [50]. An analogous material system consisting of amorphous hydrogenated germanium (a-Ge:H) was also investigated for use in those applications [51] [52] [53] [54] [55], however, these thin films could not compete with the performance of Si:H/SiGe:H systems for the stated applications. While Si:H and SiGe:H have a dark resistivity between 10¹¹ – 10¹³ Ω-cm with light resistivities as low as 10⁴ Ω-cm, Ge:H thin films show smaller dark resistivity of 10⁷ Ω-cm with smaller thermal activation [80] [52] [53] [54] [55]. However, the lower resistivity of Ge:H thin films make them good candidates for further investigation as infrared imaging materials.

Further improvement in the resistivity – TCR tradeoff was necessary, even at these levels. In addition to the high Johnson noise imposed by high resistivity, these films have fairly high 1/f noise with the ‘ α/n ’ values around 10^{-18} cm^3 [51].

It was hypothesized that in the case of Ge:H thin films a reduction in the resistivity was possible by incorporation of nanocrystallites. Saint-John found that for PECVD deposited Ge:H, nanocrystallites can nucleate as early as 10–15 nm for a dilution ration ($[\text{H}_2]/\text{GeH}_4$) of 400 [74]. Furthermore, it was suggested that the nucleation density of germanium crystallites can be increased by lowering the substrate temperature from the previously investigated value of 200 °C to 170 °C [74]. Indeed it was seen that by incorporating a small fraction of nanocrystallites, thin films with resistivity of around 1,500 $\Omega\text{-cm}$ were deposited having a $|\text{TCR}|$ value of 3.7 %/K [57].

To further the development of high TCR materials, this work investigates high TCR VO_x and Ge:H thin films for use in constant bias systems. For thin films of VO_x , normalized Hooge’s parameter values are measured. To improve the electrical properties of Ge:H, in this work thin films of Ge:H have been deposited at a very high dilution ratio of GeH_4 in H_2 to incorporate germanium nanocrystallites. Electrical properties of mixed phase amorphous + nanocrystalline thin films are investigated by varying the crystal fraction of germanium; this was achieved by changing the total thicknesses of the deposited thin films.

4.2. High TCR VO_x Thin Films

4.2.1. Experimental Details

High resistivity VO_x thin films were deposited using a Biased Target Ion Beam Deposition System (BTIBD), the details of which were described in the previous chapter. Thin films ~ 85 nm thick were deposited having a thickness uniformity $\geq \pm 3\%$ for a 4” wafer. A three-target configuration was used to deposit the thin films. A series of films was deposited as a function of oxygen partial pressure, $p\text{O}_2$, ranging from 1×10^{-6} Torr to 2.1×10^{-6} Torr, corresponding to oxygen flow 5 % – 8.5% of argon. Detailed

values for the parameters used can be found in Table 2. The total flow was kept at 70 sccm, corresponding to a deposition pressure of $\approx 5.8 \times 10^{-4}$ Torr. A pulsed waveform was used to increase the sputter yield and prevent arcing of the target. The sputtering voltage was kept at -800 V while the duty cycle was set to 99%, for all three targets yielding a film growth rate of ≈ 0.5 Å/second.

Thin films were patterned using lithographic processing steps described in Section 3.3.7. The thickness of the deposited VO_x and Ge:H thin films was measured using an AFM, Dimension Icon made by (Bruker Corporation) on a lithographically patterned step in the thin films. The roughness of the thin films was evaluated using the same AFM. The crystal structure of the thin films was evaluated by grazing incidence XRD using a PANalytical's X'Pert Pro MPD. The composition of the VO_x films was evaluated by Rutherford back scattering (RBS) using a 2.275 MeV He^{2+} ion beam with the detector set at a backscattering angle of 160° [81].

4.2.2. Results and Discussion

Thin films of VO_x were deposited by BTIBD as a function of $p\text{O}_2$, from 1×10^{-6} Torr to 2.1×10^{-6} Torr. The films were found to be 85 nm thick. All the thin films deposited were found to be amorphous and a characteristic plot of the grazing incidence x-ray data is shown in Figure 4-2. The angle of incidence for the measurement was 0.8° . The x-value in ' VO_x ' (obtained from the RBS analysis) increased linearly from 2.2 to 2.4 as the partial pressure was increased from 1×10^{-6} Torr to 2.1×10^{-6} Torr.

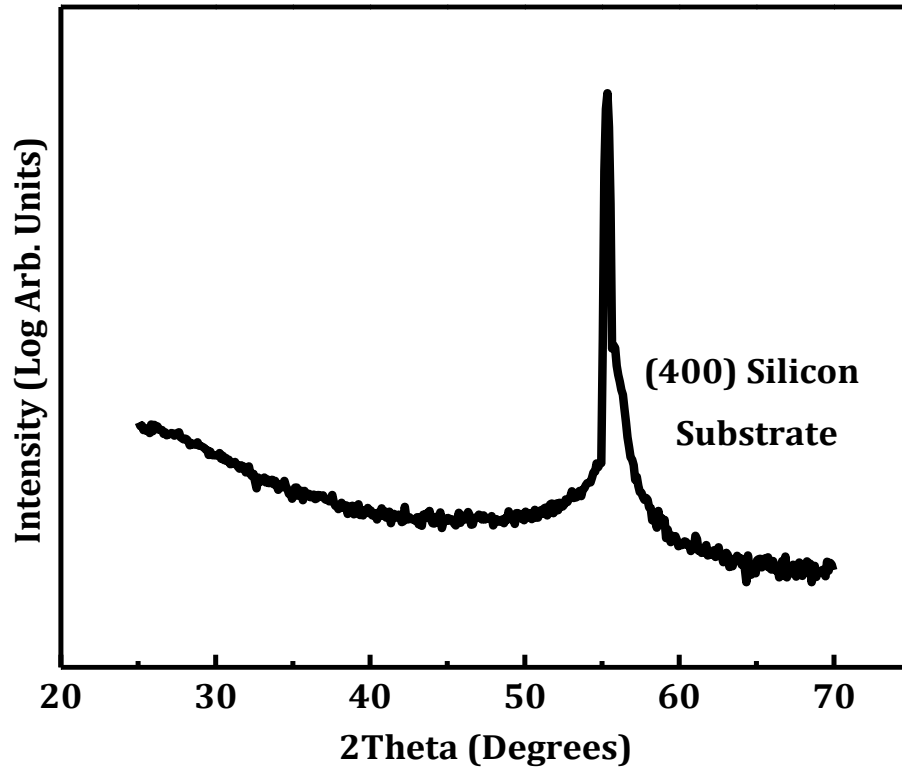


Figure 4-2. Grazing incidence X-ray diffraction spectra associated with high resistivity VO_x thin films deposited at high partial pressure of oxygen using Biased Target Ion Beam Deposition showing amorphous thin film structure.

The samples show a temperature dependent resistivity which is dominated by thermal activation at least in the range of 300 K – 350 K. The magnitude of TCR was calculated by extracting the thermal activation energy (E_a) from material's resistivity-temperature plots.

The room temperature TCR is given by:

$$TCR = - \frac{E_a}{k_b T^2} \quad \text{Equation 24}$$

Where E_a is the extracted activation energy, k_b is the Boltzmann's constant in eV and T is room temperature or 300 K.

The 1/f noise of the thin film samples was evaluated using Hooge-Vandamme relation given by [28] [82]:

$$\frac{S_I(f)}{I_{bias}^2} = \frac{\alpha_H}{nVf} \quad \text{Equation 25}$$

where $S_I(f)$ is the spectral current density, I_{bias} is the sample current, V is the volume of the sample, f is frequency range of measurement, α_H is Hooge's parameter and n is the carrier concentration. Since the volume and the bandwidth of measurement are chosen on a system level, the parameter ' α_H/n ' (normalized Hooge's parameter) was used as a measure of evaluating the $1/f$ noise of the samples.

To extract the normalized Hooge's parameter, samples having different volumes were lithographically patterned and biased using a voltage source in a shielded iron box. A low noise current amplifier (Stanford Research Model –570) was used to amplify the measured current power spectral density (PSD) which was recorded using a National Instruments data acquisition card (NI-6036E). The recorded PSD was converted into the frequency domain by using the Fast Fourier Transform function in LabVIEW. When normalized for volume, the three curves overlap as predicted by the Hooge-Vandamme relation. Similarly, the bias dependence of noise was also confirmed by applying three distinct biases. The measured power spectral density at 1 Hz (also referred to as the k -value) was multiplied by the sample volume to determine the normalized Hooge's parameter, or ' α/n ' value of our thin film.

Figure 4-3 shows the resistivity, TCR and α_H/n ($1/f$ noise) of the deposited films as a function of pO_2 . As expected, the resistivity of the deposited films increases as a function of pO_2 , reaching 20,000 Ω -cm at an oxygen partial pressure of 2.1×10^{-6} Torr. The TCR and the characteristic $1/f$ noise of the films followed no particular trend. The $|TCR|$ was a maximum of 5%/K for the film deposited with a pO_2 of 1×10^{-6} Torr while the α_H/n was found to be the lowest for the film deposited at 1.79×10^{-6} Torr with a value of 1×10^{-20} cm³. In other material systems, the inherent noise of the amorphous semiconductor has been associated with the short-range order in the amorphous material [83].

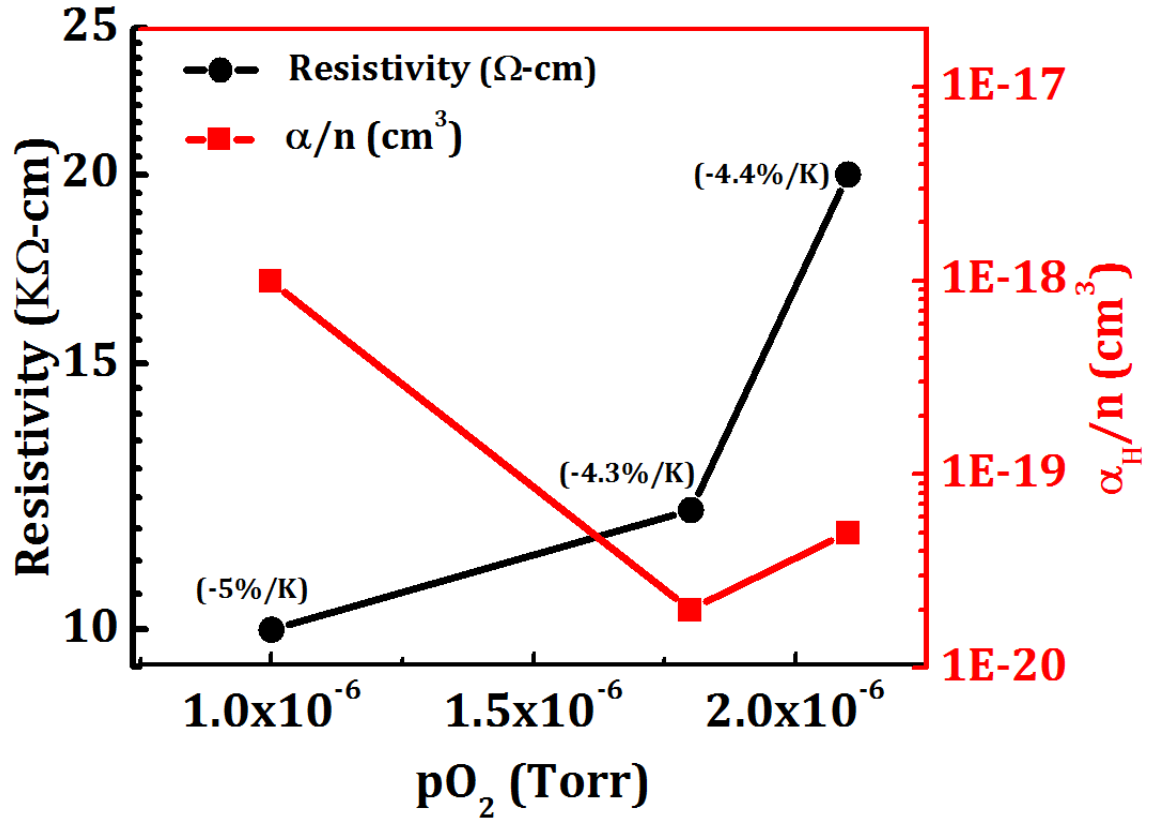


Figure 4-3. Resistivity, temperature coefficient of resistance (TCR) and the normalized Hooke's parameter (α_H/n) of VO_x thin films deposited by BTIBD as a function of partial pressure of oxygen (pO_2).

Regardless of the deposition conditions, the lowest resistivity deposited for the high TCR material was $> 10,000 \Omega\text{-cm}$. This limitation put the high resistivity VO_x material system at a disadvantage when compared with Si:H thin films even for use in constant bias readout integrated circuit bolometer cameras. Although this resistivity is higher than the currently used a-Si:H thin films for constant bias bolometer devices, their α_H/n values are on the order of those of Si:H thin films. A reduction in the total device resistance might make these thin films competitive for use in constant bias bolometer devices.

None the less, the magnitude of TCR, noise and resistivity observed for some of the thin films of VO_x of this work are better than other materials with high TCR such as spinels based on transition metal oxides and hydrogenated silicon as manufactured by L-3 communications [18] and ULIS [84].

4.3. High TCR Mixed Phase Thin Films of Ge:H

4.3.1. Experimental Details

A series of mixed phase amorphous + nanocrystalline hydrogenated germanium ((a+nc)-Ge:H) thin films having different thicknesses (thickness = 7 nm – 200 nm) were deposited onto c-Si wafers coated with 20 nm of silicon nitride by RF ($f = 13.56$ MHz) plasma enhanced chemical vapor deposition (PECVD) using ultra-high purity germane (GeH_4) gas diluted with H_2 . A number of deposition parameters were fixed along the lines of previous work including: a total pressure of ~ 93 Pa and a low plasma power density of 0.08 W/cm^2 . The background pressure was typically $< 5 \times 10^{-5}$ Pa. To facilitate an earlier nucleation of crystallites, the substrate was held at a temperature of 170°C and the hydrogen-to-reactive gas dilution ratio was maintained at $R = [\text{H}_2]/[\text{GeH}_4] = [160 \text{ sccm}]/[0.4 \text{ sccm}] = 400$.

To extract the electrical properties such as resistivity and TCR, the deposited thin films of Ge:H were patterned by photolithography and wet etching in a 30% H_2O_2 solution. Top contacts were made to the patterned thin films by photolithography and lift-off of sputter deposited chromium. The thickness of deposited Ge:H thin films were measured using an AFM, Dimension Icon made by (Bruker Corporation) on lithographically patterned steps in the thin films. The contact quality and thin film resistivity was evaluated using transmission line measurements on these lithographically patterned samples. As expected, the samples show a temperature dependent resistivity which is dominated by thermal activation at least in the range of 300 K – 350 K. The magnitude of TCR was calculated by extracting the thermal activation energy (E_a) as described in the previous sub-section.

4.3.2. Results and Discussion

Figure 4-4 shows the measured resistivity and TCR of the samples as a function of thickness. Starting with the 7 nm thin film, the magnitude of TCR increased from 1.8%/K to a value of about 6.5%/K for the 100 nm thick film. The 200 nm film showed a decrease in $|\text{TCR}|$ from the 100 nm film to about 3.6%/K. The resistivity of these films was between $750 \text{ }\Omega\text{-cm}$ and $4,500 \text{ }\Omega\text{-cm}$. Of particular interest are the films of thicknesses 50 nm and 100 nm which show a $|\text{TCR}|$ of 5%/K and 6.5 %/K for a

resistivity of about 1,500 $\Omega\text{-cm}$ and 2,250 $\Omega\text{-cm}$ respectively. To verify reproducibility of results, the 100 nm thin film was re-deposited with similar results, as can be seen in the graph.

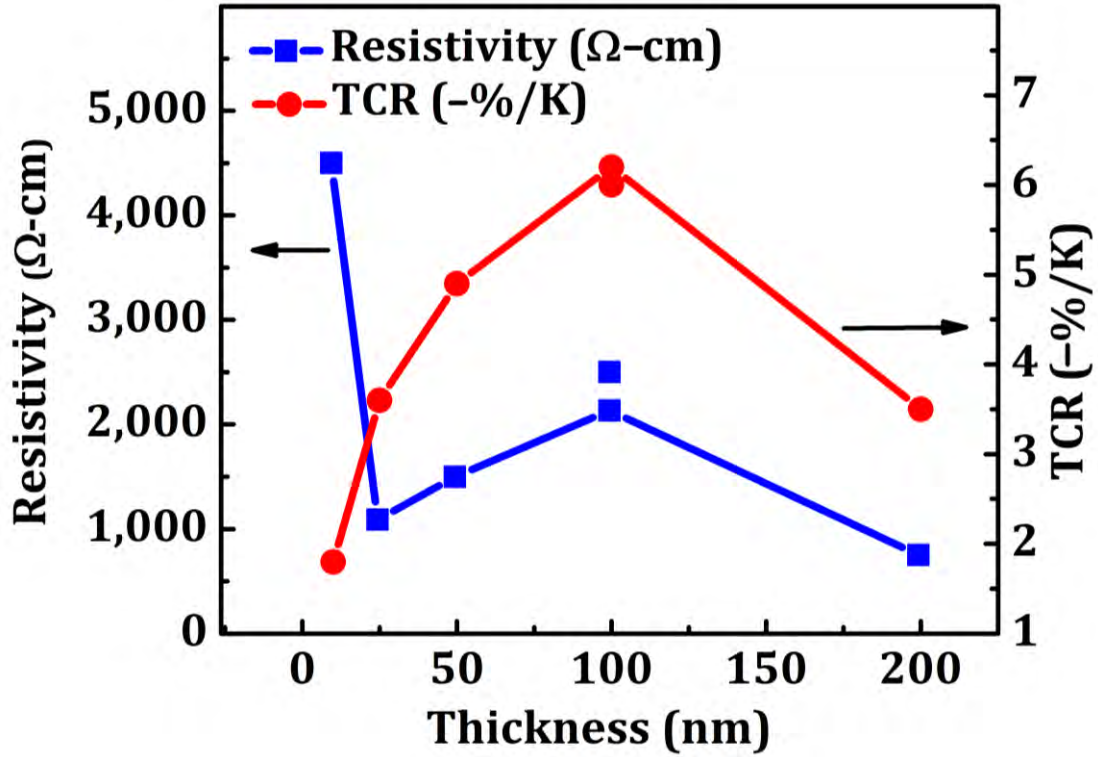


Figure 4-4. Resistivity and TCR of lithographically patterned samples of Ge:H as a function of thickness. The electrodes used for electrical measurements were evaluated to ensure ohmic contacts were obtained for all measurements.

The $1/f$ noise of the thin film samples was evaluated using the Hooge-Vandamme relation as described in the previous sub-section. Figure 4-5 shows the measured power spectral density (PSD) of a 100 nm film of Ge:H deposited in this work, confirming the volume dependence in these thin films. The y-intercept at a frequency of 1 Hz can then be used to extract α_H/n value of that thin film.

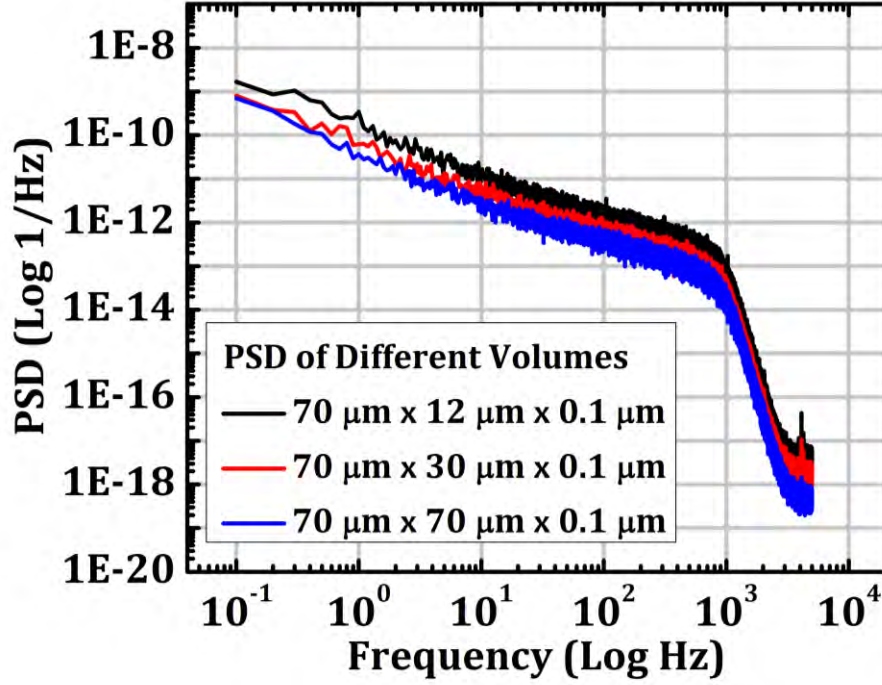


Figure 4-5. The measured Power Spectral Density (PSD), S_I^2/I_{bias}^2 , for the 100 nm sample of Ge:H showing volume dependence as predicted by the Hooge-Vandamme relation.

Figure 4-6 shows the extracted α_H/n values for the thin films of this work as a function of thickness. The $1/f$ noise for the 7 nm thick film could not be measured accurately. One possible reason for this high drift might be a resistance variation due to Joule heating of the thin film having a small cross-section for current flow (due to extremely small thickness). These values were found to be between 10^{-18} cm^3 (25 nm) and 10^{-20} cm^3 (100 nm) for the films. Interestingly, the film having the largest TCR value was also found to have the lowest α_H/n value, while the film with the lowest TCR was also found to have the highest α_H/n value.

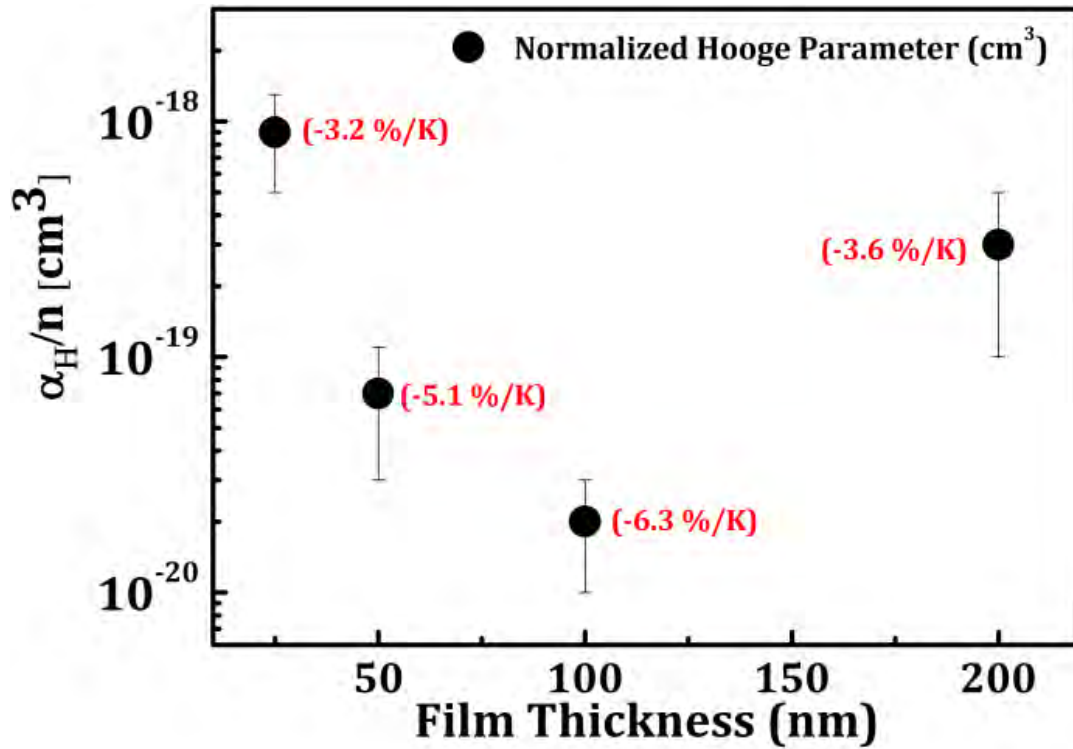


Figure 4-6. Extracted normalized Hooke's parameter ' α_H/n ' as a function of thickness for thin films of Ge:H each annotated with their corresponding value of TCR. Note that the 100 nm thin film had the lowest α/n value while having the highest TCR.

In an effort to explain the combination of high TCR and low 1/f noise in thin films of PECVD deposited Ge:H, the thin film microstructure was characterized. The crystal structure of the thin films was evaluated by grazing incidence X-ray diffraction using PANalytical's X'Pert Pro MPD with a step size of 0.026 degrees at a rate of 1.2 degrees/minute. Figure 4-7 shows the x-ray diffraction spectra for the 200 nm thin film grown on thermally oxidized silicon wafers. The data shows the presence of diamond cubic structure as expected from high dilution ratio during PECVD.

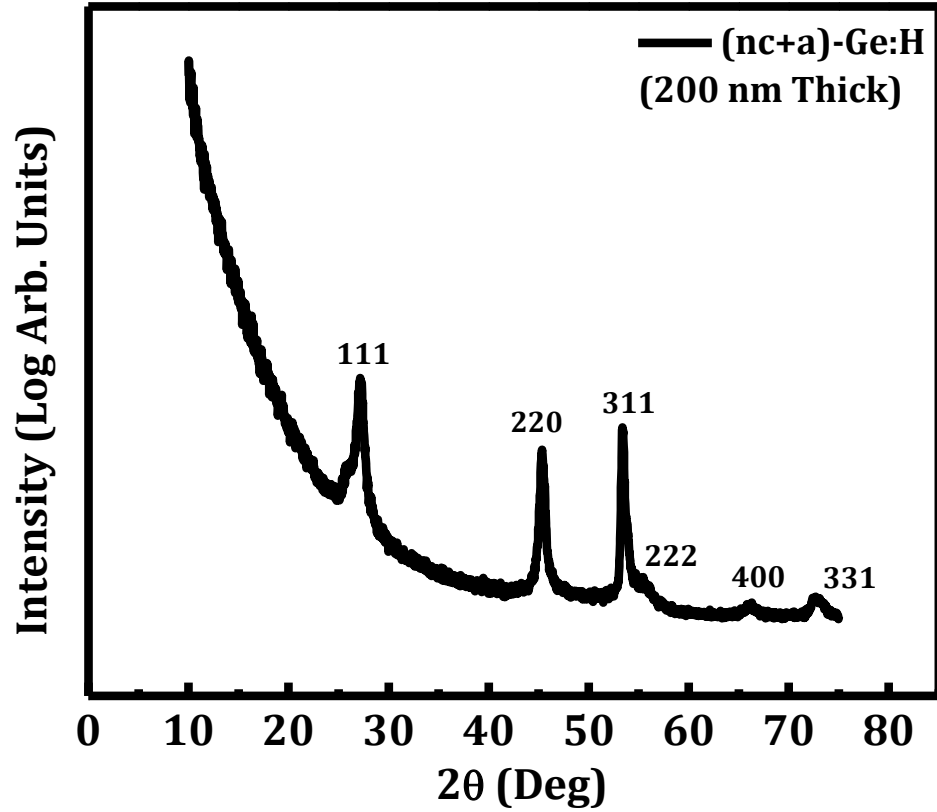


Figure 4-7. Grazing incidence x-ray diffraction pattern of a 200 nm thin film of Ge:H confirming the presence of diamond cubic crystal phase (as indexed).

To extract a first order estimate of the crystal size of the grains, the diffraction pattern for the 200 nm thick film was also collected in the Bragg-Brentano geometry, as shown in Figure 4-8. The first order grain size of the crystallites present in the films can be obtained using Scherrer's formula [85]:

$$D_p = \frac{0.94\lambda}{\beta_{1/2} \cos \theta} \quad \text{Equation 26}$$

where D_p is the calculated grain size, λ is the wavelength of radiation used for diffraction (1.54 Å); $\beta_{1/2}$ is the angle at full width half maximum. Using the Scherrer's formula, the grain size for this film was calculated to be about 140 nm.

An even thicker sample (250 nm) was deposited on a native oxide coated c-Si wafer for TEM analyses (albeit at a slightly higher temperature of 200 °C as opposed to 170 °C). Figure 4-9 shows a dark field TEM micrograph collected by Dr. David Saint John from the sample which shows that initial layers of the Ge:H are amorphous [19].

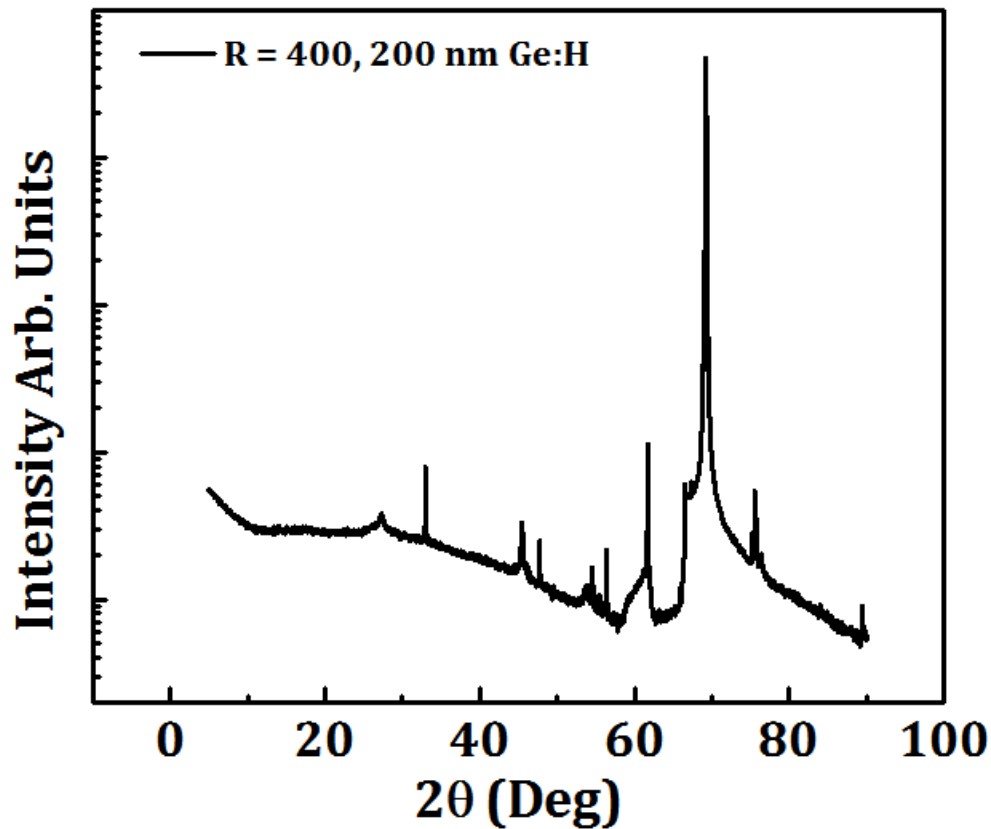


Figure 4-8. Bragg-Brentano x-ray diffraction pattern of the 200 nm thin film of Ge:H used to extract the size of crystals to the first order using the Scherrer's formula.

Around a bulk thickness of 10–15 nm, nanocrystallites start to nucleate and continue to grow segregated in an amorphous matrix until a thickness of around 100 –120 nm when these grains coalesce. In addition, the planar twinning defects with a regular periodicity of ~ 1 nm were also observed in this thin film.

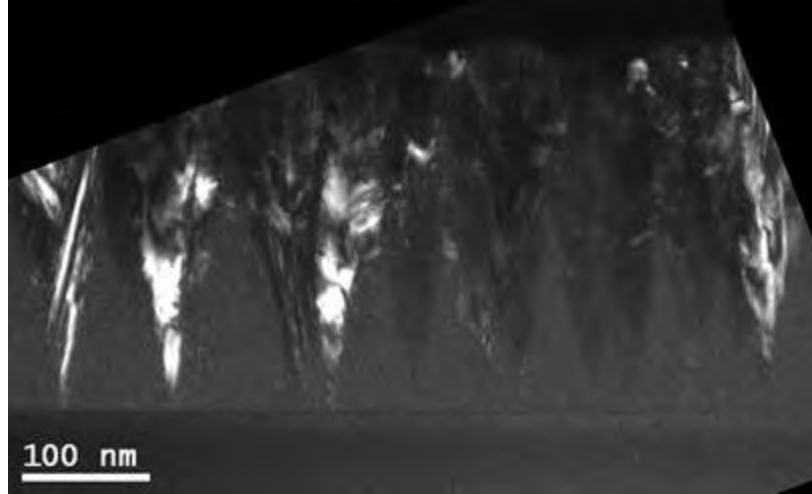


Figure 4-9. Dark field TEM micrograph of a 250 nm thin film of Ge:H showing the presence of nanocrystallites in an amorphous matrix [published previously in ref. [19].

The roughness of the thin films as a function of thickness was evaluated using an AFM. Figure 4-10 shows AFM micrographs of thin film of Ge:H with a thickness of 7 nm and 200 nm. Figure 4-10a shows the 7 nm thin film having a peak-to-valley height of 7nm having small island sizes. In contrast Figure 4-10b shows the 200 nm film has a much larger grains (> 50 nm).

Figure 4-12 illustrates the surface roughness evolution (both RMS and peak-to-valley) of the thin films of varying thicknesses deposited in this work. The RMS roughness of the films < 25 nm thick is around $8 \text{ \AA} - 9 \text{ \AA}$. The 100 nm thin film shows the highest roughness with an RMS value of 2.7 nm and a peak-to-valley height of 15 nm. Such a texture evolution is typical of growing crystallites and has been noted in Ge:H and Si:H/SiGe:H material system by numerous authors [15] [86] [72] [87]. For a film thickness of 200 nm, the RMS roughness decreases to about 2nm (peak-to-valley height of 12 nm).

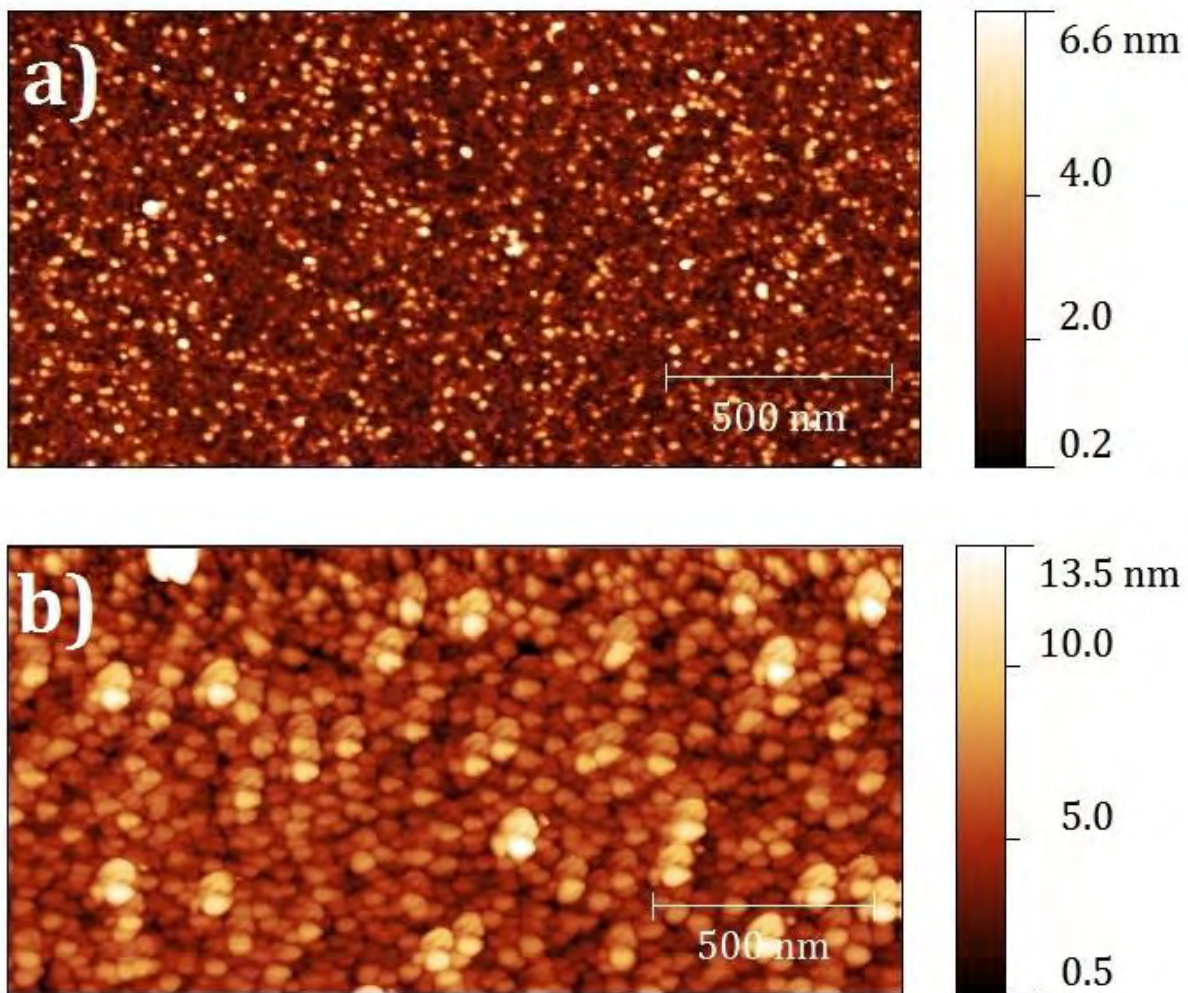


Figure 4-10. AFM micrographs of Ge:H thin films with thicknesses a) 7 nm and b) 200 nm presenting differences in surface morphology. The 200 nm thin film shows larger grains and larger peak-to-valley heights than the 7 nm thin film

Figure 4-11 shows a detailed three-dimensional image obtained for the 100 nm thin film of Ge:H. Clusters of Ge:H can be seen protruding from the surface of the film which results in the larger peak-to-valley height of 15 nm as measured for this thin film.

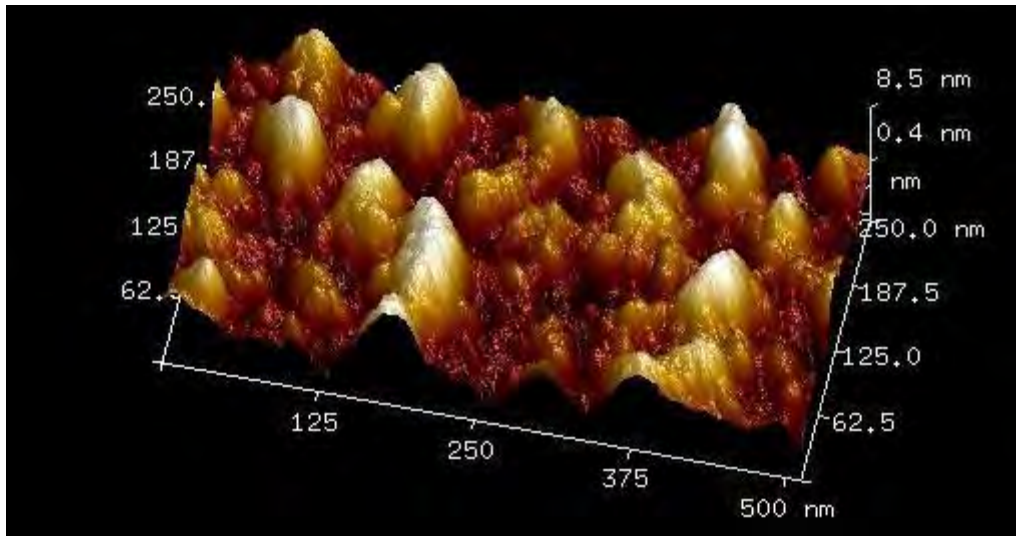


Figure 4-11. A three dimensional AFM micrograph showing the peak-to-valley roughness associated with the large grain sizes for the 100 nm thin film of Ge:H deposited in this work.

The presence of nanocrystallites in films thicker than 20 nm is confirmed in the electrical resistivity data. While amorphous germanium has been observed to have a resistivity as high as $10^7 \Omega\text{-cm}$, crystalline germanium has a resistivity of about $50 \Omega\text{-cm}$. The incorporation of these nanocrystallites lowers the resistivity of the films to about $750 \Omega\text{-cm}$ for the films in which the crystalline grains have coalesced. The increase in the resistivity and TCR for increasing film thicknesses is unexpected especially because the fraction of nanocrystallites is increasing with increasing thickness. To shed light on this behavior, the thin films were characterized using Real Time Spectroscopic Ellipsometry or RTSE.

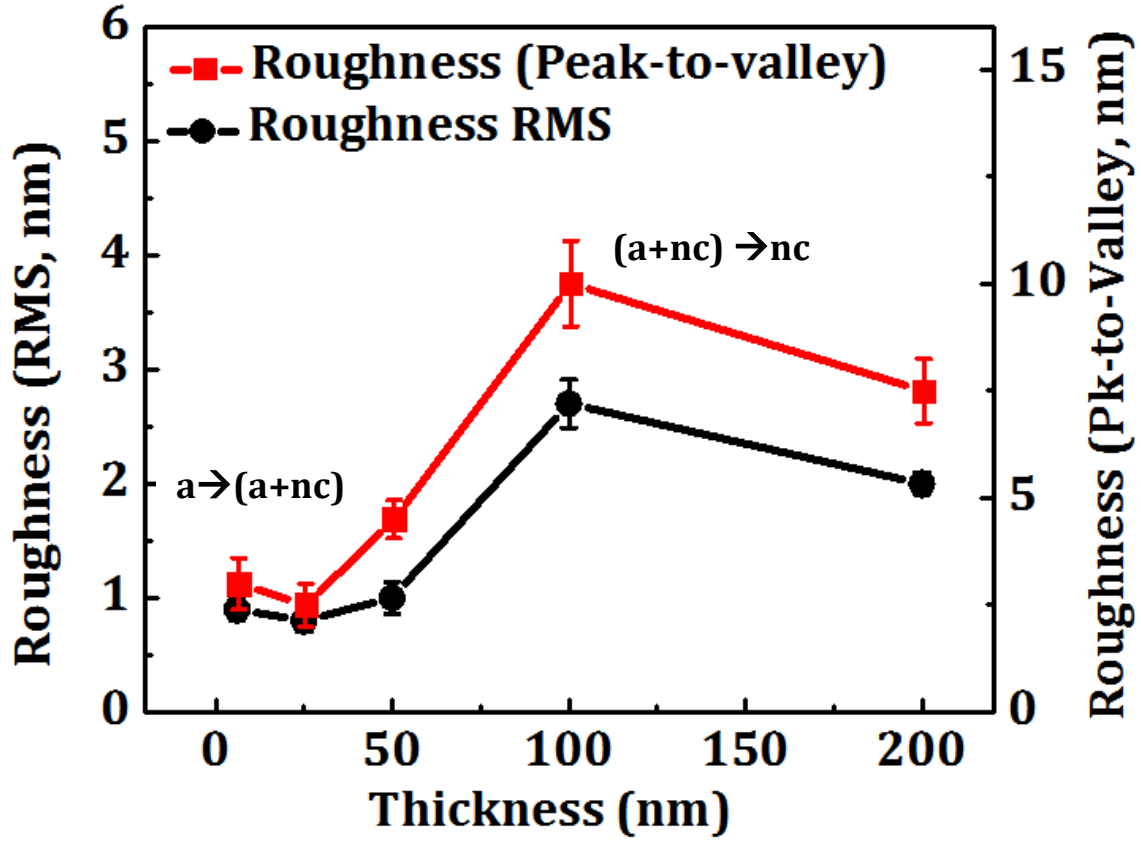


Figure 4-12. Peak to valley height (red) and RMS roughness (black) of thin films of Ge:H deposited in this work.

RTSE data was analyzed by a global $\Sigma\sigma$ -minimization procedure to obtain optical properties, in the form of the complex dielectric function spectra $\varepsilon = \varepsilon_1 + i\varepsilon_2$, and the time dependence of the bulk layer (d_b) and surface roughness (d_s) thicknesses while the film remains in the amorphous growth regime [88]. After crystallite nucleation occurs, virtual interface analysis (VIA) is used to obtain ε for the nanocrystalline phase and the time dependence of d_s and the nanocrystallite fraction (f_{nc}) [89] [90] [91]. In the mixed-phase amorphous + nanocrystalline (a + nc) regime, VIA uses a Bruggeman effective medium approximation [92] consisting of variable fractions of ε for a-Ge:H and nc-Ge:H to represent the optical response of the outermost 1.5 nm of the growing film. From this information, a depth profile in crystallinity can be determined.

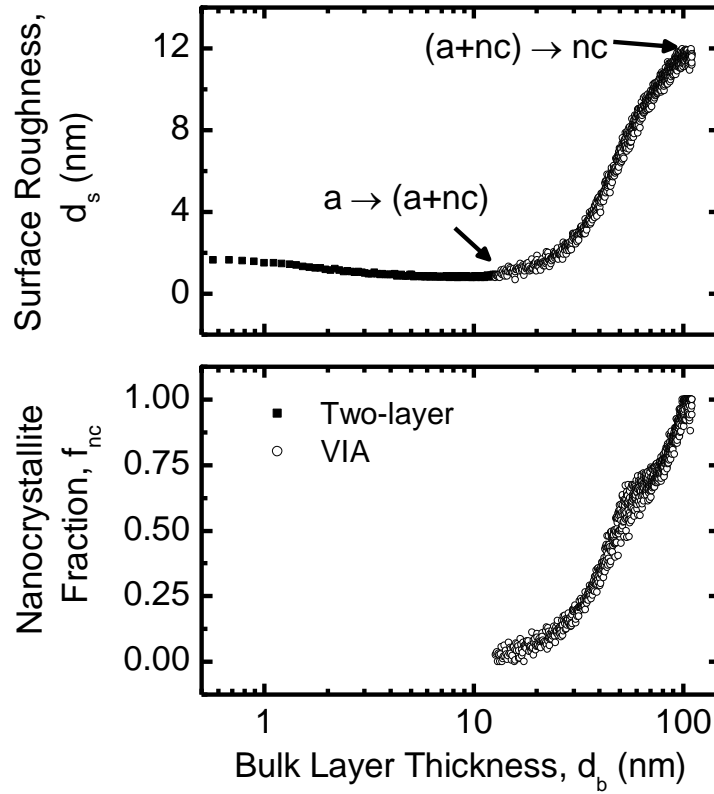


Figure 4-13. Surface roughness and nanocrystallite fraction for Ge:H on native oxide coated crystalline silicon (c-Si) obtained from two layer modeling and virtual interface analysis (VIA) of real time spectroscopic ellipsometry (RTSE) measurements. The nanocrystallite fraction profile used in the analysis of the single final set of spectra is also shown.

The RTSE data analysis was led by Dr. Nikolas Podraza from The University of Toledo, Toledo, Ohio. The results of RTSE data analysis are provided in Figure 4-13. The film remains amorphous with d_s initially decreasing and reaching a minimum value prior to the amorphous-to-mixed-phase transition [$a \rightarrow (a + nc)$] at $d_b = 13$ nm. Afterward, f_{nc} and d_s begin to increase as nanocrystallites grow preferentially over the surrounding amorphous phase. Coalescence of nanocrystalline clusters occurs when $f_{nc} = 1$, d_s reaches a maximum, and is called the mixed-phase-to-single-phase nanocrystalline transition [$(a + nc) \rightarrow nc$] at $d_b = 100$ nm. After the $(a + nc) \rightarrow nc$ transition, d_s decreases slightly as a single phase nanocrystalline layer is formed and protruding clusters coalesce.

The initial decrease in resistivity could be due to the initial nucleation of crystallites or enhanced ordering of protocrystalline Ge:H prior to the onset of crystallinity. Resistivity, however, subsequently

increase with f_{nc} , reaches a maximum near the $(a + nc) \rightarrow nc$ transition, then decreases. An explanation for this behavior is that while the initial appearance of more conductive crystallites reduces film resistivity, subsequent evolution introduces a significant amount of grain boundary material into the film. Poorly passivated grain boundaries can act as oxidation pathways post-deposition as the films are exposed to atmosphere, thereby increasing resistivity.

Figure 4-14 shows variations in ε for the nanocrystalline component of the nominally 100 nm film deposited on native oxide coated c-Si, monitored by RTSE, and characterized by ex situ spectroscopic ellipsometry post-deposition. RTSE VIA analysis yielded $a \rightarrow (a + nc)$ and $(a + nc) \rightarrow nc$ transition thicknesses as well as ε for a-Ge:H and nc-Ge:H in vacuum at the deposition temperature. The final RTSE data point was analyzed using these reference ε and a structural model incorporating a 13 nm continuous amorphous layer, a 93 nm mixed-phase layer with nanocrystallite fraction incorporating an exponential gradient shown in Figure 4-13, a 15 nm continuous nanocrystalline layer, and a 12 nm surface roughness layer in accord with VIA results. These structural parameters were fixed and used to fit ex situ ellipsometric spectra collected from the same sample after exposure to atmosphere at room temperature. The temperature dependence of ε for c-Si is known [93] and that for a-Ge:H was obtained from in situ spectroscopic ellipsometric monitoring of a 60 nm thick film prepared at $T = 200$ °C and $R = 120$ which remains amorphous.

Spectra in ε for a-Ge:H can be described using the Cody-Lorentz oscillator model [94] in terms of energy independent parameters including an amplitude (A), broadening (Γ), resonance energy (E_0), band gap (E_g), partition energy (E_p), and constant additive term to ε_1 ($\varepsilon_\infty = 1$). The temperature dependence of E_g , E_p , and A were identified as $dE_g/dT = -0.000411$ eV/K, $dE_p/dT = -0.000617$ eV/K, and $dA/dT = -0.02$ eV/K, respectively, which are in reasonable agreement with previous results for hydrogenated amorphous silicon germanium alloys [95]. Variations in Γ and E_0 were not greater than the error limits within this temperature range and were fixed. Spectra in ε obtained from RTSE for $R = 400$ a-Ge:H prior to

nanocrystallite nucleation was parameterized using the Cody-Lorentz model at the deposition temperature, and room temperature ε was simulated using these temperature dependencies to assist in fitting ex situ ellipsometric measurements of nominally 100 and 200 nm thick films. Spectra in ε for nc-Ge:H were parameterized using three Tauc-Lorentz oscillators [96] [97].

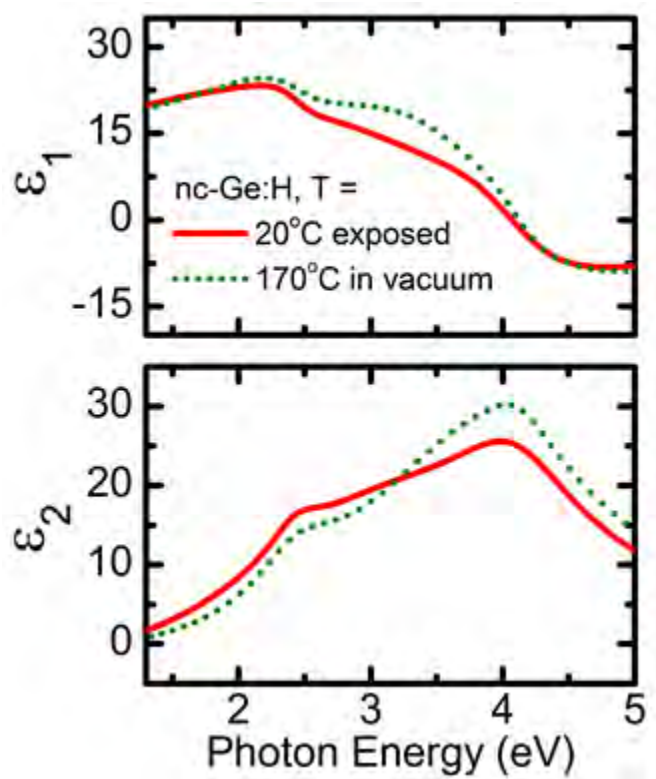


Figure 4-14. Complex dielectric function, $\varepsilon = \varepsilon_1 + i\varepsilon_2$, spectra for nanocrystalline Ge:H (nc-Ge:H) obtained in situ, in vacuum from virtual interface analysis of RTSE data and obtained ex situ, after atmospheric exposure.

Differences in ε for nc-Ge:H are expected with differences in temperature, although typically critical point broadening decreases and amplitude increases at lower temperatures for crystalline materials [93]. The data shown in Figure 4-14 shows an increase in broadening and decrease in amplitude, particularly for the higher energy critical point feature. This variation is consistent with partial oxidation of a material. When ε obtained at room temperature after atmospheric exposure is treated as a pseudodielectric function and fit to a structural model consisting of un-oxidized nc-Ge:H, in this case ε obtained in vacuum, and an overlayer of germanium oxide [98], the overlayer thickness is 1.5 nm thick.

This model is a gross simplification, but it also seems to indicate that some fraction of the nc-Ge:H has oxidized.

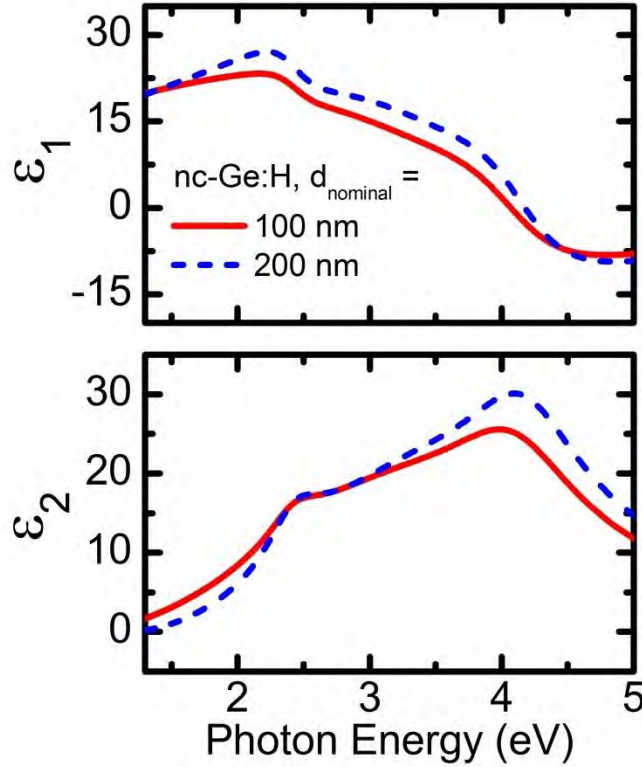


Figure 4-15. Spectra in ϵ for nc-Ge:H obtained ex situ, after atmospheric exposure for nominally 100 and 200 nm thick films.

Figure 4-15 shows a comparison of ϵ obtained at room temperature, after atmospheric exposure for the nominally 100 nm film on native oxide coated c-Si and nominally 200 nm film on SiN_x coated c-Si. Although the substrate is different, previous studies indicate that the $a \rightarrow (a + nc)$ transition occurs at similar thicknesses for Ge:H, as given in Figure 4-15. The features in ϵ for the thicker film are sharper and have a larger magnitude, indicating that grain size has increased, the amount of grain boundary material has been reduced, and/or a smaller fraction of the film has oxidized.

A proposed model describing the variations in resistivity and TCR relies on nanocrystalline grain boundaries acting as oxidation pathways. At low crystalline content as in the nominally 25 nm thick film, improved ordering in the amorphous phase may lower film resistivity. When crystallites begin to occupy a significant fraction of the surface, as in the 50 and 100 nm films, resistivity increases as the grain

boundaries enable the internal crystallite surfaces to oxidize. At greater thickness, the increase in grain size and reduction in grain boundaries again reduce resistivity since more interconnecting pathways between un-oxidized grains exist. The highest *TCR* is observed for the highest resistivity, which potentially consists of crystallites encompassed by higher resistivity germanium oxide material. This structure is similar to that of microbolometer device grade vanadium oxide, where low resistivity, small defective face centered cubic vanadium monoxide nanocrystallites are surrounded by higher oxygen content, higher resistivity material [43]. Similar vanadium oxide thin films also exhibit significant post-deposition oxidation as monitored by RTSE [99].

4.4. Conclusion

Thin films of VO_x and Ge:H having *TCR* values larger than 4%/K have been deposited in this work. Thin films of VO_x were found to be amorphous, with resistivity around 10,000 $\Omega\text{-cm}$ to 21,000 $\Omega\text{-cm}$ with α_H/n values between $\sim 10^{-18}$ and 10^{-20} cm^3 . Ge:H thin films were found to be amorphous or amorphous + nanocrystalline depending on thickness and dilution ratio of the film deposited. When deposited by PECVD using high dilutions of GeH_4 in H_2 , these films show nanocrystalline grain growth in an amorphous matrix. At thicknesses optimized for a dilution ratio, R of $[\text{H}_2]/[\text{GeH}_4]$, films 50 – 100 nm thick exhibit large *TCR* (5%/K – 6.4%/K) with reasonable values of α/n ($\sim 10^{-19}$ and 10^{-20} cm^3) having low resistivity (1,500 $\Omega\text{-cm}$ and 2,250 $\Omega\text{-cm}$). This superior combination of electrical properties was attributed to the incorporation of an optimal value of grain size and the crystal fraction of the germanium nanocrystallites.

Figure 4-16 shows a comparison of *TCR* versus resistivity of various thin films reported in the literature in comparison with thin films deposited in this work. Both Ge:H and VO_x thin films show the highest reported *TCR* for the resistivity $< 10,000 \text{ }\Omega\text{-cm}$. However, thin films of (nc+a)-Ge:H show a superior resistivity to *TCR* tradeoff in comparison with thin films of VO_x deposited in this work.

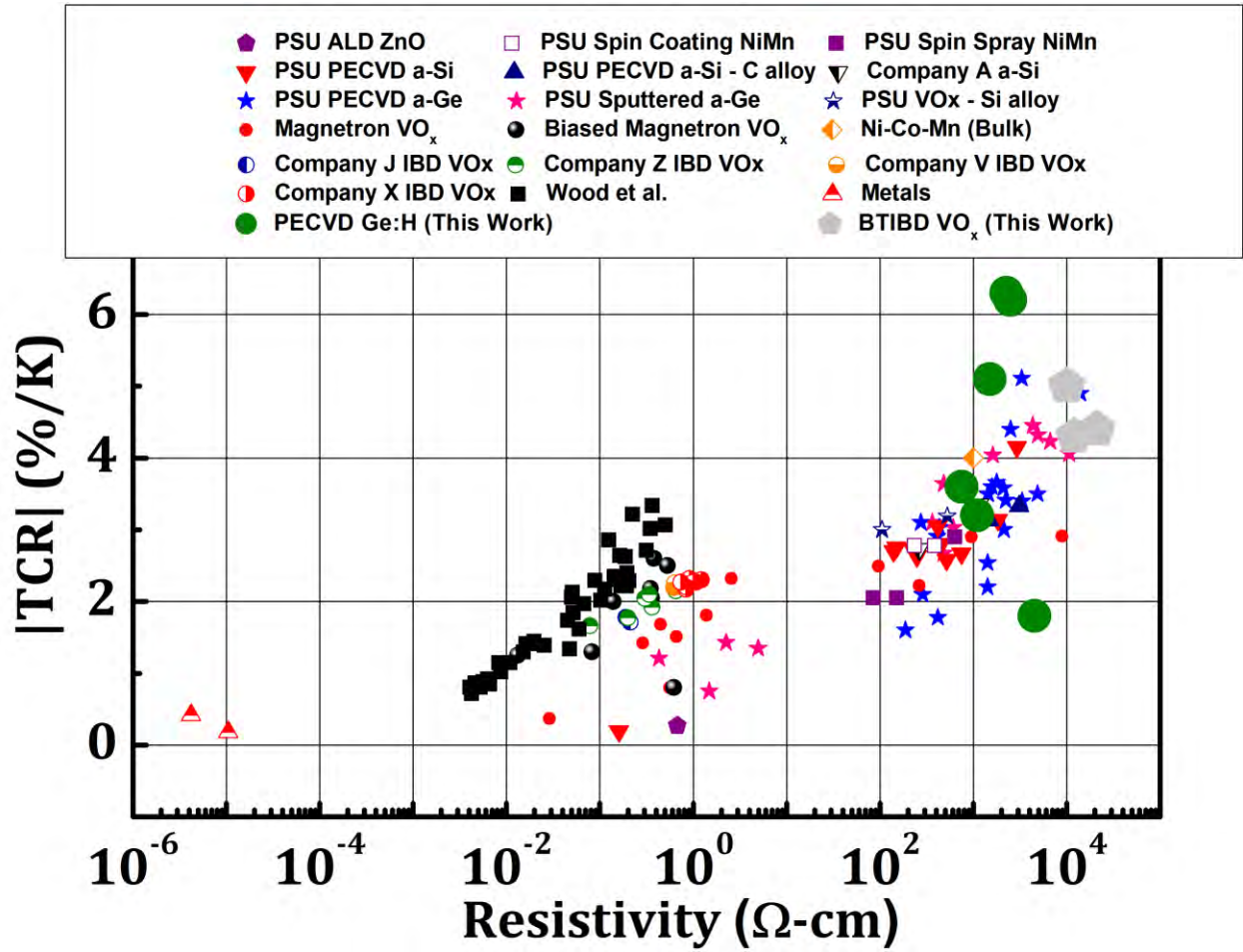


Figure 4-16. A comparison of Resistivity vs. TCR of thin films reported in literature to the thin films of Ge:H and VO_x deposited in this work.

However a more comprehensive figure of merit is the NETD which was discussed in Chapter 2. For a given material, the theoretical NETD is given by:

$$NETD \propto \frac{I_{noise, total}}{I_{bias} \times TCR} \quad \text{Equation 27}$$

Or,

$$NETD \propto \sqrt{\left(\frac{\alpha_H}{nVf}\right)} \times \frac{1}{TCR} \quad \text{Equation 28}$$

From equation 2 it is evident that a metric of comparison between different materials is the ratio of (α_H/n) to TCR^2 . Figure 4-17 gives a comparison of the normalized Hooke's parameter ' α_H/n ' versus TCR for different materials reported in the literature with the materials deposited in this work.

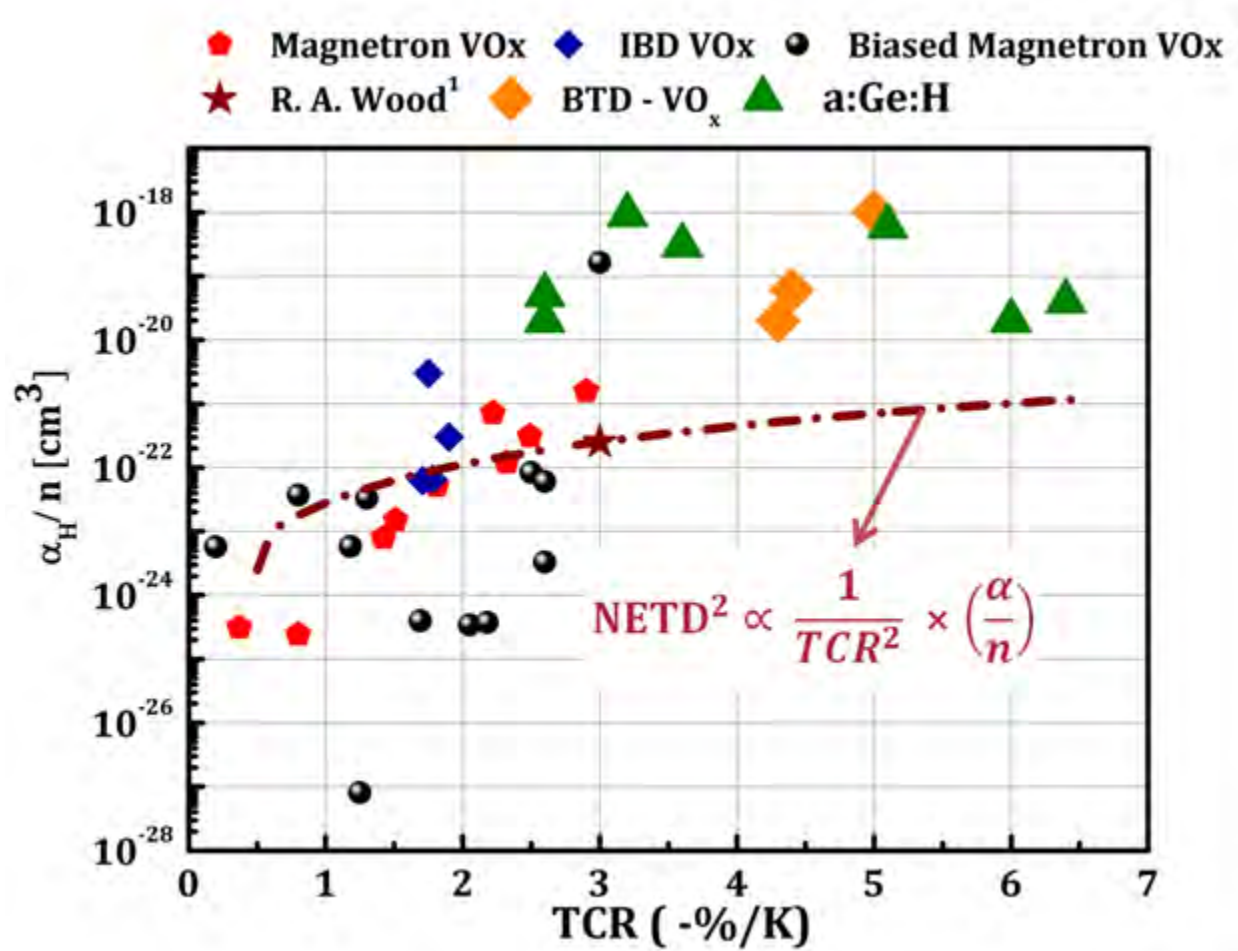


Figure 4-17. A comparison of the Normalized Hooke's parameter of some common materials reported in literature vs. thin films deposited in this work. The dotted line represents a constant ratio of $\alpha_H/n : TCR^2$.

The dotted line is a curve of an equipotential $NETD^2$. This curve shows the values which would give the same $NETD$ regardless of the fact that the TCR and noise values are changing between the thin films. This line shows that although films with higher TCR are deposited in this work, the tradeoff of TCR and noise is not sufficient for use of these high TCR materials in a pulsed bias geometry as with the VO_x microbolometer system. The real advantage in using these thin films can be obtained by advanced circuits such as those used in constant bias bolometer devices existing at L-3 communications. Both the

hydrogenated nanocrystalline + amorphous (nc+a)-Ge:H thin films and possibly VO_x thin films are potential candidates for high TCR materials used in constant bias microbolometers.

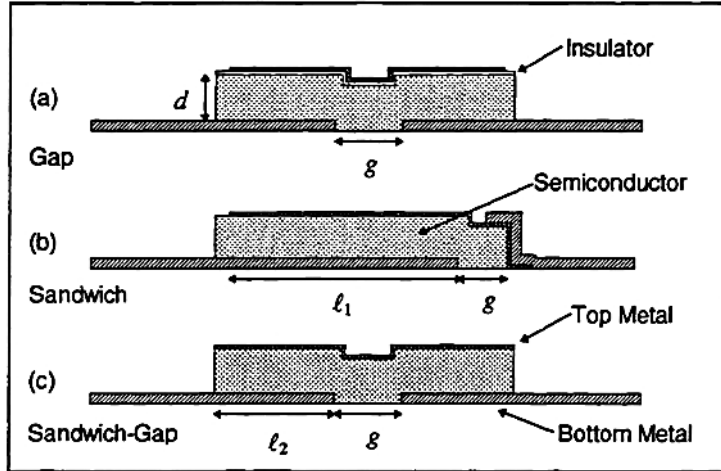
Chapter 5. High TCR Bolometers Using Vertically Integrated Thin Film Resistors

5.1. Introduction

Vanadium oxide (VO_x) and hydrogenated silicon germanium (SiGe:H) having a magnitude of TCR between 2%/K and 4%/K form an integral part of a majority of infrared imaging systems manufactured today [8] [30] [78] [100] [18]. The material properties of these thin films used in making uncooled infrared focal plane arrays has remained largely unchanged since some of the first investigations detailing their properties [8] [100] [18]. Most of the performance improvement in these devices has come from the evolution of the underlying read out circuits [101] [59] [102] [103] [104].

The current pixel structure in infrared imaging sensors employs a lateral resistor configuration with a square geometry in which the length and width of the sensing material is $17\text{ }\mu\text{m} \times 17\text{ }\mu\text{m}$. To minimize thermal mass and optimize performance, the thickness is kept to $\approx 50\text{nm}$ to 100 nm . Though high TCR materials are preferred, these materials typically have higher resistivities and therefore higher device resistance and noise associated with them. Existing materials with large values of TCR ($\sim 4\%/K$) typically have a resistivity larger than $2,000\text{ }\Omega\text{-cm}$ with higher TCR materials having even larger resistivities. Although higher TCR materials exist, they have not been incorporated into infrared focal plane arrays due to their higher resistivity ($> 100\text{ M}\Omega$) and higher noise in the lateral resistor configuration [50] [42] [51] [105] [106] [84].

To overcome this limitation, in this work, an alternate pixel design is investigated in which a high TCR material is incorporated into a structure having low device resistance. In the literature, only a few other device configurations have been explored which use the out of plane conductivity (or through film) as opposed to the lateral conductivity currently used in resistive bolometers. Figure 5-1 shows the three bolometer pixel designs explored by Unewisse et al. which are detailed in ref. [107]. These through film devices can have resistance values up to 10^5 smaller for the sandwich-gap type structures [107] [108].



$$R = \frac{\rho g}{wd}$$

gap

$$R = \rho \frac{dg}{w(d^2 + g\ell_1)}$$

sandwich

$$R = \rho \frac{2dg}{w(2d^2 + \ell_2 g)}$$

sandwich-gap

Figure 5-1. The three bolometer design structures explored by Unewisse et al. in ref. [107].

where ρ is the resistivity of the semiconductor material, g is the gap length, d is the thickness of the detector, w is the width of the detector, and ℓ_1 and ℓ_2 are the lengths of the bottom contact in the sandwich and the sandwich-gap type detectors, respectively.

Figure 5-1(a) shows the standard device structure used by the resistive microbolometer industry, whereas the detector of Figure 5-1(b) shows the sandwich type configuration in which the current flows in the transverse direction [107]. This greatly reduces the length to area ratio of the detector and hence the resistance. Due to the change in the length over area ratio associated with the through-film configuration, the resistance of a bolometer can be lowered ($R_{\text{in-plane}}/R_{\text{out-of-plane}}$) by up to a factor of 10^4 for $10 \mu\text{m} \times 10 \mu\text{m}$ pixel dimensions in a sandwich type configuration [107]. Another type of detector was named the Sandwich-gap type detector, as shown in Fig. 2(c), which essentially consists of two sandwich type elements in series, separated by a small gap [107]. In this configuration, the resistance could be reduced up to a factor of 10^5 [107]. Although these alternate designs were investigated at the Defense Science and Technology Organisation, in Australia from 1995 through 2003, there is a limited body of literature detailing the performance of microbolometers in this configuration [107].

In 2010, Moreno et al. investigated the electrical performance of the sandwich type structure and detailed it in ref. [108]. It was found that the sandwich structures had a higher level of electrical noise (5

orders of magnitude higher, 10^{-11} A/ $\sqrt{\text{Hz}}$ vs. 10^{-16} A/ $\sqrt{\text{Hz}}$ [108]. However, no reason was attributed to this higher level of noise. One possibility for the higher level of noise could be the higher electric field to which the sensing thin films were subjected. Indeed the ‘I–V’ curves of the biased sandwich structures was found to be nonlinear [108].

This work looks to fabricate sandwich type detector elements (referred to here as the through film device structures) with high TCR and high resistivity materials. The resultant through films structures are characterized for their electrical properties, especially their electrical noise.

Thin films of high TCR hydrogenated germanium (Ge:H, $|\text{TCR}| > 6\%/K$) and vanadium oxide (VO_x , $\text{TCR} > 5\%/K$) were integrated in lateral and through film configuration. The Johnson noise of the devices was reduced significantly while maintaining the same contribution of $1/f$ noise.

5.2. Theoretical Performance of Through Film Structures

An important figure of merit is the Noise Equivalent Temperature Difference or NETD, which can be used to compare the theoretical performance of the through film structures. The NETD is the measure of the sensitivity of an IR imaging system. It is defined as, “...the change in the temperature of a black body of infinite lateral extent which, when viewed by the thermal imaging system, causes a change in the signal-to-noise ratio of unity in the electrical output of the pixels of a focal plane array....” [17].

The NETD of a detector is given by [30] [17]:

$$NETD \propto \frac{I_{noise, total}}{I_{bias} \times TCR} \quad \text{Equation 29}$$

Where $I_{noise, total}$ is the resultant total electrical noise from an electrical bias I_{bias} . The ratio of $I_{bias}/I_{noise, total}$ is also known as the Signal to Noise Ratio or ‘SNR’.

When a microbolometer, dominated by the material noise, is biased using a voltage source, V_{bias} , producing a current I_{bias} the obtained SNR is given by [30]:

$$SNR = \frac{I_{bias}}{\sqrt{\frac{4\kappa T(f_2 - f_1)}{R_b} + I_{bias}^2 \frac{\alpha_H}{nV} \ln\left(\frac{f_2}{f_1}\right)}} \quad \text{Equation 30}$$

where κ is the Boltzmann's constant, T is the temperature of operation, f_1 and f_2 is the range of frequency for the bandwidth of operation, R_b is the electrical resistance of the bolometer, α_H is Hooge's parameter, n is the carrier concentration and V is the volume of the sample.

From Equation 29 and Equation 30, the NETD can be written as:

$$NETD \propto \frac{1}{SNR \times TCR} \quad \text{Equation 31}$$

To compare the electrical performance of the lateral and through film configurations, their TCR and the SNR must be evaluated. While the TCR of a device is an inherent property of the particular device and depends on the activation energy of the material used, the SNR depends on the electrical bias, applied to the device.

From Equation 30, the SNR increases for increasing bias values and reach a maximum when the device is operated at a bias level such that the $1/f$ noise dominates the total noise contribution. On the other hand the power dissipated across the thin film ($V_{bias}I_{bias}$) increases with increasing bias which may cause Joule heating of the thin film.

Due to these conflicting factors, a new set of bias conditions must be considered for this new configuration. Figure 5-2 shows calculated values of the power dissipated and the theoretical maximum values of SNR which can be achieved for the through film configuration with the following values:

Table 3. Parameters and their values used for estimating the SNR ratio and the power dissipated as a function of applied bias.

Parameter	Value
κ_b	$1.38 \times 10^{-23} \text{ m}^2.\text{kg}.\text{s}^{-2}.\text{K}^{-1}$
T	300 K
f_1	0.001 Hz
f_2	1 KHz
ρ	20,000 $\Omega\text{-cm}$
α_H/nV (k)	1×10^{-11}
Dimensions	17 $\mu\text{m} \times 17 \mu\text{m}$

A large voltage bias, similar to the one in the lateral configuration produces a bias current value 10^4 times larger than in the lateral configuration, causing a significant heating of the bolometer material leading to low frequency drift of the signal current [77].

The increase in the temperature of the bolometer due to the bias current is given by ΔT [30]:

$$\Delta T = \frac{V_{bias} I_{bias}}{c} \quad \text{Equation 32}$$

where ΔT is the rise in temperature of the bolometer per second of applied bias, and c is the heat capacitance of the bolometer material [30].

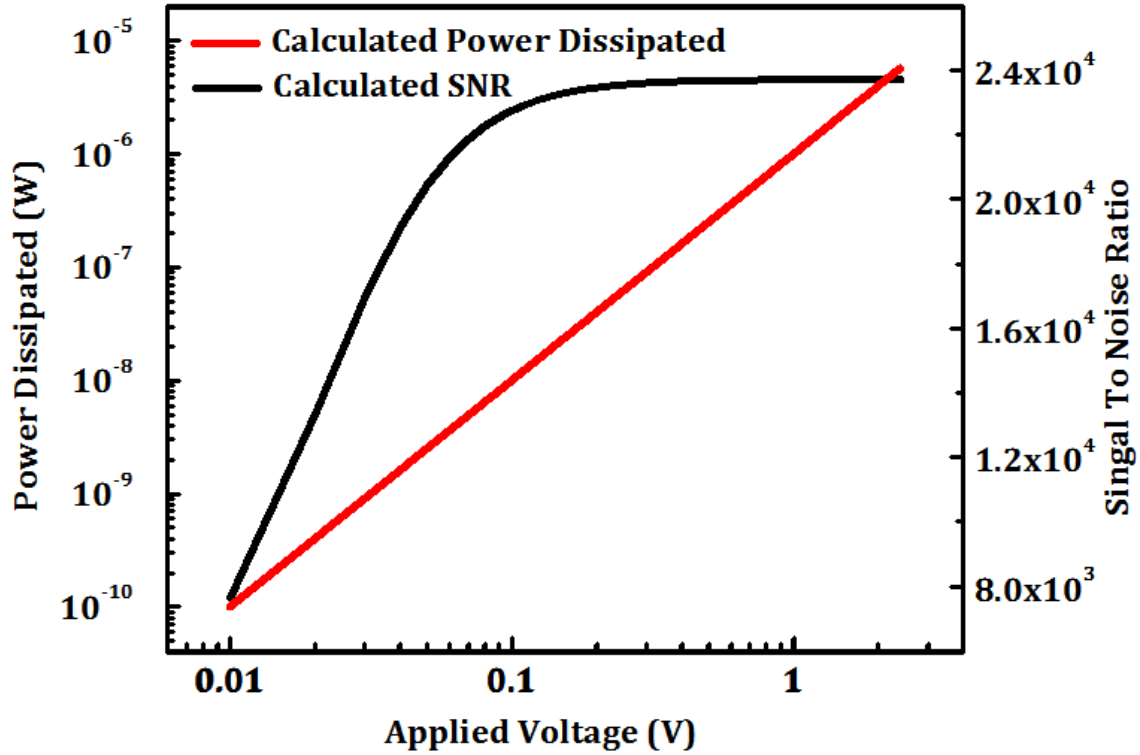


Figure 5-2. Graph showing theoretically calculated values of the power dissipated (red) and the maximum attainable signal to noise ratio (black) for a thin film device with a resistivity of 20,000 Ω -cm and dimensions of 17 $\mu\text{m} \times 17\mu\text{m}$.

While a large bias voltage may cause bias-induced heating, a low voltage bias may result in a low SNR (from Equation 30). Figure 5-2 shows that the SNR increases dramatically for low bias vales; which is also when the total noise is dominated by the Johnson noise of the bolometer. The SNR reached a maximum when the 1/f noise contribution in equation 1 dominates. **Thus it can be concluded that for the vertically integrated thin films the optimal bias level is the lowest voltage value for which the SNR has reached a maximum OR the bias value should be high enough so that the device performance is dominated by the 1/f noise and not by Johnson noise.**

5.3. Experimental Details

To compare the electrical performance of the through film structures to the conventional lateral configuration, both the lateral and through film configurations have been fabricated using thin films of

high resistivity and high TCR VO_x and Ge:H. The process steps for fabricating the devices are described in the following subsections.

5.3.1. Lithographic Fabrication of Device Structures

Figure 5-3 shows a schematic for the two device structures whose electrical properties were compared. The lateral resistors devices were processed as described in Section 3.3.7. Briefly: thin films having a high TCR were first deposited onto an electrically insulating substrates (100 nm thermally grown SiO_2 on c-Si for VO_x thin films and 20 nm LPCVD SiN_x for Ge:H). The TCR material is then isolated in a 1:2,000 $\text{H}_2\text{O}_2:\text{H}_2\text{O}$ solution, following which top electrodes are deposited by liftoff (titanium for VO_x and chromium for Ge:H).

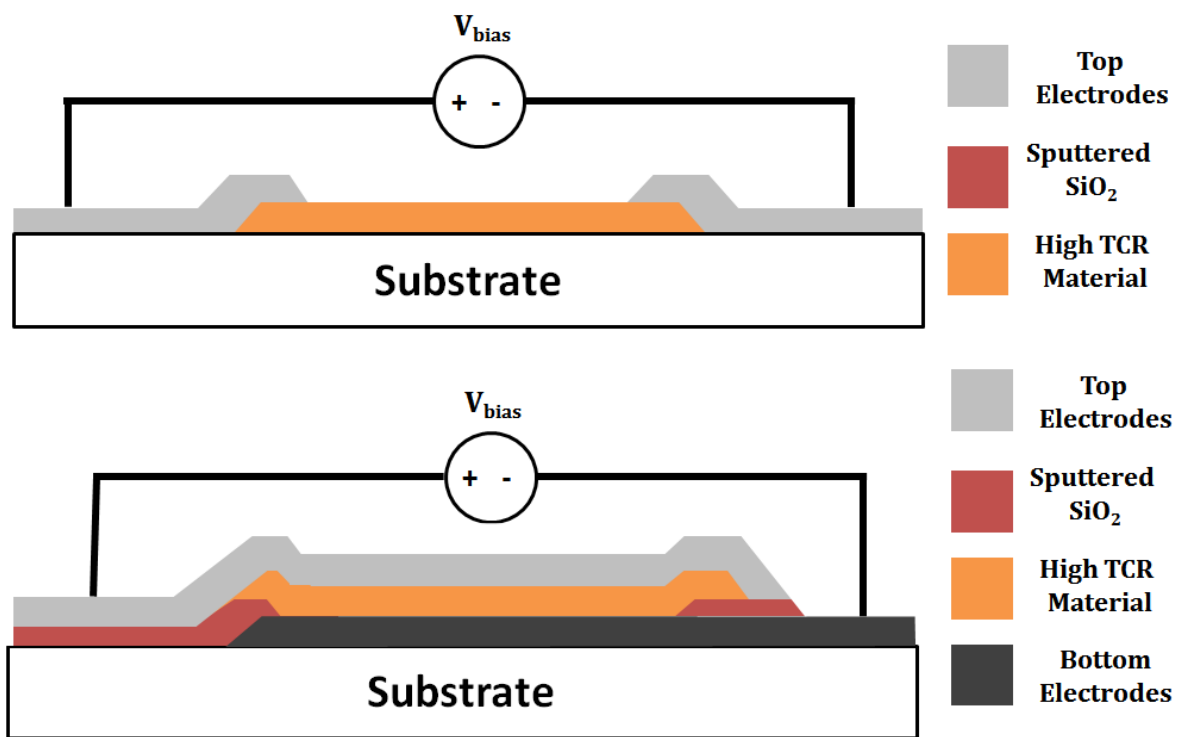


Figure 5-3. Cross-sectional schematic of bolometer configurations explored: a) In-plane conductivity (top); b) Out-of-plane conductivity (bottom).

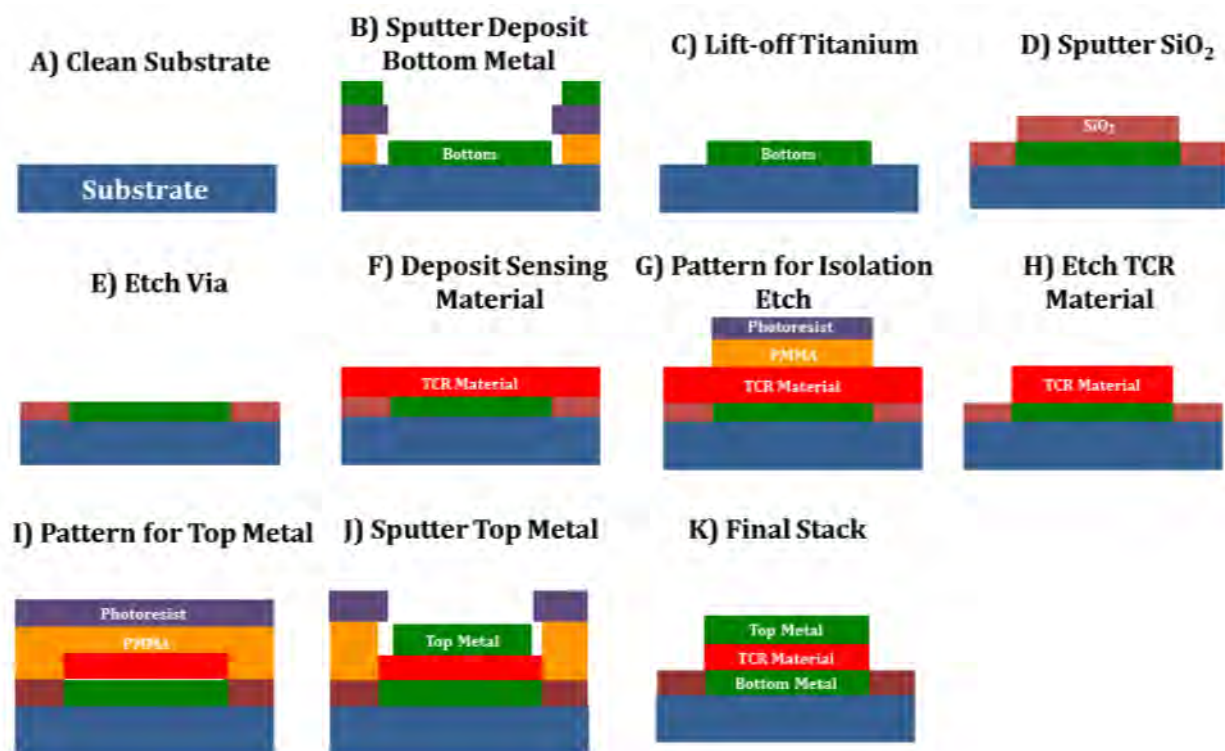


Figure 5-4. Lithographic processing for through film resistance structures.

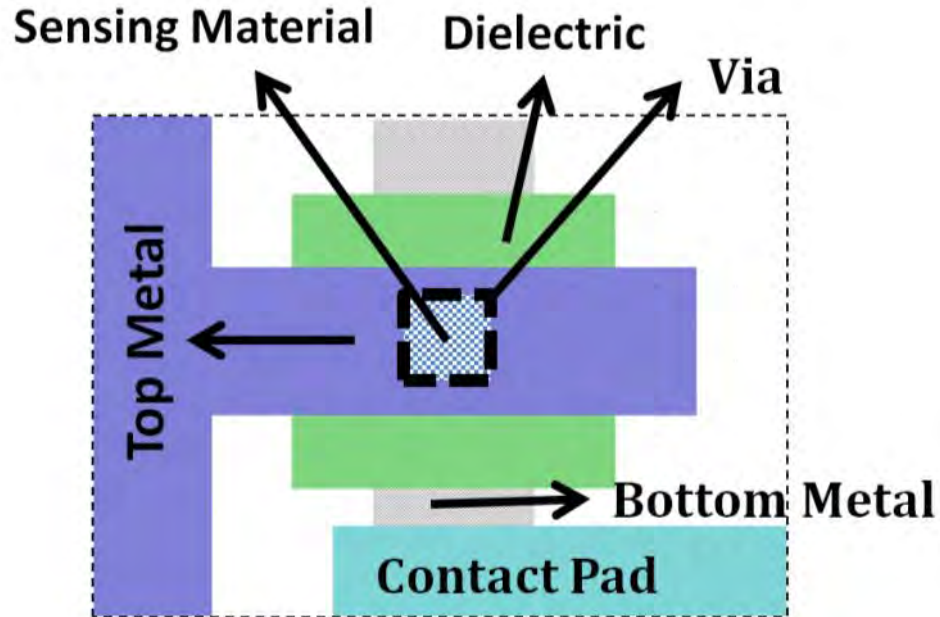


Figure 5-5. Top view of a mask set showing the different layers used for fabricating the out of plane resistance structure.

The processing of through-film structures was performed by using a mask set as shown in Figure 5-5. The processing was done following the process flow diagram of Figure 5-4 as follows: Bottom

contacts were deposited onto insulating substrates by a liftoff method. 100 nm of chromium was used for bottom contacts to Ge:H, whereas bottom contacts to high TCR VO_x thin films were obtained using either 100 nm of Titanium or Vanadium. Following the patterning of bottom contacts, 100 nm of SiO₂ was sputtered using magnetron sputtering of a 3-inch silicon target (99.999% pure) with 20% of O₂ flow in argon. A bias of –120 Volts was applied to improve the leakage current density through the sputtered SiO₂. Following this step, vias were etched using (6:1) BOE solution down to the bottom metal. High TCR VO_x deposited using Biased Target Ion Beam Sputtering (BTIBD) while Ge:H was deposited using Plasma Enhanced Chemical Vapor Deposition (PECVD) whose deposition will be described in the following subsection.

5.3.2. Deposition of High TCR, High Resistivity VO_x Thin Films

Previously, it has been shown that high TCR VO_x thin films can be deposited using a novel deposition technique of Biased Target Ion Beam Deposition (BTIBD) that incorporates precise control of the oxygen content of the thin film using a residual gas analyzer (RGA). The details of this deposition technique have been discussed in a previous chapter. Detailed values for the parameters used can be found in Table 2.

Briefly, a three-target configuration was used to deposit the thin films. A series of films was made with increasing partial pressure of oxygen, pO₂, ranging from 1×10^{-6} to 3×10^{-6} Torr, corresponding to an oxygen flow of 3 sccm–5 sccm. Total flow was kept at 70sccm, corresponding to a deposition pressure of $\approx 5.8 \times 10^{-4}$ Torr. A pulsed waveform was used to increase the sputter yield of the target in the oxidized regime. The target voltage was pulsed between –800V and +5 V to help minimize arcing during reactive sputtering. The voltage was pulsed at 10 KHz with a pulse width of 1 μ sec. Thin films were deposited to a thickness of ≈ 100 nm (at a deposition rate of 0.17 Å/sec) and were found to be highly uniform in thickness and its electrical properties (better than $\pm 3\%$).

5.3.3. Deposition of High TCR, High Resistivity Ge:H Thin Films

Thin films of Ge:H having thicknesses of 25 nm to 100 nm were deposited by RF ($f = 13.56$ MHz) plasma enhanced chemical vapor deposition (PECVD) using ultra-high purity germane (GeH_4) gas diluted with H_2 . The deposition conditions were similar to the experiment described in Section 3.2. A number of deposition parameters were fixed along the lines of previous work including: a total pressure of ~ 0.7 Torr and a low plasma power density of 0.08 W/cm^2 . The substrate was held at a temperature of 170°C and the hydrogen-to-reactive gas dilution ratio was maintained at $R = [\text{H}_2]/[\text{GeH}_4] = [160 \text{ sccm}]/[0.4 \text{ sccm}] = 400$.

5.3.4. Electrical Characterization of Device Performance

The three most important electrical properties for thin film microbolometer materials are: room temperature resistivity, temperature coefficient of resistivity (TCR) and the electrical noise given by the normalized Hooge parameter (α_H/n). The lateral resistivity of the thin films was extracted using the Transmission Length Method (TLM) patterns. Figure 5-6 shows a graph of resistance versus spacing of electrodes for a thin film of VO_x deposited using the BTIBD system at a partial pressure $p\text{O}_2$ of 3×10^{-6} Torr. The other deposition conditions are described in section 5.3.2. The contact resistance is given by the y-intercept (here $2 \times 10^7 \Omega$), the transfer length is given by half the value of the x-intercept (here $2 \mu\text{m}$) and the resistivity is given by multiplying the slope of the graph with the cross-sectional area of the thin film (here $\rho = 21,000 \Omega\text{-cm}$). The transfer length is used to decide on the minimum feature size which can be used to extract accurate thin film properties.

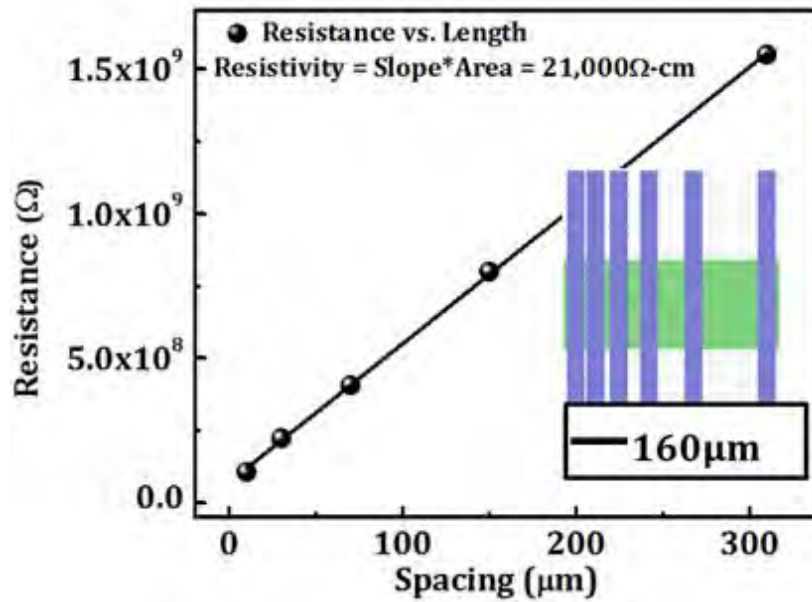


Figure 5-6. Resistance vs. electrode spacing measurements used to extract the sensing material's resistivity and the contact resistance.

Since the thickness of thin film is constant, the resistivity of the through film structures could not be measured using the TLM method. Instead, the effective through film resistivity was determined by patterning through film structures having different areas as can be seen in Figure 5-7.

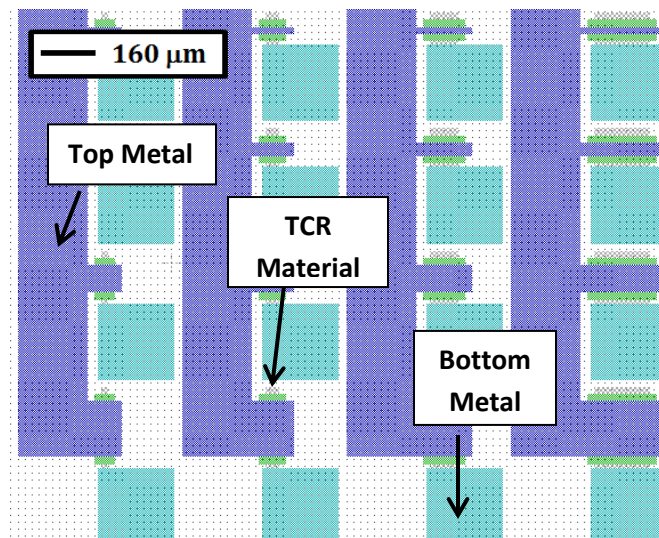


Figure 5-7. Top view of the mask set used for the measurement of resistivity of the sensing material.

I-V measurements were made on each through film resistor VO_x thin film and is evaluated in Figure 5-6. The resulting resistance values are plotted as a function of '1/contact area' and are shown in

Figure 5-8. The slope of the graph can be used to obtain the ‘effective resistivity’ of the thin film such that:

$$\rho = \frac{1}{\text{thickness}} \times \frac{R_B}{1/\text{Area}} = \frac{\text{Slope}}{\text{Thickness}} \quad \text{Equation 33}$$

Similarly, the contact resistance can be calculated using the x–intercept of the curve. The x–intercept gives a point in which the area of the device interrogated is infinitely large. Such a point would contain only the contact resistance and have a relatively insignificant contribution from the thin film itself.

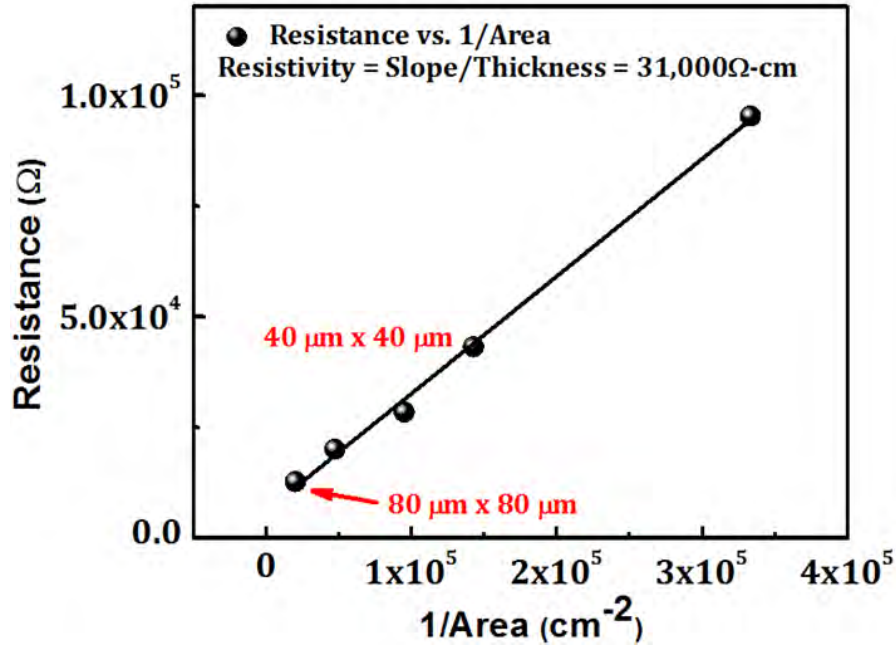


Figure 5-8. A plot of resistance vs. 1/Area used to extract the resistivity of the sensing material as measured from the structures in Figure 5-7. By dividing the slope of the line and the thickness of the film, the material’s resistivity can be extracted.

The TCR measurements were made using a heated stage and a computer controlled HP4140B pA /DC voltage source. The TCR value was extracted from the activation energy after measuring the temperature dependence of resistance at incremental temperatures between 20-60°C using the relation given by:

$$TCR = - \frac{E_a}{k_b T^2} \quad \text{Equation 34}$$

where E_a is the activation energy of the thin film material, k_b is the Boltzmann's constant and T is the temperature at which the TCR value is to be calculated.

The 1/f noise of the material is evaluated by the Hooge-Vandamme relation given by:

$$\text{Log} \left(\frac{S_I(f)}{I_{bias}^2} \right) = \text{Log} \left(\frac{\alpha_n}{n \times V} \right) - \beta \text{Log}(f) \quad \text{Equation 35}$$

where, $S_I(f)$ is the spectral current density, I_{bias} is the sample current, V is the volume of the sample, f is the frequency of measurement, α_n is the Hooge's parameter, β is the slope of 1/f noise measurement and n is the carrier concentration in the samples. To evaluate the properties of the films, ' α_H/n ' was treated as the property of interest as described previously. The instrumentation for this measurement has also been described in a previous chapter.

5.4. Experimental Results

Since in the through film configuration, the thickness of the thin film is used as the length of the resistor, small electrical biases can result in large electric fields across the thin film. These large electric fields can result in nonlinear I–V characteristics of the through film resistors. The result of which can be seen in Figure 5-9.

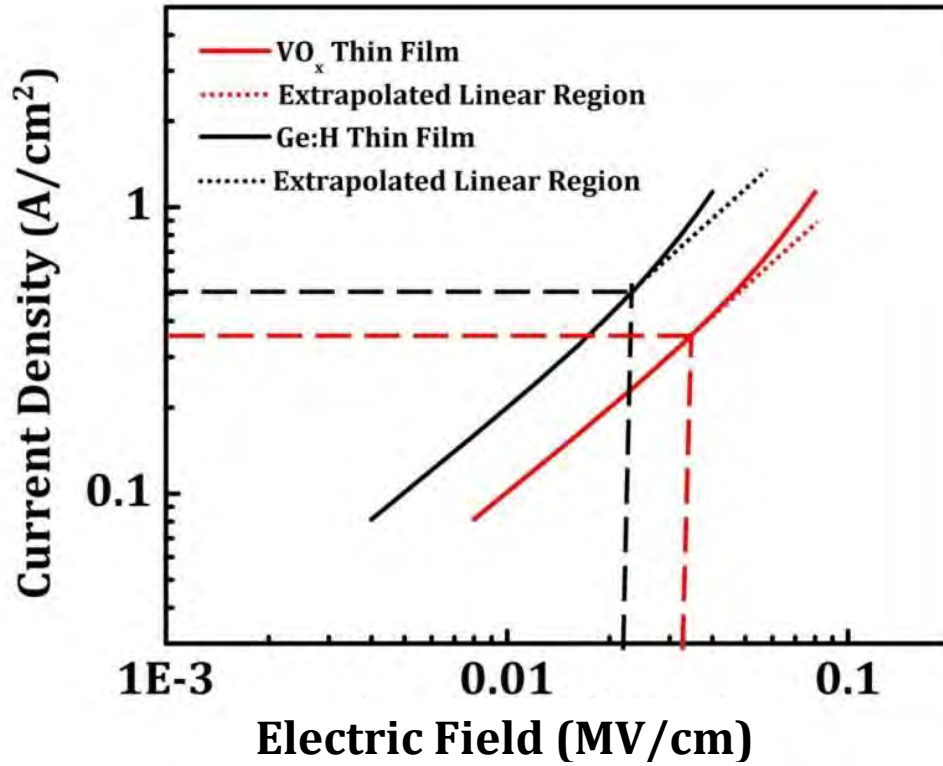


Figure 5-9. Current density as a function of electric field applied across the thin film resistor.

To ensure accurate measurements, the through film sensors were biased in the linear region of Figure 5-9. Figure 5-10 shows the lateral and through film resistivities of thin films of Ge:H deposited in this work. The lateral resistors of Ge:H have been investigated in Chapter 4. The lateral resistivity depends on the thickness of the thin film investigated. The through film resistivity varies significantly from its lateral resistivity: from 1,000 $\Omega\text{-cm}$ for the 200 nm (750 $\Omega\text{-cm}$ for the lateral configuration) to 28.6 $M\Omega\text{-cm}$ for the 25 nm thin film (1,250 $\Omega\text{-cm}$ for the lateral configuration). The disparity in the resistivity between the lateral and the through film configuration suggests that there exists an insulating layer at the interface of the bottom metal and the resistive thin film, or the initial layers of the resistive thin film have an extremely high resistivity.

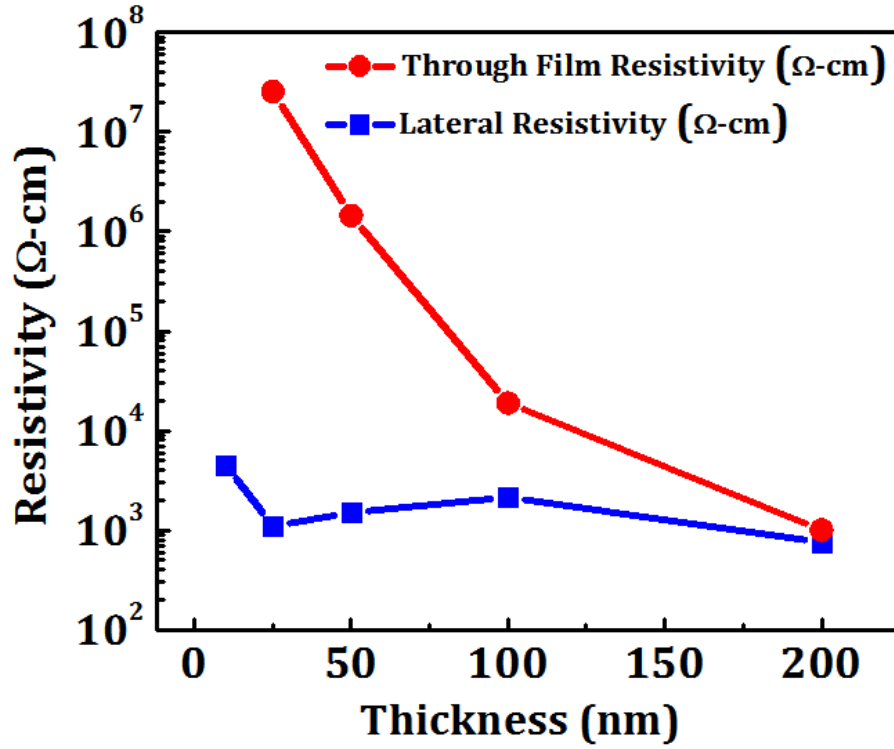


Figure 5-10. Lateral and through film resistivity of thin films of Ge:H thin films as a function of thickness. The through film resistivity increases dramatically for smaller thicknesses, indicating an insulating interfacial layer between the bottom metal and the resistive thin film.

Figure 5-11 shows a plot of natural log of resistance versus temperature of thin films of VO_x and Ge:H in the lateral and through-film configurations. For the through film measurements, the resistors were biased by using small electric fields such that the 'I-V' data collected were linear. It was found that though the lateral and through film resistance values are orders of magnitude different, the TCR values remained the same. These results are a strong proof of concept for the proposed through film resistor design.

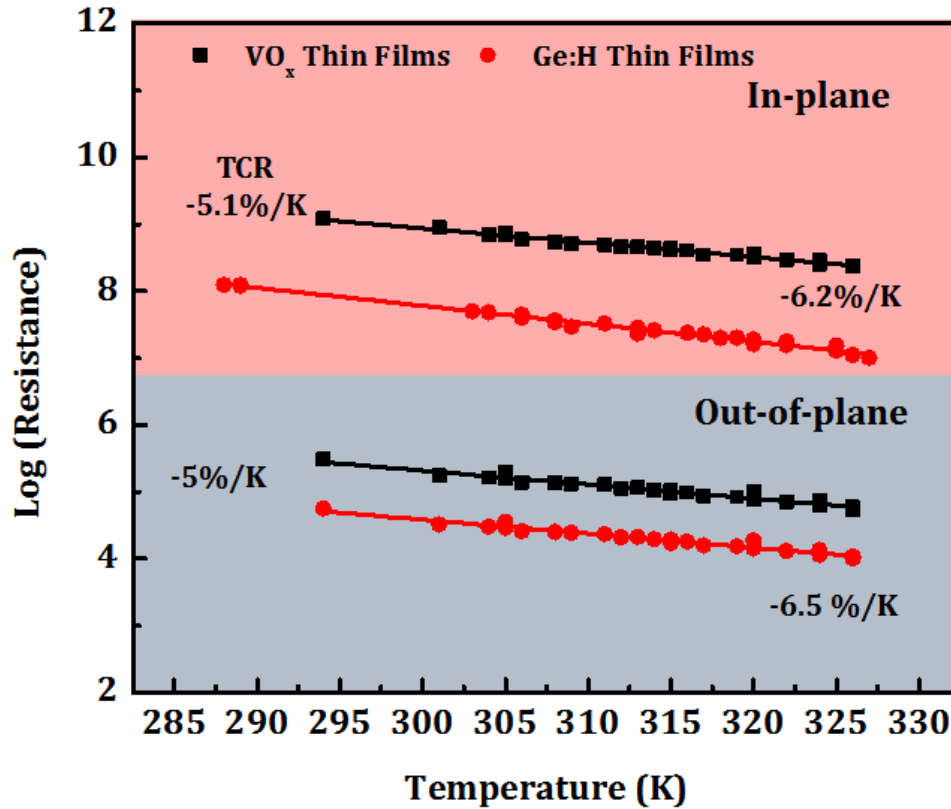


Figure 5-11. Resistance vs. temperature plots for thin films of VO_x and Ge:H fabricated in lateral and through film configuration showing orders of magnitude difference in resistance but similar TCR.

Having measured the resistance and the TCR values of the through film resistors, the $1/f$ noise of the thin films was evaluated using methods described in Chapter 3. Figure 5-12 shows the acquired Power Spectral Density of thin films of Ge:H, 50-nm-thick with different volumes of the thin film resistors in both lateral and through film configurations. As expected, the $1/f$ noise increases with decreasing device volume. When normalized for volumes, the magnitude of the $1/f$ noise was found to be the same as can be seen from the inset of Figure 5-12.

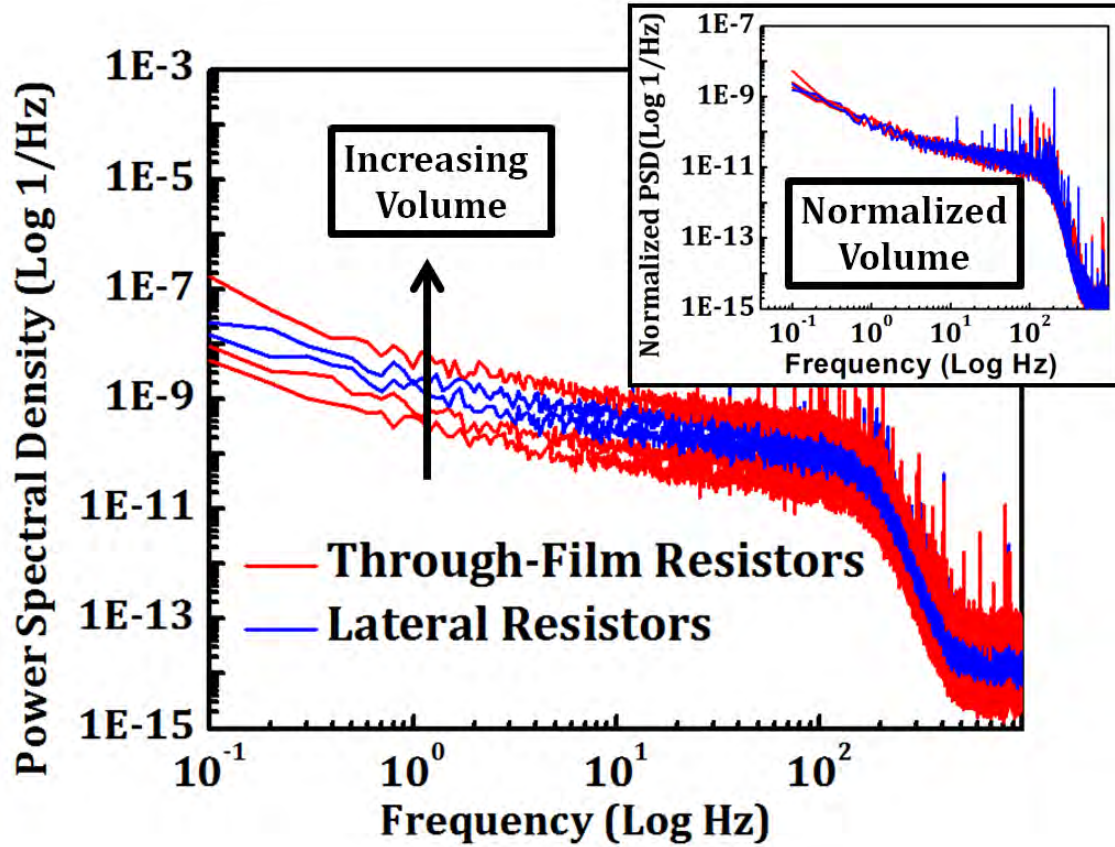


Figure 5-12. The measured Power Spectral Density (PSD), S_i^2/I_{bias}^2 for a 50 nm thin film of Ge:H showing good agreement with the Hooke's relationship, independent of device structure used (lateral or through film). Inset shows the PSD normalized for volume.

Table 4 compares the TCR and ' α_H/n ' of thin films in lateral and through film configuration deposited in this work. Within the margin of error of measurement, the TCR and the ' α_H/n ' of thin films was found to be the same.

Table 4. Summary of TCR and ' α_H/n ' values in lateral and through film configuration deposited in this work.

Sample	TCR Lateral (%/K)	TCR Through Film (%/K)	' α_H/n ' Lateral (cm ³)	' α_H/n ' Through Film (cm ³)
VO _x	-4.1	-4	1.4×10^{-19}	1×10^{-19}
VO _x	-4.5	-4.6	1.5×10^{-18}	1×10^{-18}
VO _x	-4.7	-5	4×10^{-18}	1×10^{-18}
VO _x	-5	-5.3	3×10^{-18}	1×10^{-18}
Ge:H	-3.4	-3.6	7×10^{-19}	5×10^{-19}
Ge:H	-5	-5.1	1.7×10^{-19}	1×10^{-19}
Ge:H	-6.2	-6.5	8×10^{-20}	1.2×10^{-20}

Similar values of TCR and α_H/n shows that in going from the lateral device configuration to a through film configuration there is no change in the signal to noise ratio (SNR). However, as it was noted in section 5.2, the vertically integrated devices can sustain larger signal currents due to their lower device resistance without any change in self heating. This means that although the SNR has not changed with device configuration, the magnitude of the signal is larger. As was seen in Section 2.3.4.2, a higher signal current implies reduced integration time on the readout capacitor, thereby increasing the available frame rate of the sensing array.

5.5. Conclusion

Vertically integrated VO_x thin films structures have been demonstrated as potentially viable alternative to the conventional lateral-pixel configuration used in uncooled imaging bolometers, for next generation IR FPAs that employ higher TCR and higher resistivity material. In this work, high VO_x thin films were obtained using BTIBD and high TCR Ge:H thin films were obtained by PECVD of GeH_4 at high dilution ratios.

Using lithographically patterned structures it has been shown that through film conductivity measurements make it possible to reduce the device resistance of high TCR materials. The SNR for the through film structures equal to those obtained using lateral conductivity.

Chapter 6. Resistive Temperature Sensing Arrays

6.1. Introduction

Microbolometer arrays have been at the forefront non-contact thermometry. These devices have high sensitivity ($\text{NETD} < 30 \text{ mK}$) and high frame rates ($> 30 \text{ Hz}$) [15] [18]. However, these systems are based on the principle of differential temperature and are not designed for use in the contact mode or for mapping the absolute temperature of the object under investigation. In addition, these sensors are based on materials with $|\text{TCR}| < 4 \text{ \%}/\text{K}$ in the lateral configurations where the device impedance is relatively high ($> 100 \text{ M}\Omega$). In this work, thin films of VO_x with $\text{TCR} \approx 4.4 \text{ \%}/\text{K}$ were used to fabricate one dimensional arrays of vertically integrated temperature sensors on glass substrates. The performance of these arrays is compared with those of the lateral resistors. In addition, discrete devices are fabricated with integrated ZnO based transistors to allow multiplexing of two dimensional arrays.

6.2. Array Design and Fabrication

6.2.1. Design and Processing of 1-D VO_x Sensor Array

Figure 6-2 shows the schematic of the 1×8 1-D temperature sensing array fabricated in this work. The total length of the sensor was kept at 2 cm, while the head of the sensor was fabricated to be $500 \text{ }\mu\text{m}$ wide. The narrow width of the top of the sensor was designed to reduce the thermal mass, and facilitate implant for in-vivo testing. The base of the sensor was kept wide to facilitate bonding to the pads. The bonding pads had a width of $250 \text{ }\mu\text{m}$ with a pitch of $500 \text{ }\mu\text{m}$.

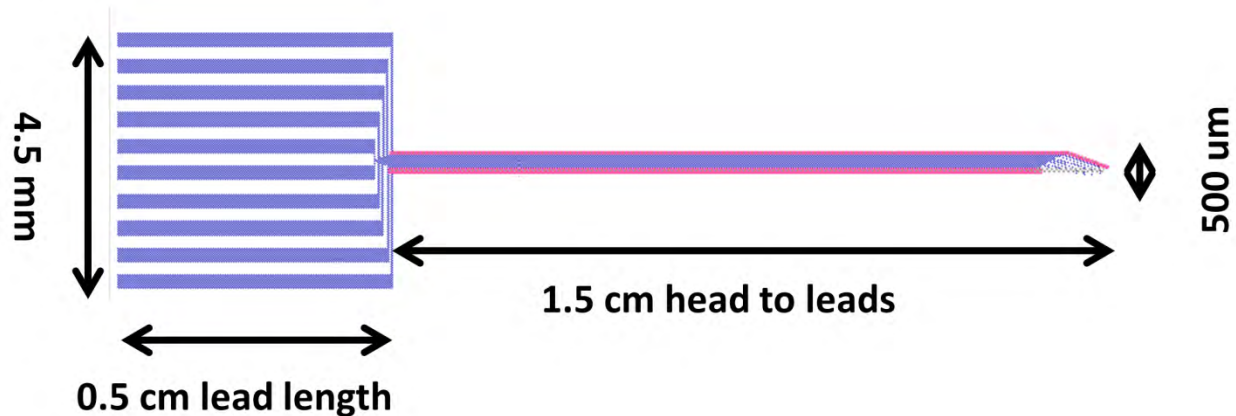


Figure 6-1. Schematic showing the 1x8 temperature sensing array fabricated in this work. The top of the sensor is kept narrow while the leads are spread out to facilitate wire bonding.

Figure 6-2 shows a close up view of the top of the sensor array. Although the array shown in this figure consists of vertically integrated thin films of VO_x , lateral configurations were also investigated in this work. Vertically integrated resistors had dimensions of $10\text{ }\mu\text{m} \times 10\text{ }\mu\text{m}$, while the lateral configuration had a W/L ratio of $10\text{ }\mu\text{m}/50\text{ }\mu\text{m}$, both with a film thickness of 85 nm. To avoid catastrophic failure of the vertically integrated sensors due to electrostatic discharge during handling, all leads were connected using a shunt. Once the array was ready for measurement, the shunt connection could be cut by using micromanipulators on a probe station.

To improve the sensitivity of the fabricated array, glass substrates ($\approx 2\text{ mm}$ thick) were used due to their low thermal conductivity and therefore a lower ability to transport heat away from the sensors. The fabrication of the vertically integrated resistor array was done using a procedure described in section 5.3 and Figure 5-4, while the lateral configuration resistors were fabricated using the procedure detailed in Figure 3-18. The thin films of VO_x were deposited using the BTIBD system using a three target configuration. The deposition parameters can be found in Table 5. The obtained resistivity of the thin films was $\approx 12,000\text{ }\Omega\text{-cm}$.

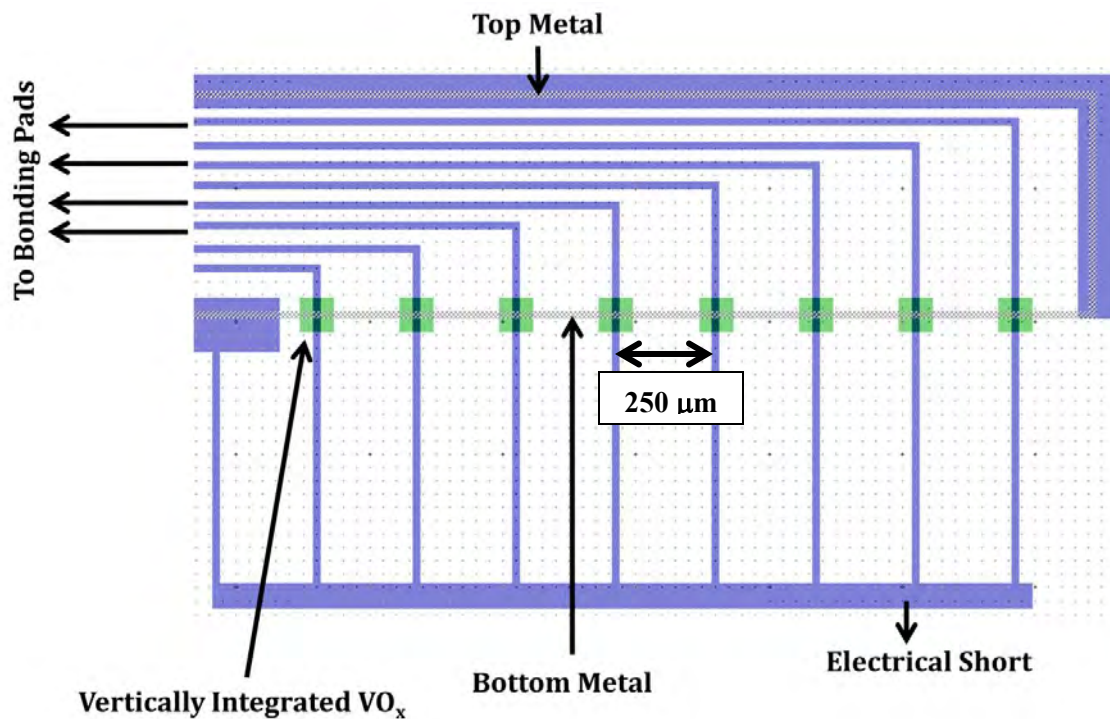


Figure 6-2. Schematic of the top of the 1×8 vertically integrated VO_x sensor array fabricated in this work. All through film sensors were electrically shorted during fabrication, dicing and wire bonding. Prior to measurement they were cut using a micromanipulator.

Table 5. Typical parameters used for the deposition of VO_x thin films for this chapter

Deposition Conditions	Value
Base Pressure	$< 1 \times 10^{-7}$ Torr
Targets	3, Vanadium (99.99% pure)
Total pressure	5.8×10^{-4} Torr
O ₂ Partial pressure	3×10^{-6} Torr (4–5 sccm)
H ₂ O partial pressure	$< 2 \times 10^{-7}$ Torr
Voltage pulse	99 μsec/1 μsec (–800V/+5 V) = 100 μsec
Target current	285 mA
HC parameters	10 sccm Ar flow, 1.5 A, 20 V
Ion source parameters	60 sccm Ar flow, 7.5 A, 38 V
Pre-sputter time	10 minutes
Stage spin	20 rpm
Time	30 minutes (85 nm thick)

An equivalent circuit diagram of a second design consisting of a ZnO based transistor/switch is shown in Figure 6-3. The VO_x sensor/resistor is placed on the drain of the transistor. The current (and therefore impedance) is read between the drain and the source terminals when the transistor is turned on

and a bias is applied using a voltage source. Devices were fabricated using both the vertically integrated and the lateral resistance structures.

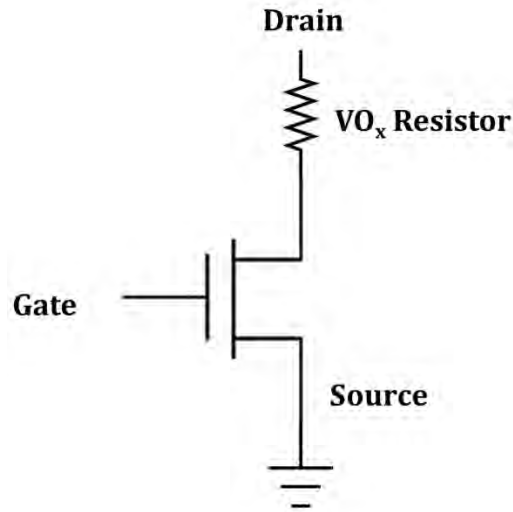


Figure 6-3. Equivalent circuit diagram showing VO_x resistors integrated with ZnO transistors as fabricated in this work.

To reduce the resistance of the lateral VO_x structures, interdigitated electrodes were fabricated as can be seen in Figure 6-4. The resistor's W/L ratio was designed to be $160\text{ }\mu\text{m}/5\text{ }\mu\text{m}$. For high TCR VO_x thin films (85 nm thick) having resistivity of $\approx 10,000\text{ }\Omega\text{-cm}$, this implied a resistance value of $\approx 35\text{ M}\Omega$ for the lateral devices and $\approx 1.5\text{ M}\Omega$ for the vertically integrated devices Figure 6-5. The W/L ratio of the transistor was chosen so that the TFT's contribution to the total impedance is minimal. This ratio is especially critical for the vertically integrated transistors where the resistance of the VO_x structure is of the order of $1\text{ M}\Omega$. For these TFTs, interdigitated source drain contacts were deposited having a W/L ratio of $470\text{ }\mu\text{m}/5\text{ }\mu\text{m}$ for TFT on resistance of $\approx 1,500\text{ }\Omega$.

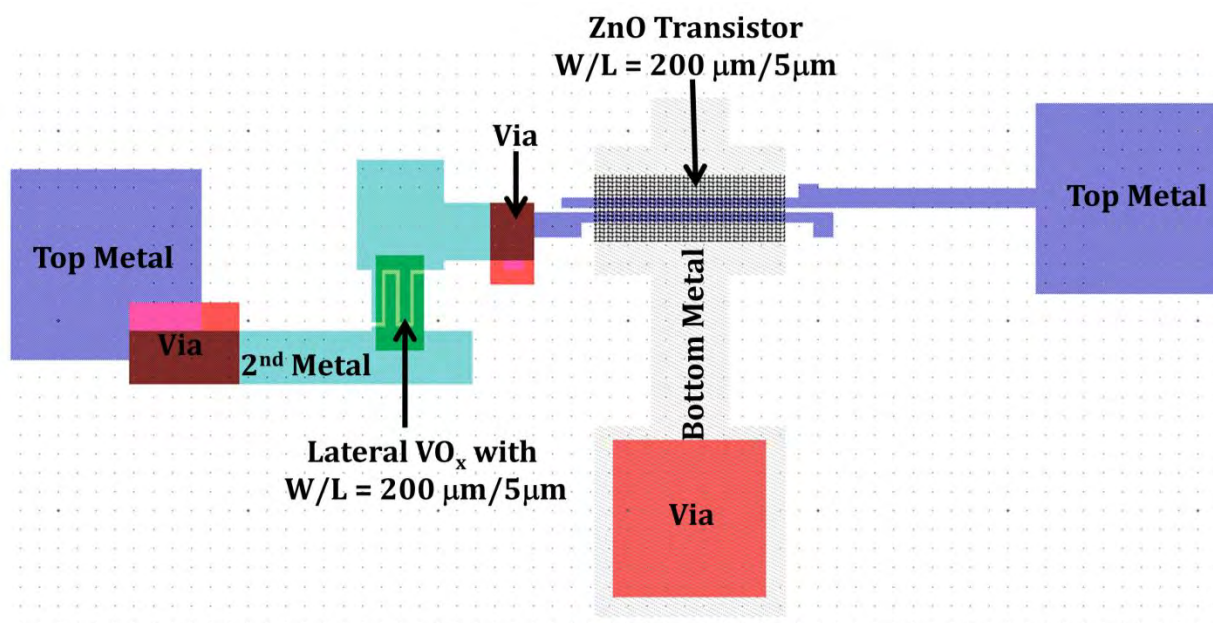


Figure 6-4. Schematic of lateral VO_x sensors integrated with ZnO based transistors. To allow for low impedance, the width to length ratio of $200\ \mu\text{m}/5\ \mu\text{m}$ was designed for both the VO_x resistors ($100\ \text{M}\Omega$) and the ZnO transistors ($4,000\ \Omega$).

Processing of these TFT integrated VO_x thin films was done using a 6 layer mask set as follows. Bottom gate metal (100 nm of Ti) was patterned by using sputter deposition and liftoff techniques. The thin film of VO_x was deposited using parameters shown in Table 5. Following this the VO_x thin films were patterned and etched using double layer lithography in a 1:2,000 solution of H_2O_2 and H_2O . A second layer of Ti metal was sputter deposited onto the VO_x thin films to serve as electrodes for the thin film.

The gate oxide and ZnO layers were deposited using plasma enhanced atomic layer deposition (PEALD) with help from Yiyang Gong from the department of Electrical Engineering. A 32 nm of Al_2O_3 was deposited from trimethylaluminum (TMA) and CO_2 , and a 10 nm ZnO film was deposited from diethylzinc and N_2O , both at $200\ ^\circ\text{C}$. After the PEALD step the ZnO was patterned by wet etching in diluted HCl (1:4000), and vias were etched in the Al_2O_3 down to the bottom metal and the second metal contacts, by wet etching in hot ($80\ ^\circ\text{C}$) phosphoric acid. Finally the source drain contacts were sputter deposited and patterned by liftoff.

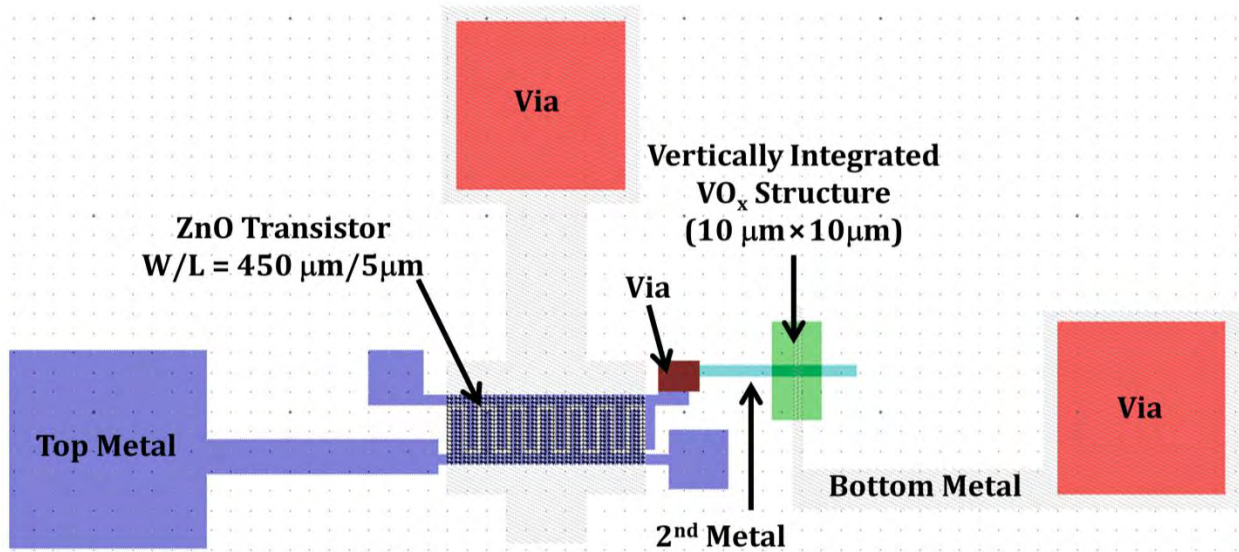


Figure 6-5. Schematic of vertically integrated VO_x sensors with ZnO based transistors. The through film resistors had dimensions of $10\ \mu\text{m} \times 10\ \mu\text{m} \times 100\ \text{nm}$ ($1.3\ \text{M}\Omega$), while the ZnO transistors were fabricated with a width to length ratio of $450\ \mu\text{m}/5\ \mu\text{m}$ ($1,500\ \Omega$).

Figure 6-5 shows the schematic of vertically integrated VO_x resistors. For these structures, the bottom metal used as the gate metal for the ZnO TFT, was used as the bottom electrode for VO_x thin films.

6.2.2. One Dimensional Testing Setup

One dimensional arrays were fabricated using both lateral and through film configurations using high TCR VO_x thin films. Figure 6-6 shows the equivalent circuit diagram of the design used for the fabrication of the array. Resistors R_1 through R_8 are resistors of VO_x thin films which could be fabricated using either lateral or vertically integrated configurations. Switches S_1 through S_8 are relays of the Keithley 7075 general purpose multiplex card which can be used to select the resistor to be interrogated. Each switch of the Keithley 7075 general purpose multiplex card is connected to an HP 414B DC source/monitor unit (SMU) which sources voltage and measures current through each resistor. Since 4 SMUs are available on an HP 4141B, up to four resistors could be read simultaneously to achieve a higher array refresh rate. The 1-D array was measured by bonding the array to a PC Board using anisotropic conductive film (ACF) bonding. Leads from the board were connected to individual relays of

the Keithley 7075 multiplex card. Figure 6-7 shows an array bonded to a PC Board and the setup used for measurement of the 1-D array.

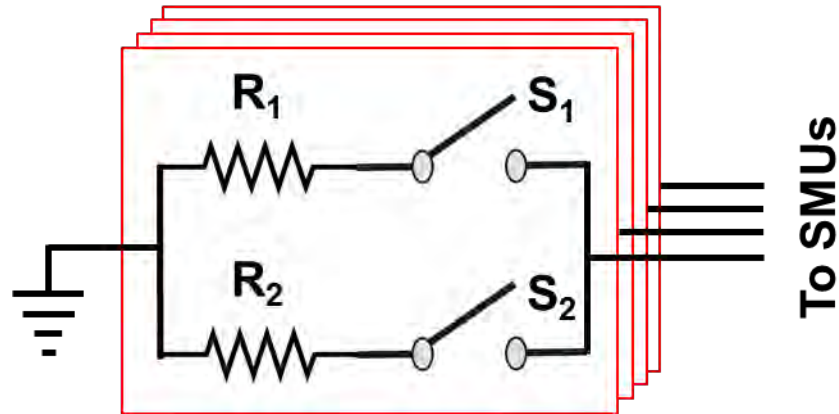


Figure 6-6. Equivalent circuit diagram of the 1x8 array fabricated in this work. The resistors can be lateral or vertically integrated, a Keithley 7075 general purpose multiplex card is used as the switch matrix while an HP4141B DC SMU is used for measuring the output current.

For temperature stabilization, the entire array was placed on a VWR heater block which had a temperature stability of ± 0.1 °C and a surface temperature variability of ± 0.1 °C. The entire setup was insulated from the environment using a foam construction as seen in Figure 6-7.

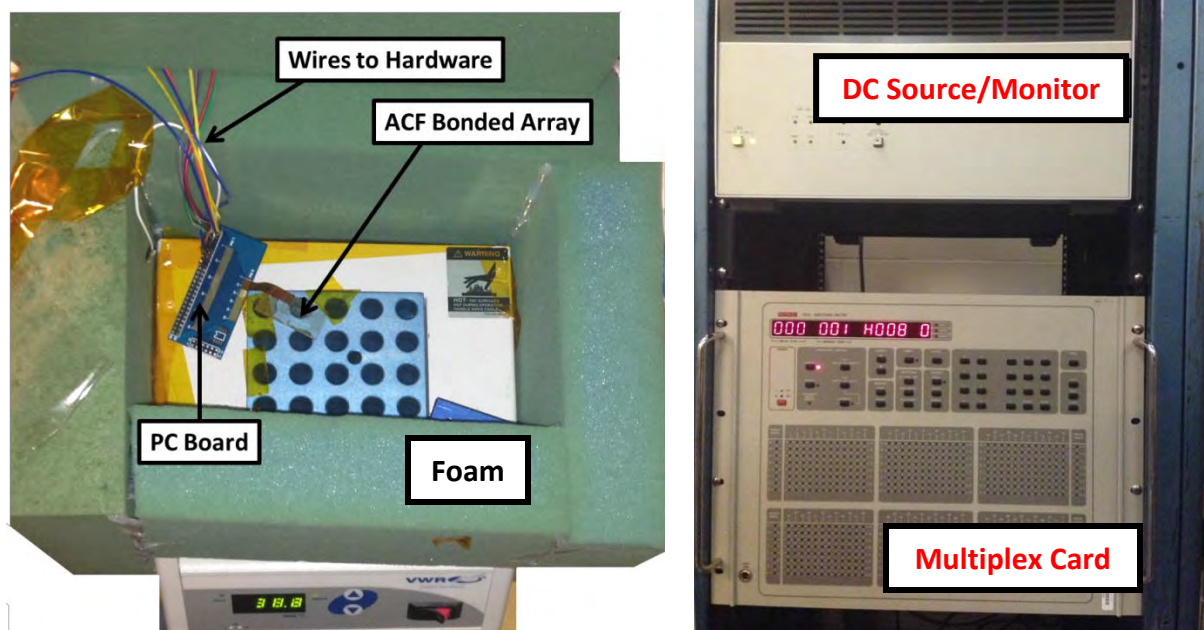


Figure 6-7. Test setup for the measurement of the 1-D arrays. ACF bonded samples on a VWR heater block (left) and the sensor biasing hardware including the HP4141B DC SMU and the Keithley 707A mainframe consisting of the Keithley 7075 general purpose multiplex card (right).

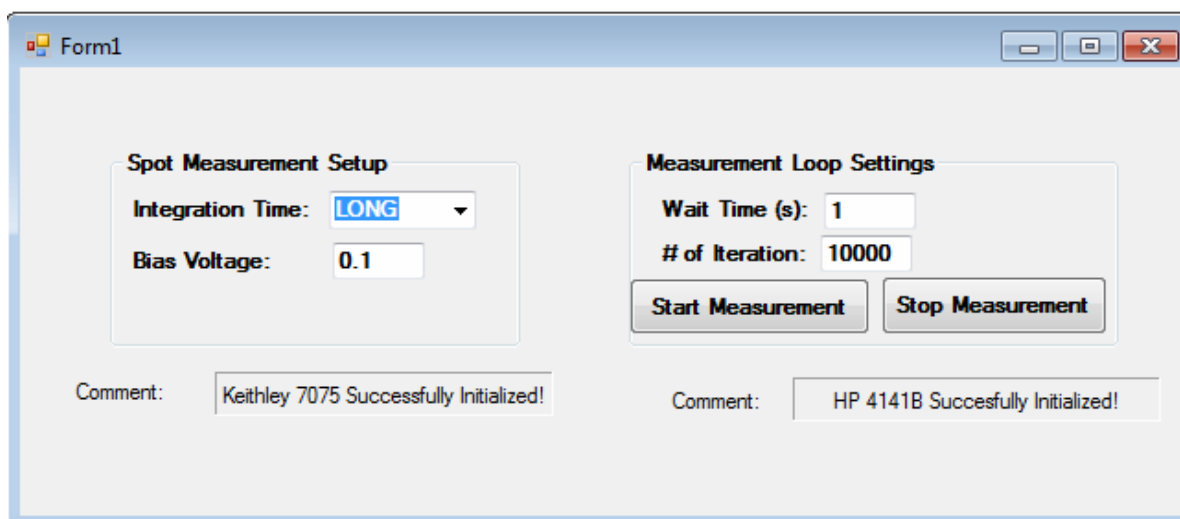


Figure 6-8. Screenshot of the C++ based program written to readout the 1D array by remote operation of the HP4141B DC SMU and the Keithley 7075 general purpose multiplex card. The program sets parameters for the array voltage bias, current measurement, the number of spot measurements to be performed and the wait time between each measurement.

The testing of the array was performed using a C++ program (screenshot in Figure 6-8) which provided computerized control and automation of the measurement. Appropriate bias, the integration time

for the HP 4141B DC SMU as well as the number of iterations the array needed to be measured can be remotely selected. The program triggered a spot measurement of the HP4141B after the selected bias was applied. Since two sensors are needed to be measured by one SMU, each device was left unbiased while the other device was being measured. Using a long integration time, the array had a refresh time of 3.5 seconds.

6.3. Results and Discussion

The 1-D array consisting of lateral VO_x resistors was biased using a voltage of 1 V. The output current for all the 1×8 sensors was recorded over a 24 hour time period at a temperature of 35 °C. The current of one of the sensors is shown in Figure 6-9. The output current has an RMS noise of ≈ 160 mK and is found to drift by ≈ 0.25 °C over the 24 hour time period. In addition, the output current shows periodic oscillations with a frequency of 4×10^{-4} Hz.

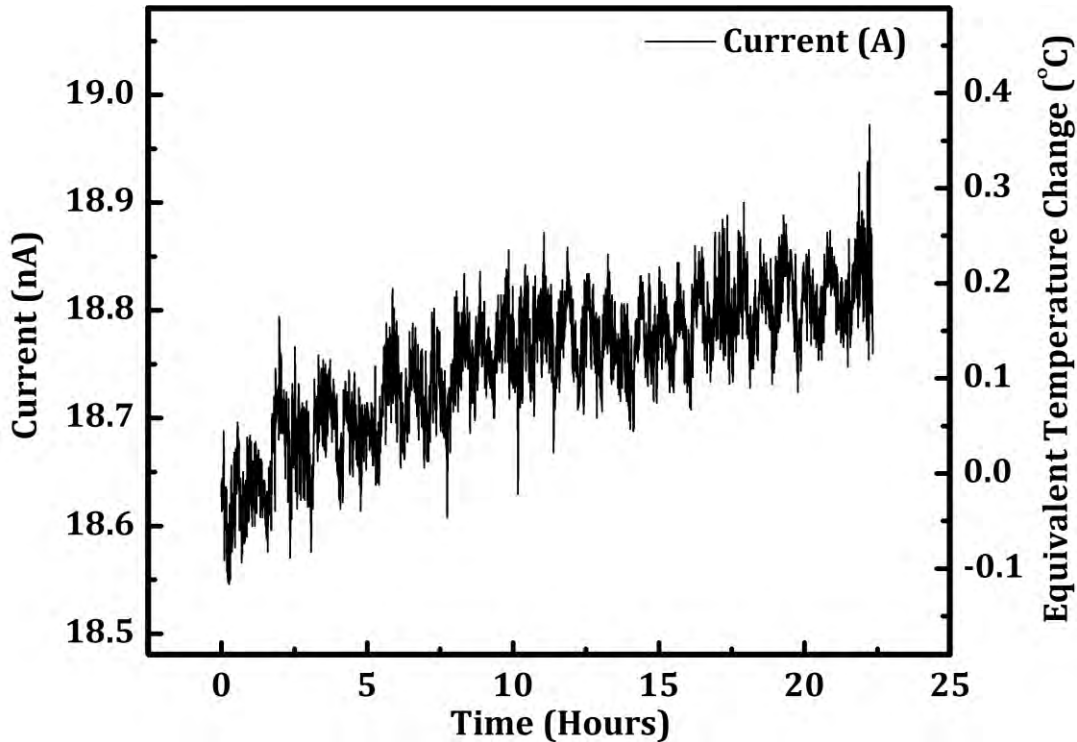


Figure 6-9. Current output for a lateral VO_x sensor with a resistance of ≈ 50 M Ω at 35 °C measured over 24 hours. The periodicity arises from the attempts of the heater block to stabilize to a set point of 35 °C. The measured RMS noise was found to be 160 mK.

Figure 6-10 shows the output current from all 8 sensors of the lateral 1×8 sensor array. It can be seen that all sensors have similar values of resistance ($\approx 1\%$). All sensors have similar drift in the long term performance of $0.2\text{ }^{\circ}\text{C}$. The low frequency oscillations observed appears at the same time for all sensors. This implies that the observed periodic fluctuation in the output current at a frequency of $4 \times 10^{-4}\text{ Hz}$ is due to oscillations in the temperature of the heater block.

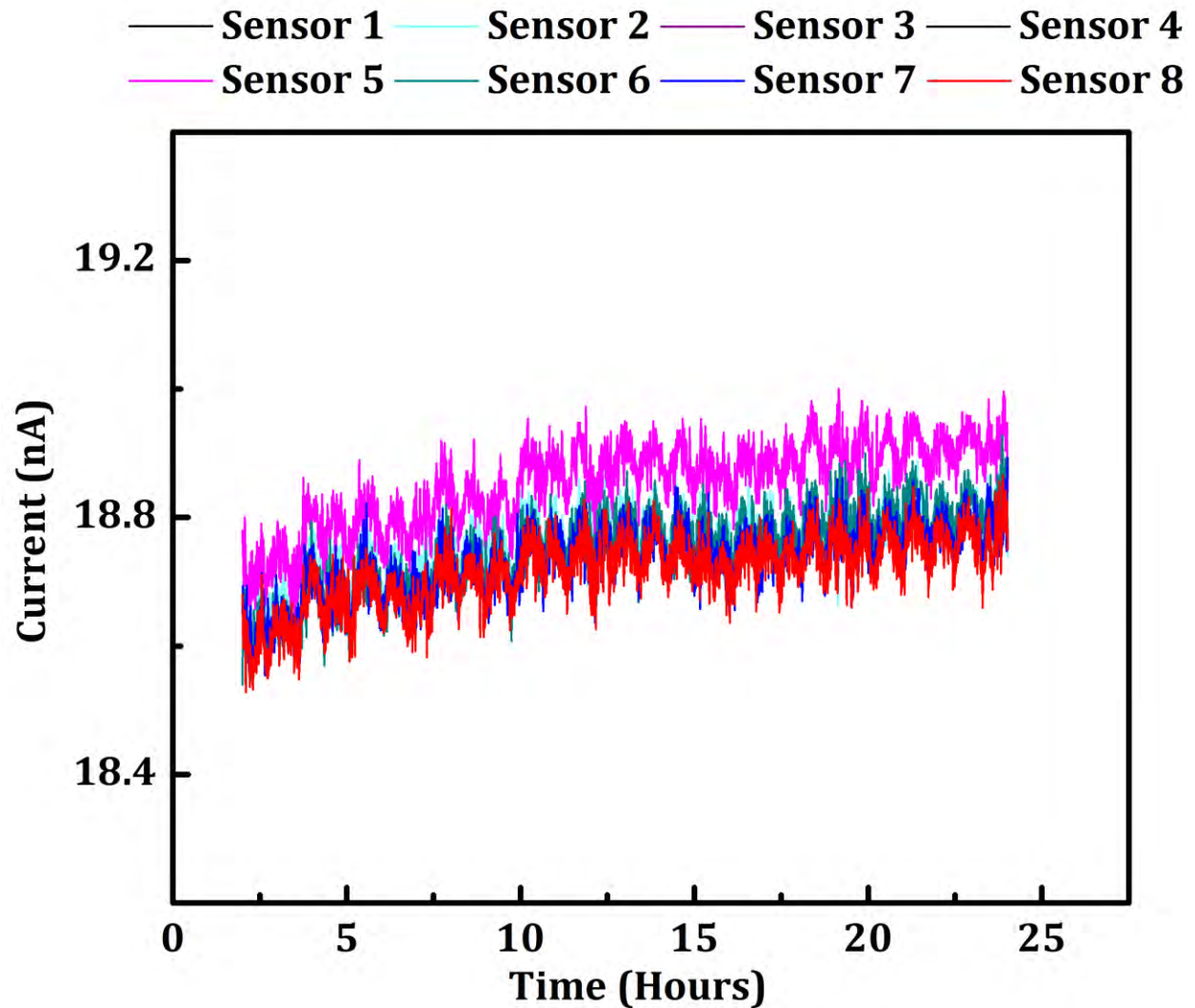


Figure 6-10. Current output of the 8 VO_x temperature sensor array measured at $35\text{ }^{\circ}\text{C}$ on a VWR heater block at bias voltage of 1 V for 24 hours.

The RMS noise observed in all 8 sensors is $\approx 160\text{ mK}$. Table 6 gives the parameters used as well as the calculated and observed signal to noise ratio (SNR) of thin film sensors using lateral resistance structures. The experimentally observed noise is ≈ 40 times higher than the theoretical calculations

estimated using Equation 30. The higher noise can be attributed to the cables used in the setup and leakage through the Keithley switch matrix card. When open circuit measurements were performed with the setup, current leakage of ± 40 pA was observed.

Table 6. Assumed parameters for SNR calculation

Parameter	Lateral	Vertically Integrated
Resistance	50 M Ω	1.5 M Ω
V_{bias}	1 V	0.1 V
N. Hooge's parameter (α_H/n)	10^{-18} cm^3	10^{-18} cm^3
f_2	714 Hz (1.4 ms measurement)	714 Hz (1.4 ms measurement)
f_1	1 Hz	1 Hz
Samples averaged (based on integration time)	256	256
TCR	-4.4 %/K	-4.4 %/K
T	308 K	308 K
Volume	$10 \mu\text{m} \times 50 \mu\text{m} \times 85 \text{ nm}$	$10 \mu\text{m} \times 10 \mu\text{m} \times 85 \text{ nm}$
Calculated SNR from Equation 30	10,000	7,200
Observed SNR	≈ 280	$\approx 1,500$

Figure 6-11 shows the current response of a vertically integrated sensor from a 1×8 temperature sensing array. These devices were biased with 0.1 V with other relevant measurement parameters as shown in Table 1. The observed SNR ratio was 1,500 compared with 280 for the lateral resistance structures as calculated from Equation 30. The recorded RMS noise for these sensors was ≈ 35 mK compared with 160 mK for the lateral devices. The periodic fluctuation in the temperature of the heater block can be seen much clearly for these vertically integrated sensors.

Figure 6-12 shows a plot of log resistance versus temperature for a lateral device. The TCR from the measurement was found to be -4.4 %/K which was similar to that of vertically integrated thin films.

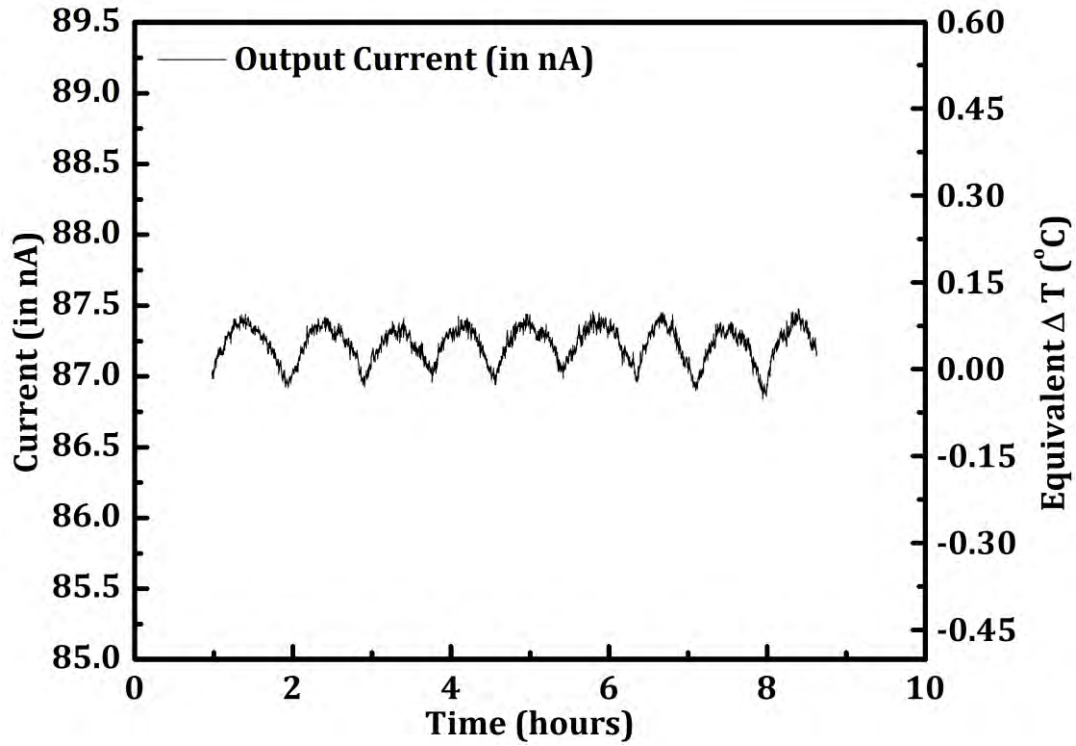


Figure 6-11. Output current of vertically integrated VO_x sensors $10\text{ }\mu\text{m} \times 10\text{ }\mu\text{m} \times 85\text{ nm}$ having a resistance of $1.3\text{ M}\Omega$ at a temperature of $35\text{ }^{\circ}\text{C}$. The resistor was biased with a voltage of 100 mV . The measured RMS noise was found to be $\approx 35\text{ mK}$.

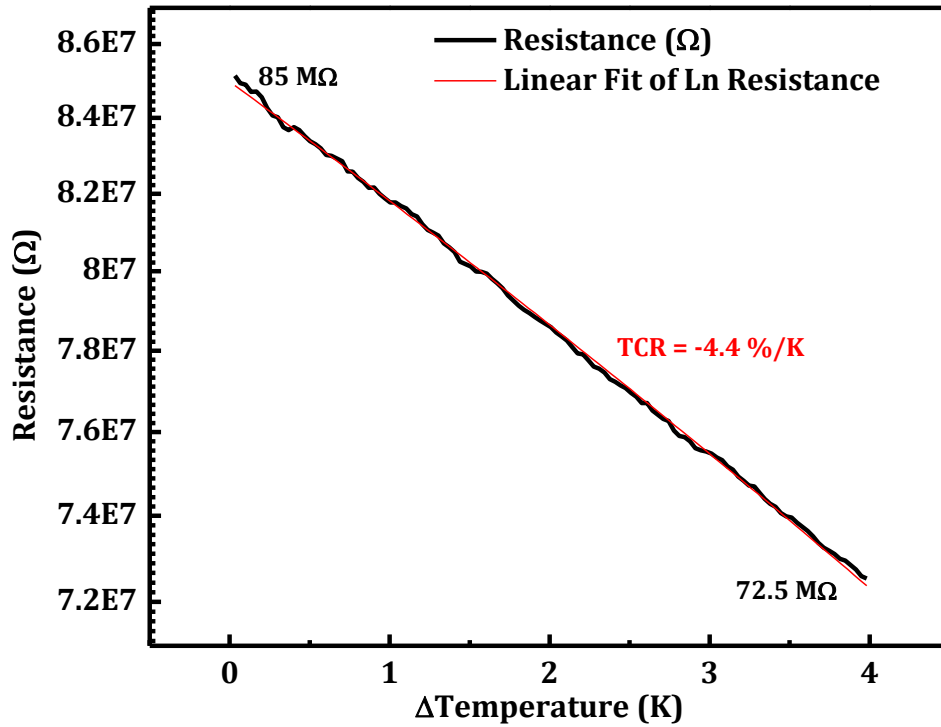


Figure 6-12. A plot of natural log of resistance as a function of temperature for lateral thin film resistors of VO_x having dimensions of $10\text{ }\mu\text{m} \times 50\text{ }\mu\text{m} \times 85\text{ nm}$. The TCR extracted using activation energy was found to be $-4.4\text{ \%}/\text{K}$.

Although there is a significant decrease in the electrical noise for the vertically integrated devices in comparison with the lateral devices (from 160 mK to 35 mK), the noise is significantly higher than the theoretical calculation of electrical noise of 8 mK. One such reason for the disparity in the electrical noise could be elevated levels of electrical noise due to the ribbon cables used in the test setup. Figure 6-13 shows the measured current noise of the measurement system over duration of 8 hours with the VO_x sensors disconnected. This open circuit measurement gives the lower limit of the current signal current which can be measured and hence sets a lower limit on the achievable sensitivity. This current noise was found to be of the order of 40 pA.

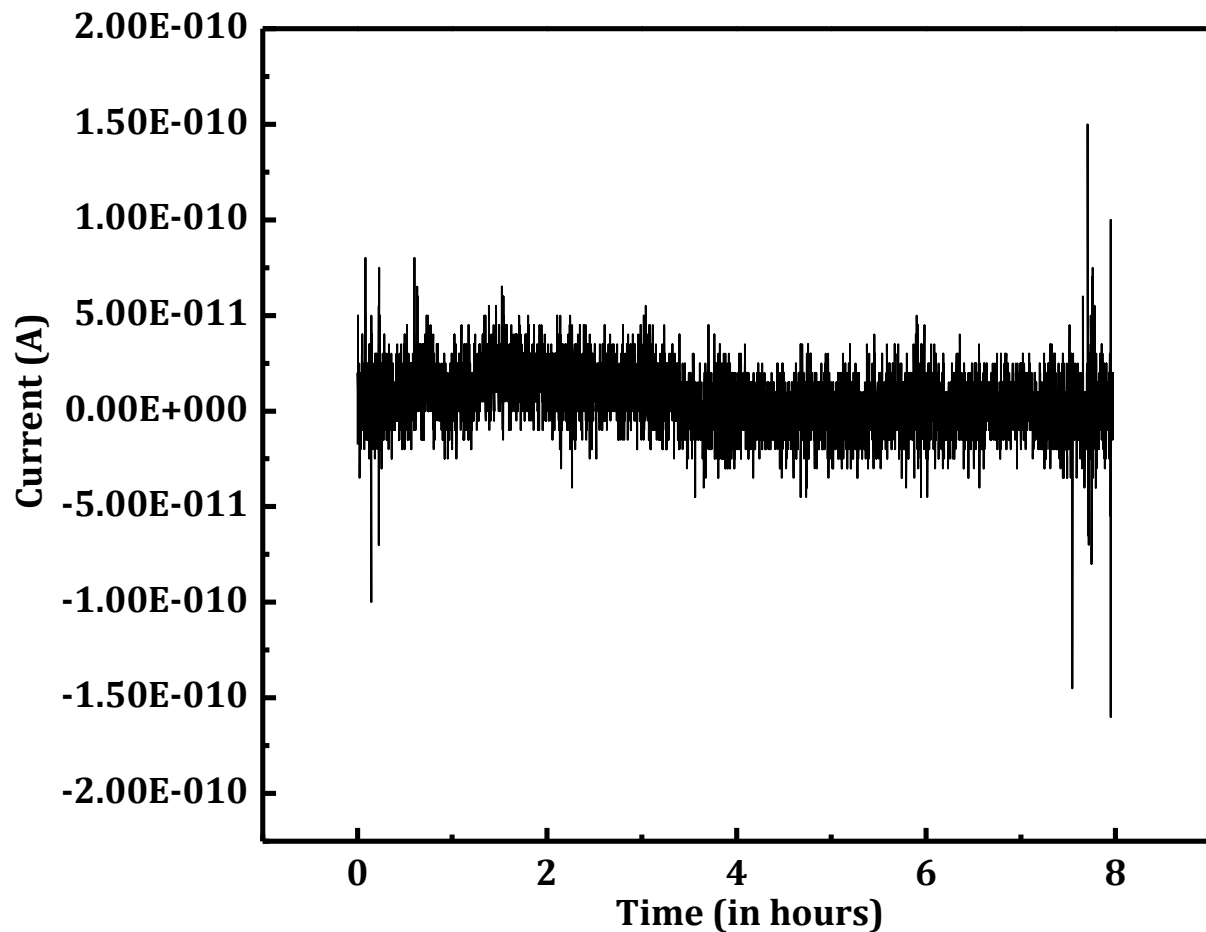


Figure 6-13. A plot of leakage current through the ribbon cables used during measurement.

In order to measure the sensitivity of the sensor, a lower noise test setup was used. The sensors were measured without the use of the ribbon cables on a probe station using the HP 4141B DC SMU. Figure 6-14 shows the electrical output of the temperature sensors measured on the probe station without the ribbon cables. These sensors have sensitivity of 12 mK, a significant improvement from 35 mK measured using ribbon cables.

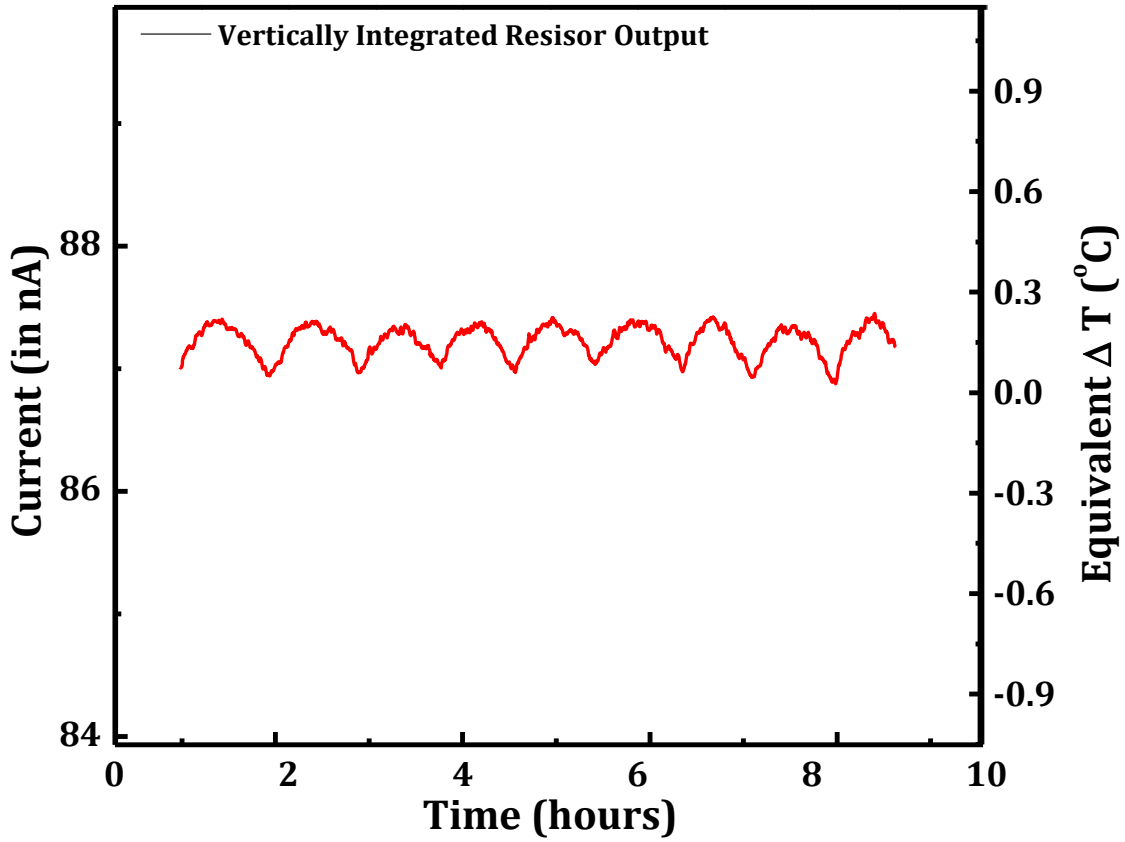


Figure 6-14. Output current of vertically integrated VO_x sensors $10\text{ }\mu\text{m} \times 10\text{ }\mu\text{m} \times 85\text{ nm}$ having a resistance of $1.3\text{ M}\Omega$ at a temperature of $35\text{ }^{\circ}\text{C}$ measured without a switch matrix using the HP4141B DC SMU. The resistor was biased with a voltage of 100 mV . The measured RMS noise was found to be $\approx 12\text{ mK}$.

To evaluate the performance of the TFT integrated temperature sensors, the TFT performance was characterized to extract the threshold voltage (V_T), the resistance of the TFT when turned on (R_{on}) and its mobility. Figure 6-15 (black curve) shows a plot of the $\text{Log}(I_D)$ versus gate voltage (V_G) for a transistor with a width to length ratio (W/L) of $400\text{ }\mu\text{m}/15\text{ }\mu\text{m}$. The extracted differential mobility (red

curve) was found to be $\approx 10 \text{ cm}^2/\text{V-s}$ at a V_{DS} of 1 V at a V_{GS} of 12 V. R_{on} of $\approx 4,000 \Omega$ was achieved for this W/L.

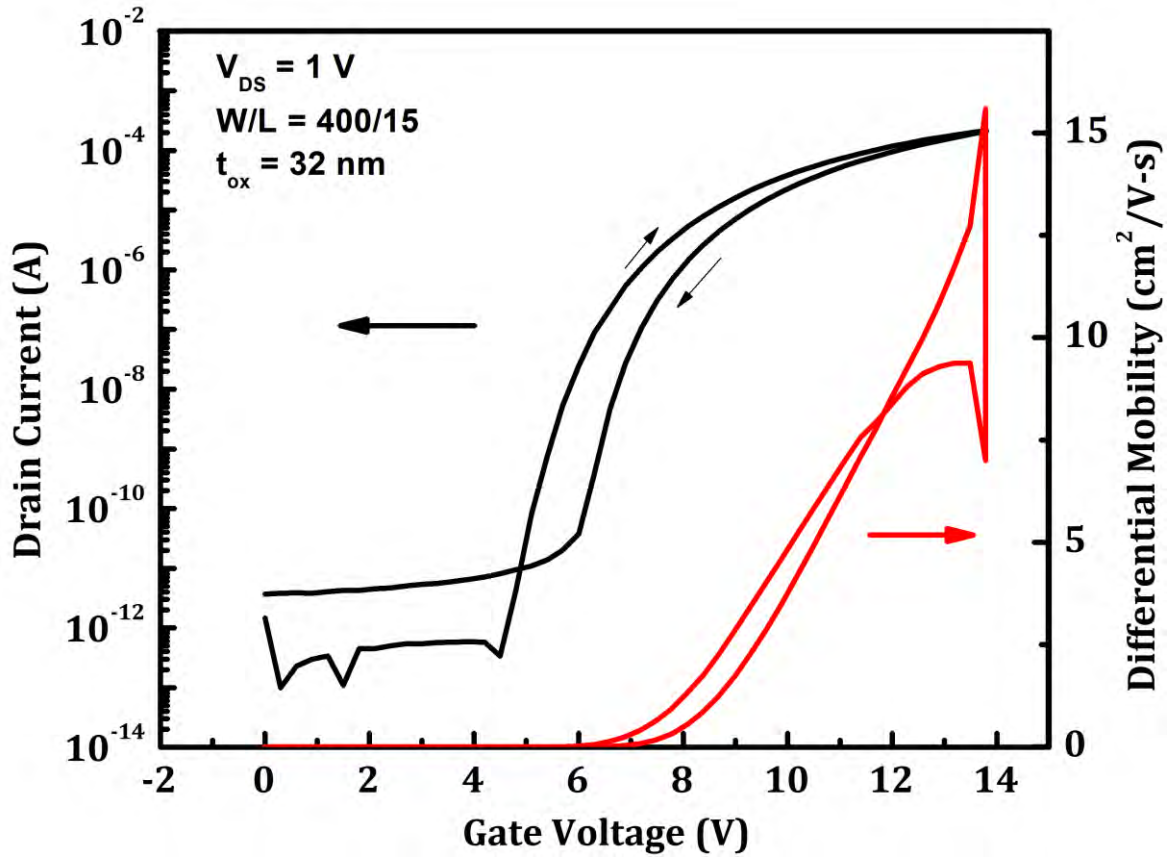


Figure 6-15. Linear region $\log(I_D)$ versus V_{GS} of a ZnO based TFT with a linear region differential mobility of $10 \text{ cm}^2/\text{V-s}$ for a V_{DS} of 1 V. The TFT dimensions are $W/L = 400 \mu\text{m}/15 \mu\text{m}$ and $t_{ox} = 32 \text{ nm}$. The R_{on} for this W/L ratio was $\approx 4,000 \Omega$ for a V_{GS} of 10 V.

Figure 6-16 shows the I_D versus V_G for a ZnO TFT ($W/L = 400 \mu\text{m}/5 \mu\text{m}$) integrated with vertical VO_x resistors ($\approx 1.5 \text{ M}\Omega$) for a V_{DS} of 75 mV. The expected R_{on} for these TFTs is $\approx 1,500 \Omega$. It can be seen that the transistor is off at -1 V and is on at 4 V .

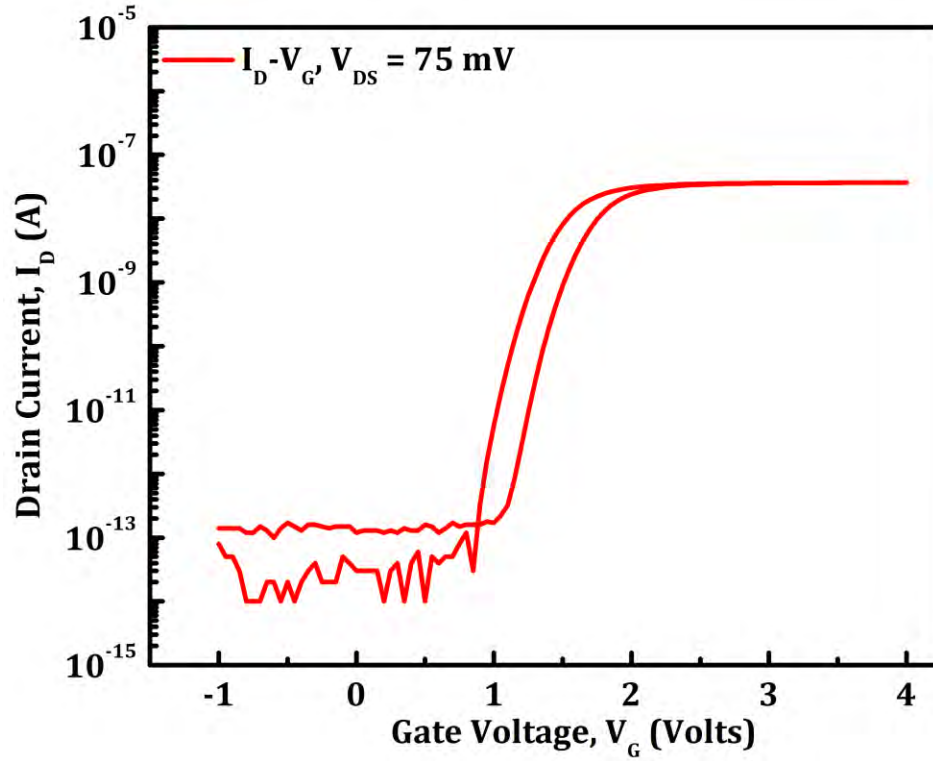


Figure 6-16. Log (I_D) versus V_G for a ZnO based TFT with a vertically integrated with vertically integrated VO_x resistor ($1.6 \text{ M}\Omega$ at room temperature) on the transistor drain for a V_{DS} of 75 mV ($W/L = 450 \text{ }\mu\text{m}/5 \text{ }\mu\text{m}$, $t_{ox} = 32 \text{ nm}$).

Figure 6-17 shows the drain current of the TFT integrated with vertical VO_x thin films structures. As the gate voltage is increased from a V_G of -1 V to $+5 \text{ V}$, the resistor is swept from a bias of -0.1 V to 0.1 V (V_{DS}) and the current is recorded. When the transistor is off, the impedance of the integrated sensor is $10^{11} \Omega$, when the transistor is turned on the resistance is $1.3 \text{ M}\Omega$ (\sim the resistance of the VO_x resistor) for V_{GS} higher than 4 V .

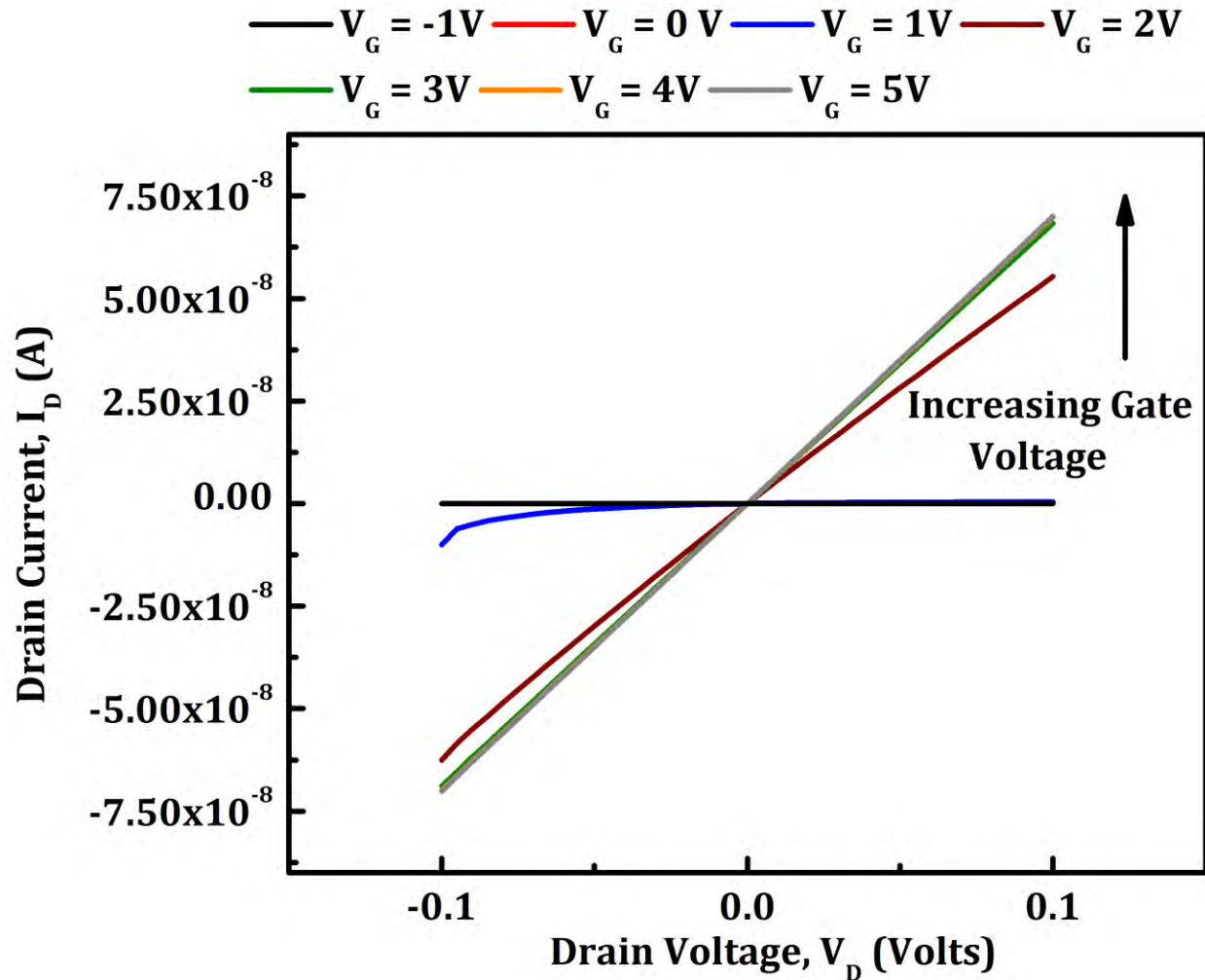


Figure 6-17. I_D versus V_{DS} of a ZnO based TFT with a vertically integrated VO_x resistor ($1.6 \text{ M}\Omega$ at room temperature) on the transistor drain as a function of V_{GS} from -1 V to 5 V ($W/L = 450 \text{ }\mu\text{m}/5 \text{ }\mu\text{m}$, $t_{ox} = 32 \text{ nm}$). I_D - V_D at V_{GS} of 4 V and 5 V are similar indicating a small impedance contribution from the ZnO TFT.

Figure 6-18 shows the I_D - V_D curve of a vertically integrated VO_x sensor incorporated with a ZnO TFT as a function of temperature. The drain voltage is swept from -0.1 V to $+0.1 \text{ V}$ and the resultant current is recorded. During this measurement, the V_{GS} of the TFT is held at $+4 \text{ V}$ so that the transistor is turned on. After each measurement the temperature was increased and the I_D - V_D sweep was collected at this new elevated temperature. The resistance of this vertical device along with the TFT was plotted at various temperatures in a $\ln(\text{resistance})$ versus temperature plot and can be seen in Figure 6-19. The extracted TCR from the activation energy was found to be $-4.4 \text{ \%}/\text{K}$.

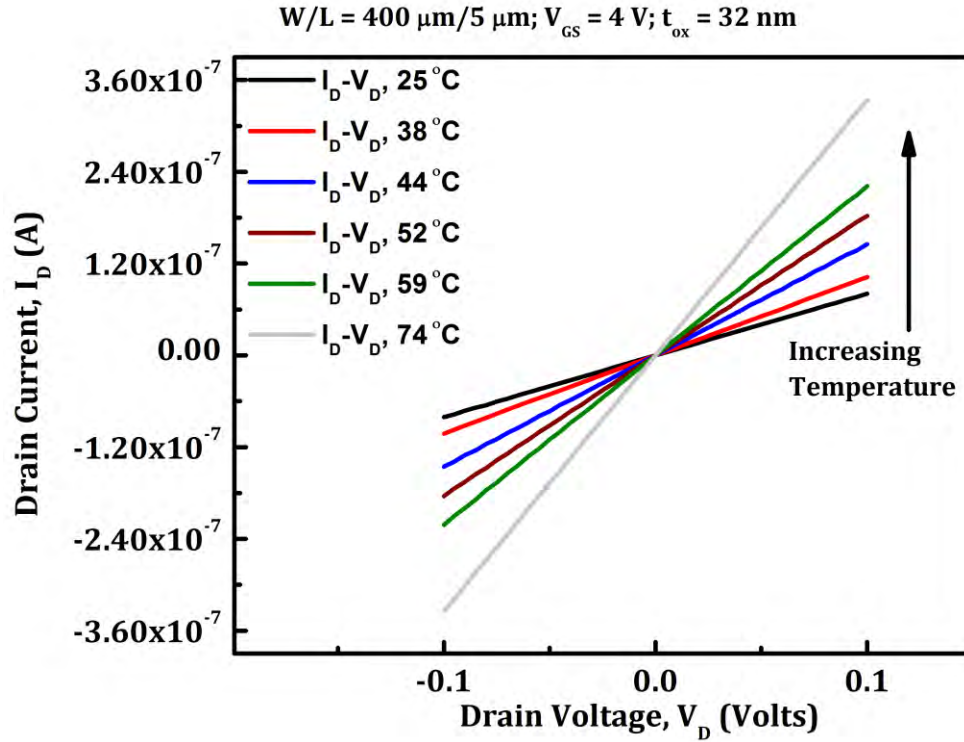


Figure 6-18. I_D versus V_{DS} of a ZnO based TFT with a vertically integrated VO_x resistor ($1.6 \text{ M}\Omega$ at room temperature) on the TFT drain as a function of temperature for a V_{GS} of 5 V ($W/L = 450 \mu\text{m}/5 \mu\text{m}$, $t_{ox} = 32 \text{ nm}$). Increasing temperature of the device leads to lower resistance of the VO_x thin film at higher temperatures which is evident from the increasing slopes of the I_D - V_D characteristics.

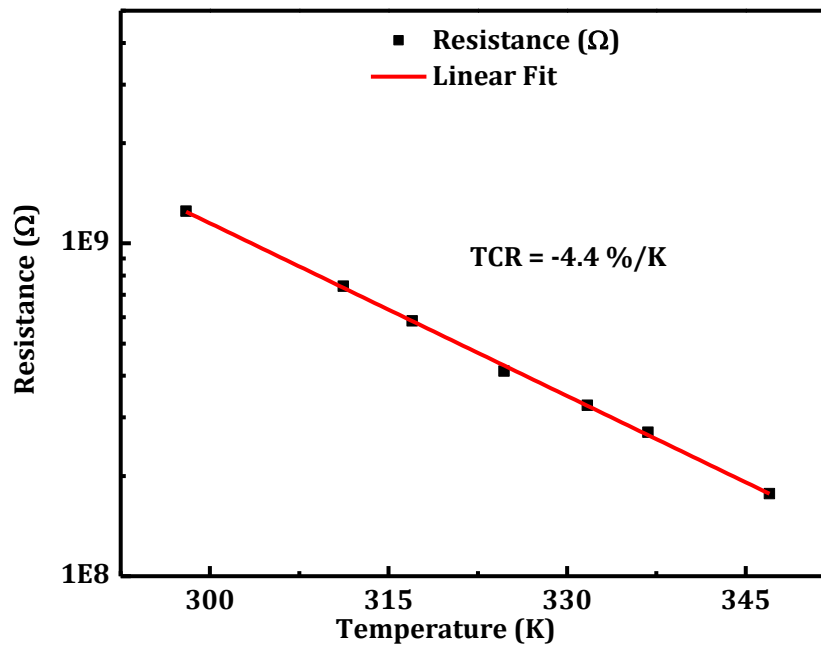


Figure 6-19. $\ln(\text{Resistance})$ versus temperature of vertically integrated VO_x thin film resistors ($1.6 \text{ M}\Omega$ at room temperature) integrated with ZnO TFT at a V_{GS} of 5 V ($W/L = 450 \mu\text{m}/5 \mu\text{m}$, $t_{ox} = 32 \text{ nm}$). The TCR extracted from the activation energy was found to be $-4.4 \text{ \%}/\text{K}$.

6.4. Conclusion

1×8 temperature sensing arrays are fabricated using lateral and vertically integrated thin films of high TCR VO_x thin films. Custom hardware and software was built using a DC SMU and a switch matrix to perform the measurements. Thin film TCR of $-4.4\%/\text{K}$ was maintained in both lateral and vertically integrated structures. The hardware setup allowed for the arrays to have a refresh time of 3.5 seconds. While the arrays using lateral resistance structures have an RMS noise of 160 mK, due to limitations imposed by the hardware setup. The vertically integrated resistors have higher sensitivity due to increased magnitude of the signal. The RMS noise of the vertically integrated structures was found to be 35 mK .

Both the lateral and vertically integrated resistance structures were incorporated along with a ZnO based TFT for device level multiplexing of the sensor arrays. The bias and therefore the current from the resistor could be turned on or off depending on the gate voltage applied to the transistor. Temperature dependent measurements confirmed that the TCR of the thin film material was maintained in these TFT integrated resistance temperature sensors.

Chapter 7. Summary and Future Work

7.1. Summary

High TCR Thin films of VO_x and Ge:H

Resistance based microbolometers are based on two distinct types of materials: materials with $|TCR|$ of 2–2.5 %/K, resistivity between 0.1–1 $\Omega\text{-cm}$ and those with $|TCR|$ between 3–4 %/K with resistivity between 200–2,000 $\Omega\text{-cm}$. This work investigates thin films of Ge:H and VO_x having $|TCR| > 4 \text{ %/K}$.

For thin films of undoped Ge:H deposited by PECVD, it was found that significant improvement in the resistivity, TCR and electrical noise could be achieved for a thickness of $\approx 100 \text{ nm}$ by increasing the dilution ratio of $[\text{GeH}_4]$ in $[\text{H}_2]$ to extremely large values ($R = 400$). Thin films having TCR of $\approx 6.5 \text{ %/K}$ were repeatedly deposited having a resistivity of 2,250 $\Omega\text{-cm}$ and a normalized Hooge's parameter of $\approx 10^{-20} \text{ cm}^3$. In combination with prior work it is concluded that the thickness of thin film showing superior TCR-noise-resistivity tradeoffs could be achieved by could be changed by changing the dilution ratio used during deposition. The combination of electrical properties for thin films of Ge:H deposited in this work are the best in comparison with other materials reported in the literature to date.

Electrical noise in thin films of VO_x with $x > 2$ and $|TCR| > 3 \text{ %/K}$ was largely uninvestigated prior to this work. Thin films having high TCR ($|TCR|$ of 4–5 %/K) were deposited by Biased Target Ion Beam Deposition. These thin films had very high resistivities (between 10,000 to 20,000 $\Omega\text{-cm}$), much higher than those of Ge:H. Their normalized Hooge's parameter values were around 10^{-18} to 10^{-20} cm^3 .

Vertically Integrated High TCR Thin Films

The use of large TCR values in microbolometer applications has been limited by large values of normalized Hooge's parameter and the enormous resistivities ($10,000 \text{ } \Omega\text{-cm}$) associated with these materials. High resistivity leads to high pixel resistance in a lateral resistor configuration. In this work, an alternate pixel structure using vertically integrated high TCR films was demonstrated and its electrical performance was characterized.

This configuration resulted in much lower pixel resistance than the lateral configuration with no change in the signal to noise ratio. In addition, TCR and the normalized Hooge's parameter of the vertically integrated configuration were found to be similar to resistors fabricated in the lateral configuration. The reduced pixel resistance allows for sustaining higher bias currents without an increase in Joule heating and therefore operation in a constant bias mode. In addition, the constant SNR and larger signal current might allow for reduced current integration times and therefore higher imaging frame rates.

Temperature Sensor Arrays

Combination of large TCR materials and low impedance devices developed in this work positions the thermistor based contact based temperature sensor at a distinct advantage over existing micro fabricated temperature sensors. 1-D temperature sensing arrays using thin films having large values of TCR lateral and vertically integrated configurations were fabricated on to glass substrates. 1×8 sensor array using the lateral configuration was demonstrated have an RMS noise value of 160 mK, while vertically integrated resistors showed a much lower RMS noise of 35 mK. To allow for measurement of 2-D arrays, sensors were integrated with ZnO based transistors to turn the current through the resistor on or off depending on the gate voltage applied to the bias with no degradation in the sensor performance.

7.2. Future Work

This dissertation investigated several areas of temperature sensing materials and devices. As a result many questions arose which may be answered by future work. One main area of future work would

be to publish the results on the high TCR materials, the through film structure, the noise measurement system and results, and the temperature sensing array.

High TCR thin films of VO_x:

Thin films of VO_x deposited by BTIBD were grown having high resistivity ($>10,000 \text{ } \Omega\text{-cm}$) and moderate values of Hooge's parameter (10^{-20} to 10^{-18} cm^3). These electrical properties are too large for thin films of high TCR VO_x to be incorporated in existing pulse bias, lateral resistor, read out circuits. There appears to be a large gap in terms of resistivity (from $1 \text{ } \Omega\text{-cm}$ to $10,000 \text{ } \Omega\text{-cm}$), and Hooge's parameter (from 10^{-24} to 10^{-20} cm^3) where thin films of VO_x have not been successfully deposited. It is worth attempting to deposit films in this region to see if the electrical properties of these films are superior films of SiGe:H which are currently used in the constant bias bolometer market.

VO_x thin films with $|\text{TCR}| > 2.5 \text{ } \%/K$ and reasonably low resistivity ($< 0.1 \text{ } \Omega\text{-cm}$) have been deposited by reactive pulsed DC magnetron sputtering of a vanadium target with oxygen [37]. Basantani et al. showed that when thin films of VO_x were deposited using pulsed DC magnetron sputtering, an increase in the oxygen content during sputtering led to an increase in the thin film $|\text{TCR}|$. The $|\text{TCR}|$ increased from $1.2 \text{ } \%/K$ at 4 % of O₂/Ar mixture to $2.1 \text{ } \%/K$ at 11 % O₂/Ar at a substrate bias of -250 V and a sputtering pressure of 2.5 mTorr [44]. In that work, a further increase in the oxygen content led to an abrupt increase in the TCR and resistivity of the thin films. At an O₂/Ar ratio of 12 %, the resistivity increased to $10 \text{ } \Omega\text{-cm}$ and the TCR was $3 \text{ } \%/K$ [44].

In that work, a further increase in the oxygen content was not investigated because thin films having large resistivity were not of interest for that work. However, high TCR and high resistivity thin films are of interest for the constant bias bolometers. Further investigation of the parameter space not covered in ref. [44] could be performed with the deposition of thin films with oxygen percentage in argon from 12 % to 20 %. Some other deposition parameters that were held constant: the total pressure was maintained at 5 mTorr , the substrate bias was kept at -250 V and the total gas flow was held at 18 sccm .

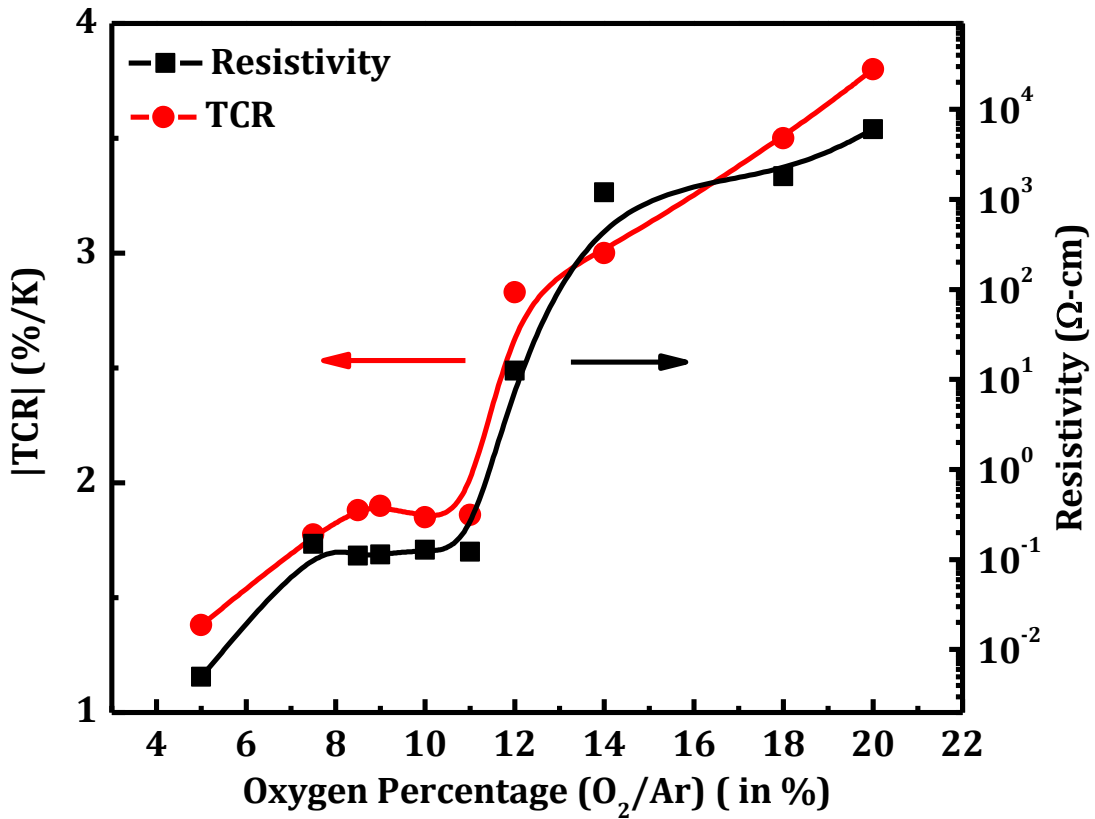


Figure 7-1. Resistivity and TCR of thin films of VO_x deposited by pulsed DC magnetron sputtering using a pure vanadium target with a substrate bias of -250 V. The graph is a compilation of thin films deposited in previous work [44], and films deposited in this work.

Figure 7-1 shows that a further increase in the percentage of oxygen used during deposition led to an increase in the resistivity and the magnitude of TCR for the deposited thin films of VO_x . For the thin film deposited with an oxygen content of 20 %, the resistivity was found to be $\approx 6,000 \text{ } \Omega\text{-cm}$ and the $|\text{TCR}|$ was found to be $\approx 3.8 \text{ } \%/K$. The resistivity and TCR of these thin films are similar to the thin films of VO_x deposited using BTIBD.

Future work for thin films deposited using pulsed DC magnetron sputtering of VO_x thin films should involve investigation of thin films having even higher TCR values. An increase in the oxygen percentage during deposition beyond the 20 % investigated in this work may result in thin films with even

higher TCR values. In addition, the normalized Hooge's parameter must be investigated for thin films of VO_x deposited using pulsed DC magnetron sputtering.

Hydrogenated Germanium Thin Films:

Thin films of Ge:H were deposited with superior electrical properties of TCR ($> 6 \text{ \%}/\text{K}$), resistivity ($2,250 \text{ } \Omega\text{-cm}$), and normalized Hooge's parameter (10^{-20} cm^3). In combination with prior work it is concluded that the thickness of thin films showing superior TCR-noise-resistivity tradeoffs can be adjusted by changing the dilution ratio used during deposition. Through years of investigation, F. N. Hooge concluded that $1/f$ noise of thin films is strongly inversely proportional to the number of carriers available for transport [29]. Therefore, similar to the work done for SiGe:H systems, it is worth investigating if the material properties can be improved by doping of the thin films to increase the available carriers for transport. In the case of SiGe:H thin films, Ajmera et al. and Saint John et al. have demonstrated a decrease in the normalized Hooge's parameter ' α_H/n ' with little change in the TCR of the thin films [18] [19].

Vertically Integrated Thin Films of VO_x :

Vertically integrated thin films of VO_x were demonstrated as an alternate to lateral resistor configurations. A few key questions arose as a result of this work:

1. It was observed that there exists a barrier layer at the interface of the sensing material for both VO_x and Ge:H based devices. Further investigation must be done to identify this barrier layer which may involve the use of a noble metal.
2. Pin hole defect density for large area out of plane devices is a concern which must be addressed to prove manufacturability of vertically integrated bolometer structures.
3. The performance of the vertically integrated sensor has been evaluated by measuring the electrical response as a function of change in temperature. However, the spot temperature

measurements may require additional information on heat transfer between the substrate, the active thin film material as well as the top and bottom electrodes. This information can be obtained by means of Finite Element Analysis (FEA).

4. The true test of this architecture would be to evaluate a pixel incorporated into a free-standing MEMs structure including a full evaluation of the optical and thermal properties of the device.

Temperature Sensor Array:

One dimensional temperature sensing arrays were demonstrated in this work by means of a Keithley 707A general purpose multiplex card. The ability to switch each sensor ON/OFF was also demonstrated by means of integrated ZnO TFTs.

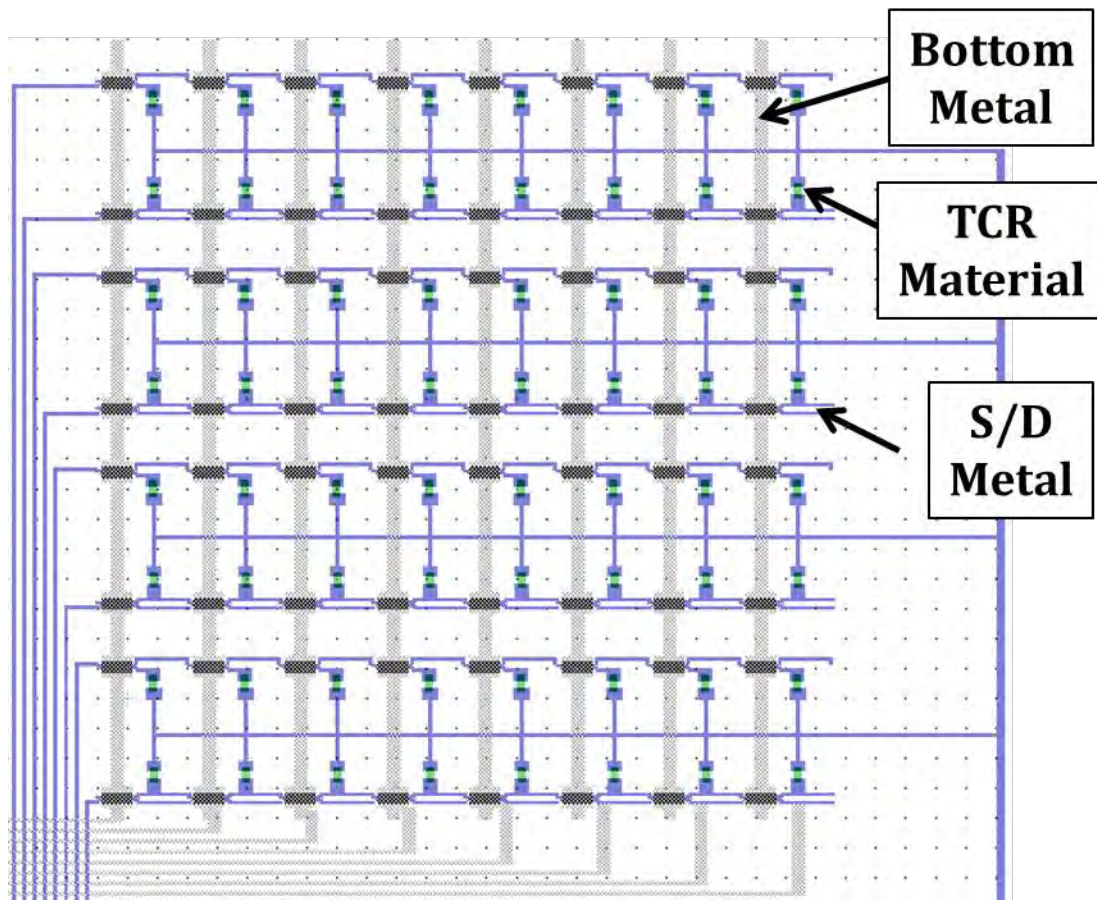


Figure 7-2. A schematic showing the layout of an 8×8 temperature sensor array with integrated TFTs for two dimensional temperature sensing applications.

Future work for the one-dimensional sensor array would be to fabricate them on a flexible, biocompatible substrate for insertion into the body, particularly the brain. This would require temporary attachment of the device on a stiff but small cross-sectional area probe that would allow insertion, dissolution of the adhesive and removal of the probe.

Future work for the temperature sensor array includes measurement of two dimensional temperature sensor arrays with integrated TFTs. Figure 7-2 shows a layout of two dimensional temperature sensor arrays with integrated TFTs for in pixel switching. Hardware test setup must be developed for appropriate biasing of these temperature sensor arrays.

Bibliography

- [1] L. Michalski, K. Eckersdorf, J. Kucharski and J. McGhee, *Temperature Measurement*, Chicester: John Wiley and Sons, Ltd., 2001.
- [2] E. C. Guyer, *Handbook of Applied Thermal Design*, Taylor and Francis, 1999.
- [3] P. W. Kruse and D. Skatrud, *Uncooled Infrared Imaging Array and Systems*, Academic Press, 1997.
- [4] Amphenol Advanced Sensors, "NTC Interchangeable Type 95 Series," 2014.
- [5] Omega, "Introduction to Thermistors," Omega, 2014. [Online]. Available: <http://www.omega.com/prodinfo/thermistor.html>.
- [6] I. Kim, H. Fok, Y. Li, T. N. Jackson and B. J. Gluckman, "Polymer substrate temperature sensor array for brain interfaces," *Engineering in Medicine and Biological Society, Annual International Conference of the IEEE*, pp. 3286-3289, 2011.
- [7] B. E. Cole, "Microstructure design for higher IR sensitivity". Patent US Patent No. 5,286,976, 1994.
- [8] R. Wood, "Use of vanadium oxide in microbolometer sensors". Patent US5450053 A, 29 June 1993.
- [9] FLIR, *FLIR Technical Note*.
- [10] C. P. Cain and A. J. Welch, "Thin-film temperature sensors for biological measurements," *IEEE transactions on Biomedical Engineering*, Vols. BME-21, no. 5, pp. 421-423, 1974.
- [11] D. C. Murphy, S. E. Persson, M. A. Pahre, A. Sivaramakrishnan and S. G. Djorgovski, "An infrared camera for the Palomar Observatory 60-inch telescope," *Publications Astronomical Soc. of the Pacific*, vol. 107, p. 1234–1242, 1995.
- [12] P. W. Kruse, "Thermal Detectors," in *Handbook of Optics*, McGraw-Hill, Inc., 1995, pp. 19.1-19.14.
- [13] C. Hanson and H. Beratan, "Uncooled Pyroelectric Thermal Imaging," in *Proceedings of the Ninth IEEE International Symposium on Applications of Ferroelectrics*, University Park, PA, 1991.
- [14] C. Ye, T. Tamagawa, R. Schiller and D. L. Polla, "Pyroelectric PbTiO₃ Thin Film for Microsensor Applications," *Sensors and Actuators A*, vol. 35, pp. 770-83, 1992.
- [15] FLIR INC., "Uncooled detectors for thermal imaging cameras," [Online]. Available: http://www.flir.com/uploadedFiles/Eurasia/Cores_and_Components/Technical_Notes/uncooled%20detectors%20BST.pdf.

- [16] E. Hayes and M. Rau, "More than meets the eye: the electromagnetic spectrum," *Science in School*, no. 20, 2011.
- [17] P. W. Kruse, *Uncooled thermal imaging-arrays, systems and applications*, Bellingham: SPIE PRes, 2002.
- [18] S. Ajmera, J. Brady, C. Hanson, T. Schimert, A. J. Syllaios and M. Taylor, "Performance improvement in amorphous silicon based uncooled microbolometers through pixel design and materials development.," in *Proc. SPIE 8012, Infrared Technology and Applications XXXVII, 80121L*, 2011.
- [19] D. B. Saint John, *Optical and Electrical Characterization of High Resistivity Semiconductors for Constant-Bias Microbolometer Devices*, PhD Thesis. The Pennsylvania State University, 2012.
- [20] C. Venkatasubramanian, *Preparation, characterization and post deposition modification of pulsed-DC magnetron sputtered vanadium oxide thin films for microbolometer applications*, PhD Thesis. The Pennsylvania State University, 2010.
- [21] B. D. Gauntt, *The nano-composite nature of vanadium oxide thin films for use in infrared microbolometers*, PhD Thesis. The Pennsylvania State University, 2011.
- [22] N. Fieldhouse, S. M. Pursel, R. Carey, M. W. Horn and S. Bharadwaja, "Vanadium oxide thin films for bolometric applications deposited by reactive pulsed DC sputtering," *J. Vac. Sci. Technol. A*, vol. 27, p. 951, 2009.
- [23] B. D. Gauntt, J. Li, O. M. Cabarcos, H. A. Basantani, C. Venkatasubramanian, Bharadwaja, N. J. Podraza, T. N. Jackson, D. L. Allara, S. Antrazi, M. W. Horn and E. C. Dickey, "Microstructure of Vanadium Oxide Used in Microbolometers," *SPIE Proceedings 8012*, 2011.
- [24] S. Baliga, M. Rost and A. Doctor, "Sputtered film thermistor IR detectors," in *SPIE Proc. 2225*, 1994.
- [25] W. Zhou, C. Ouyang, J. Wu, Y. Gao and Z. Huang, "Structural, Morphological and infrared detection properties of Mn-Co-Ni-O spinel oxide films," in *Eighth International Conference on Thin Film Physics and Applications, Proc. of SPIE Vol. 9068*, 2013.
- [26] D. Zhao, *Plasma-enhanced Atomic Layer Deposition Zinc Oxide Flexible Thin Film Electronics*, The Pennsylvania State University.
- [27] S. W. Ko, J. Li, N. J. Podraza, E. C. Dickey and S. Trolier-McKinstry, "Spin Spray-Deposited Nickel Manganite Thermistor Films For Microbolometer Applications," *Journal of the American Ceramic Society*, vol. 94, no. 2, pp. 516-523, 2010.
- [28] F. N. Hooge and L. J. Vandamme, "Lattice Scattering Causes 1/f Noise," *Physics Letters A*, vol. 66, no. 4, pp. 315-316, 1978.

- [29] F. N. Hooge, "1/f Noise Sources," *IEEE Transactions of Electron Devices*, vol. 41, no. 11, p. 1926, 1994.
- [30] R. A. Wood, "Monolithic Silicon Microbolometer Arrays," in *Uncooled Infrared Imaging Arrays and Systems*, vol. 47, P. W. Kruse and D. D. Skatrud, Eds., San Diego, CA, Academic Press, 1997, pp. 45-119.
- [31] P. E. Howard, C. J. Han, J. E. Clarke, J. C. Stevens, P. Ely and E. T. Fitzgibbons, "Advances in Microbolometer Focal Plane Technology at Boeing," in *SPIE Conference on Infrared Detectors and Focal Plane Arrays V*, Orlando Florida, 1998.
- [32] D. Murphy, M. Ray, R. Wyles, J. Asbrock, N. Lum, J. Wyles, A. C. Hewitt, Kennedy, D. V. Lue, J. Anderson, D. Bradley, R. Chin and T. Kostrzewa, "High sensitivity 25 μm microbolometer FPAs," in *Proceedings of SPIE. 4721*, 2002.
- [33] W. A. Radford, D. F. Murphy, M. Ray, S. H. Propst, A. Kennedy, J. K. Kojiro, J. T. Woolaway, K. L. Soch, R. Coda, G. Lung, E. A. Moody, D. Gleichman and S. T. Baur, "320x240 silicon microbolometer uncooled IR FPAs with on-chip offset correction," in *Proc. SPIE 2746, Infrared Detectors and Focal Plane Arrays IV*, Orlando, FL, 1996.
- [34] K. G. West, J. Lu, J. Yu, D. Kirkwood, W. Chen, Y. Pei, J. Claassen and S. A. Wolf, "Growth and characterization of vanadium dioxide thin films prepared by," *Journal of Vacuum Science & Technology A*, vol. 26, no. 1, pp. 133-139, 2008.
- [35] Y.-H. Hana, I.-H. Choia, H.-K. Kang, J.-Y. Park, K.-T. Kim, H.-J. Shin and S. Moon, "Fabrication of vanadium oxide thin film with high-temperature coefficient of resistance using V2O5 / V / V2O5 multi-layers for uncooled microbolometers," *Thin Solid Films*, vol. 205, pp. 260-264, 2003.
- [36] C. Batista, J. Mendes, V. Teixeira and J. Carneiro, "Reactive DC Magnetron Sputtering of Vanadium Oxide Thin Films," *Materials Science Forum*, Vols. 587-588, pp. 343-347, 2008.
- [37] H. A. Basantani, S. Kozlowski, M.-Y. Lee, J. Li, E. C. Dickey, T. N. Jackson, S. S. N. Bharadwaja and M. W. Horn, "Enhanced Electrical and Noise Properties of nanocomposite Vanadium Oxide Thin Films by Reactive Pulsed-DC Magnetron Souttering," *Applied Physics Letters*, vol. 100, 2012.
- [38] N. Fateh, G. A. Fontalvo and C. Mitterer, "Structural and mechanical properties of dc and pulsed dc reactive magnetron sputtered V2O5 films," *Journal of Physics D: Applied Physics*, vol. 40, p. 7716–7719, 2007.
- [39] N. Fieldhouse, S. M. Pursel, R. Carey, M. W. Horn and S. S. N. Bharadwaja, "Vanadium Oxide Thin Films for Bolometric Applications Deposited by Reactive Pulsed DC Sputtering," *Journal of Vacuum Science & Technology A*, vol. 27, p. 951, 2009.

- [40] K. Wells, Properties of Pulsed DC Sputtered Vanadium Oxide Thin Films Using a V₂O₃ Target for Uncooled Microbolometers, The Pennsylvania State University, 2008.
- [41] C. Venkatasubramanian, M. O. Cabarcos, R. W. Drawl, L. D. Allara, R. W. Drawl, S. Ashok, M. W. Horn and S. S. N. Bharadwaja, "Process-structure-property correlations in pulsed dc reactive magnetron sputtered vanadium oxide thin films," *Journal of Vacuum Science & Technology A*, vol. 29, no. 6, 2011.
- [42] C. O. M. C. W. R. D. D. L. A. S. A. M. W. H. a. S. S. N. B. Venkatasubramanian, "Process-structure-property Correlations in Pulsed Dc Reactive Magnetron Sputtered Vanadium Oxide Thin Films," *Journal of Vacuum Science & Technology A: Vacuum, Surfaces, and Films*, vol. 29, no. 6, p. 061504, 2011.
- [43] B. D. Gauntt, O. M. C. J. Li, H. A. Basantani, C. Venkatasubramanian, S. S. N. Bharadwaja, N. J. Podraza, T. N. Jackson, D. L. Allara, S. Antrazi, M. W. Horn and E. C. Dickey, "Microstructure of vanadium oxide used in microbolometers," in *SPIE Proceedings: Infrared Technology and Applications 8012*, 2011, 2011.
- [44] H. A. Basantani, Effect of RF Substrate Bias on Vanadium Oxide Thin Films During Reactive Pulsed DC Magnetron Sputter Deposition, The Pennsylvania State University, 2011.
- [45] B. D. Gauntt, M. W. Horn and E. C. Dickey, "Stoichiometry and microstructural effects on electrical conduction in pulsed dc sputtered vanadium oxide thin films," *Journal of Material Research*, vol. 24, no. 4, 2009.
- [46] H. Wang, X. Yi, S. Chen and S. He, "Reactive Ion Beams Sputtering of Vanadium Oxides Films for Uncooled Microbolometer," *International Journal of Infrared and Millimeter Waves*, vol. 26, no. 3, pp. 421-431, 2005.
- [47] T. L. Hylton, B. Ciorneiu, D. A. Baldwin and O. Escorcia, "Thin Film processing by biased target ion beam deposition," *IEEE Transactions of Magnetics*, pp. 2966-2971, 2000.
- [48] R. Street, Technology and Applications of Amorphous Silicon, New york, 2000.
- [49] H. Klauk, S. L. Wright, L. F. Palmateer, S. E. Mohny and T. N. Jackson, "Hydrogenated Amorphous Silicon Germanium Black-matrix Material for Active-matrix Liquid-crystal Displays," *Journal of the Society for Information Display* 5, vol. 4, p. 393, 1997.
- [50] J. -L. Tissot, F. Rotham, C. Vedel, M. Vilain and J.-J. Yon, "LETI/LIR's Amorphous Silicon Uncooled Microbolometer Development," in *Proc. SPIE 3379, Infrared Detectors and Focal Plane Arrays V*, 1998.

- [51] D. B. Saint John, H.-B. Shin, M.-Y. Lee, E. C. Dickey, N. J. Podraza and T. N. Jackson, "Thin film silicon and germanium for uncooled microbolometer applications," in *Proc. SPIE 8012, Infrared Technology and Applications XXXVII, 80123U*, 2011.
- [52] C. Godet, I. E. Zawawi, M. Théye, M. Gauthier and J. Stoquert, "Improvement of Plasma-deposited a-Ge : H Thin Films by Hydrogen Dilution of Germane," *Solid State Communications*, vol. 74, pp. 721-725, 1990.
- [53] I. Chambouleyron, C. F. Graeff, A. R. Zanatta, F. Fajardo, M. Mulato, R. Campomanes, D. Comedi and F. C. Marques, "The Perspectives of Hydrogenated Amorphous Germanium as an Electronic Material," *Physica Status Solidi (b)*, vol. 192, no. 2, pp. 241-251, 1995.
- [54] W. Palz, G. T. Wrixon and P. Helm, in *Ninth E.C. Photovoltaic Solar Energy Conference: Proceedings of the International Conference*, Freiburg, Fed. Rep. of Germany, 1989.
- [55] M. Stutzmann, J. Stuke and H. Dersch, "Electron Spin Resonance of Doped Glow-discharge Amorphous Germanium," *Physica Status Solidi (b)*, vol. 115, no. 1, pp. 141-151, 1983.
- [56] F. C. Marques and I. Chambouleyron, "Optoelectronic Properties of High Quality Hydrogenated Amorphous Germanium Thin Films," in *Proceedings of the Ninth E. C. Photovoltaic Solar Energy Conference*, Freiburg, Germany, 1989.
- [57] M. Moreno, A. Torres, R. Ambrosio, P. Rosales, A. Heredia, A. Kosarev, E. Torres, C. Zuñiga, C. Reyes-Betanzo and M. Domínguez, "Deposition and characterization of polymorphous germanium films prepared by low frequency PECVD," *Journal of Non-Crystalline Solids*, vol. 358, no. 17, pp. 2099-2102, 2012.
- [58] N. J. Podraza, D. B. S. John, J. Li, C. R. Wronski, E. C. Dickey and R. W. Collins, "Microstructural Evolution in Si(1-x)Ge_x:H Thin Films for Photovoltaic Applications," in *Proceedings of the 35th Photovoltaic Specialists Conference*, 2010.
- [59] W. J. Parrish, J. T. W. II, G. T. Kincaid, J. L. Heath and J. D. Frank, "Low-cost 160 x 128 uncooled infrared sensor array," in *Proc. SPIE 3360, Infrared Readout Electronics IV, 111*, 1998.
- [60] C. M. Hanson, S. K. Ajmera, J. Brady, T. Fagan, W. McCardel, D. Morgan, T. Schimert, A. J. Syllaos and M. F. Taylor, "Small pixel a-Si/a-SiGe bolometer focal plane array technology at L-3 Communications," *Proc. SPIE 7660, Infrared Technology and Applications XXXVI*, p. 76600R, 2010.
- [61] V. V. Zhurin, *Industrial Ion Sources: Broadbeam Gridless Ion Sources Technology.*, Weinheim: Wiley-VCH, 2012.
- [62] 4Wave Inc., "LABORATORY ALLOY and NANOLAYER SPUTTERING," [Online]. Available:

<http://www.4waveinc.com/dslans.html>.

- [63] Kaufman & Robinson Inc., "Broad Beam Sources," [Online]. Available: <http://www.ionsources.com/eh1000.htm>.
- [64] H. R. Kaufman, R. S. Robinson and R. I. Seddon, "End-Hall Ion Sources," *J. Vac. Sci. Technol.*, pp. 2081-2084, 1987.
- [65] H. R. Kaufman, "Explanation of Bohm diffusion," *J. Vac. Sci. Technol. B*, vol. 8, p. 107, 1990.
- [66] J. J. Cuomo, S. M. Rossmagel and H. R. C. W. S. Kaufman, *Handbook of Ion Beam Processing Technology - Principles, Deposition, Film Modification and Synthesis*, Westwood, New Jersey: Noyes Publications, 1989.
- [67] J. R. H. R. K. R. E. N. R. S. R. a. C. M. S. Kahn, "Low Energy End-Hall Ion Source Characterization at Millitorr Pressures," *Society of Vacuum Coaters Technical Conference Proceedings*, 2005.
- [68] Kaufman & Robinson Inc., *EH1000 Ion Source Manual Filament Cathode Version*, Fort Collins, Colorado, 2003.
- [69] J.-L. Delcroix and A. R. Trinidade, "Hollow Cathode Arcs," *Advances in Electronics and Electron Physics*, vol. 35, pp. 87-190, 1974.
- [70] D. Faircloth, "Ion sources for high-power hadron accelerators," in *CERN Accelerator School CAS 2011: High Power Hadron Machines*, Bilbao, 2011.
- [71] M. C. Shonka, R. J. Kahn and R. H. Kaufman. Patent US 7,728,498, 2010.
- [72] N. J. Podraza, *Real Time Spectroscopic Ellipsometry of the Growth and Phase Evolution of Thin Film Si_{1-x}Gex:H*, The Pennsylvania State University, 2008.
- [73] R. Street, *Technology and Applications of Amorphous Silicon*, New York, 2000.
- [74] D. Saint John, *Optical and Electrical Characterization of High Resistivity Semiconductors for Constant-Bias Microbolometers*, 2012.
- [75] T. C. o. D. School of Physics, "Ellipsometry - Surface and Interface Physics," Dublin, 2012.
- [76] D. K. Schroder, *Semiconductor Material and Device Characterization*, Wiley-IEEE Press, 2006.
- [77] W. A. Lentz, *Characterization of noise in Uncooled IR Bolometer Arrays*, Massachusetts Institute of Technology, 1998.

- [78] T. Schimert, J. Brady, T. Fagan, M. Taylor, W. McCardel, R. Gooch, S. Ajmera, C. Hanson and A. J. Syllaos, "Amorphous silicon based large format uncooled FPA microbolometer technology," *Infrared Technology and Applications XXXIV*, p. 694023, 17 April 2008.
- [79] Y. Jin, H. A. Basantani, A. O. Ozcelik, T. N. Jackson and M. W. Horn, "High-resistivity and high-TCR vanadium oxide thin films for infrared imaging prepared by bias target ion-beam deposition," in *SPIE Conference Proceedings Vol. 8704*, Baltimore, 2013.
- [80] H. Klauk, S. L. Wright, L. F. Palmateer, S. E. Mohny and T. N. Jackson, "Hydrogenated Amorphous Silicon Germanium Black-matrix Material for Active-matrix Liquid-crystal Displays," *Journal of the Society for Information Display* 5, vol. 4, p. 393, 1997.
- [81] *SIMNRA software from max-Planck Institute for Physics was used to fit the RBS for compositional analysis.*
- [82] F. N. Hooge, T. G. M. Kleinpenning and L. K. J. Vandamme, "Experimental studies on 1/f noise," *Reports on Progress in Physics*, vol. 44, no. 5, 1981.
- [83] N. Podraza, B. Gauntt, M. Motyka, E. Dickey and M. Horn, "Electrical and optical properties of sputtered amorphous vanadium oxide thin films," *Journal of Applied Physics*, vol. 111, no. 7, 2012.
- [84] J. L. C. T. B. F. A. C. a. O. L. Tissot, "Uncooled Microbolometer Detector: Recent Developments at ULIS," *Opto-Electronics Review*, vol. 14, no. 1, pp. 25-32, 2006.
- [85] B. D. Cullity, *Elements of X-ray Diffraction*, Addison-Wesley Publishing Company, Inc., 1978.
- [86] R. W. Collins, A. S. Ferlauto, G. M. Ferreira, J. K. C. Chen, R. J. Koval, Y. Lee, J. M. Pearce and C. R. Wronski, "Evolution of microstructure and phase in amorphous, protocrystalline, and microcrystalline silicon studied by real time spectroscopic ellipsometry," *Solar Energy Materials and Solar Cells*, vol. 78, pp. 143-180, 2003.
- [87] N. J. Podraza, J. Li, C. R. Wronski, E. C. Dickey and R. W. Collins, "Analysis of controlled mixed-phase (amorphous + microcrystalline) silicon thin films by real time spectroscopic ellipsometry," *Journal of Vacuum Science & Technology A: Vacuum, Surfaces & Technology*, vol. 27, no. 6, pp. 1255-1259, 2009.
- [88] Y. Cong, I. An, K. Vedam and R. W. Collins, "Optical characterization of a four-medium thin film structure by real time spectroscopic ellipsometry: amorphous carbon on tantalum," *Applied Optics*, vol. 30, pp. 2692-2703, 1991.
- [89] D. E. Aspnes, "Minimal-data approaches for determining outer-layer dielectric responses of films from kinetic reflectometric and ellipsometric measurements," *Journal of the Optical Society of*

America A, vol. 10, pp. 974-983, 1993.

- [90] A. S. Ferlauto, G. M. Ferreira, R. J. Koval, J. M. Pearce, C. R. Wronski, R. W. Collins, M. M. Al-Jassim and K. M. Jones, "Evaluation of compositional depth profiles in mixed-phase (amorphous+crystalline) silicon films from real time spectroscopic ellipsometry," *Thin Solid Films*, Vols. 455-456, pp. 665-669, 2004.
- [91] N. J. Podraza, J. Li, C. R. Wronski, E. C. Dickey, M. W. Horn and R. W. Collins, "Analysis of Si_{1-x}Ge_x:H thin films with graded composition and structure by real time spectroscopic ellipsometry," *Physica Status Solidi A*, vol. 205, pp. 892-895, 2008.
- [92] H. Fujiwara, J. Koh, P. I. Rovira and R. W. Collins, "Assessment of effective-medium theories in the analysis of nucleation and microscopic surface roughness evolution in semiconductor thin films," *Physical Review B*, vol. 61, pp. 10832-10844, 2000.
- [93] P. Lautenschlage, M. Garriga, L. Vina and M. Cardona, "Temperature dependence of the dielectric function and interband critical points in silicon," *Physical Review B*, Vols. 4821-4830, p. 36, 1987.
- [94] A. S. Ferlauto, G. M. Ferreira, J. M. Pearce, C. R. Wronski and R. W. Collins, "Analytical model for the optical functions of amorphous semiconductors from the near-infrared to ultraviolet: applications in thin film photovoltaics," *Journal of Applied Physics*, vol. 92, pp. 2424-2436, 2002.
- [95] N. J. Podraza, C. R. Wronski, M. W. Horn and R. W. Collins, "Dielectric functions of a-Si_{1-x}Ge_x:H vs. Ge content, temperature, and processing: advances in optical function parameterization," in *Materials Research Society Symposia Proceedings*, 2006.
- [96] G. E. Jellison Jr. and F. A. Modine, "Parameterization of the Optical Functions of Amorphous Materials in the Interband Region," *Applied Physics Letters*, vol. 69, p. 371, 1996.
- [97] G. E. J. Jr. and F. A. Modine, "Erratum: Parameterization of the Optical Functions of Amorphous Materials in the Interband Region," *Applied Physics Letters*, vol. 69, p. 371, 1996.
- [98] Y. Z. Hu, J.-T. Zettler, Y. S. Chongsawangvirod, Q. Wang and E. A. Irene, "Spectroscopic ellipsometric measurements of the dielectric function of germanium dioxide films on crystal germanium," *Applied Physics Letters*, vol. 61, pp. 1098-1100, 1992.
- [99] M. A. Motyka, B. D. Gauntt, M. W. Horn and N. J. Podraza, "Optical properties and microstructural evolution of vanadium oxide prepared by pulsed-DC magnetron sputtering," *Journal of Applied Physics*, p. 112, 2012.
- [100] T. Schimert, C. Hanson, J. Brady, T. Fagan, M. Taylor, W. McCardel, R. Gooch, M. Gohlke and A. J. Syllaos, "Advances in small-pixel, large-format α -Si bolometer arrays," *Infrared Technology and*

Applications XXXV, vol. 7298, p. 72980T, 7 May 2009.

- [101] P. Topart, F. Picard, S. Ilias, C. Alain, C. Chevalier, B. Fisette, J. E. Paultre, F. Génèreux, M. Legros, J.-F. Lepage, C. Laverdière, L. N. Phong, J.-S. Caron and Y. Desroches, "Heterogeneous MEMS device assembly and integration," in *Proc. SPIE 8975, Reliability, Packaging, Testing, and Characterization of MOEMS/MEMS, Nanodevices, and Nanomaterials XIII*, 89750E, 2014.
- [102] M. Yazici, H. Kayahan, O. Ceylan and Y. Gurbuz, "A new unit cell design with automatic input stage selection capability for increased SNR," in *Proc. SPIE 8704, Infrared Technology and Applications XXXIX*, 870409, 2013.
- [103] M. U. Pralle, J. E. Carey, H. Haddad, C. Vineis, J. Sickler, X. Li, J. Jiang, F. Sahebi, C. Palsule and J. McKee, "IR CMOS: infrared enhanced silicon imaging," in *Proc. SPIE 8704, Infrared Technology and Applications XXXIX*, 870407, 2013.
- [104] P. Robert, J. Tissot, D. Pochic, V. Gravot, F. Bonnaire, H. Clerambault, A. Durand and S. Tinnes, "Easy to use uncooled ¼ VGA 17 µm FPA development for high performance compact and low-power systems," in *Proc. SPIE 8353, Infrared Technology and Applications XXXVIII*, 83531F, 2012.
- [105] M. L. Hai, M. Hesani, J. Lin, Q. Cheng, M. Jalal, A. J. Syllaos, S. Ajmera and M. Almasri, "Uncooled silicon germanium oxide (SixGe_{1-x}O_{1-x-y}) thin films for infrared detection," in *Proc. SPIE 8353, Infrared Technology and Applications XXXVIII*, 835317, 2012.
- [106] Y. Jin, H. A. Basantani, A. Ozcelik, T. N. Jackson and M. W. Horn, "High-resistivity and high-TCR vanadium oxide thin films for infrared imaging prepared by bias target ion-beam deposition," in *Proc. SPIE 8704, Infrared Technology and Applications XXXIX*, 87043C, 2013.
- [107] M. H. Unewisse, B. I. Craig, R. J. Watson, O. Reinhold and K. C. Liddiard, "Growth and properties of semiconductor bolometers for infrared detection," in *SPIE Proceedings 2554*, 1995.
- [108] M. Moreno, A. Torres and A. Kosarev, "Uncooled microbolometers with GexSi_{1-x} thermo-sensing layer deposited by plasma with different device configurations," in *SPIE Proceedings*, 2010.
- [109] "New paints and coatings with specific properties in the near and the far infrared," IPS Innovations, 2007. [Online]. Available: http://www.ips-innovations.com/new_paints_ref.htm.

Vita

Hitesh Basantani

Hitesh Arjun Basantani [REDACTED]

[REDACTED]. They moved to New Delhi, India for a few years during the Gulf War of 1990 before returning back to Kuwait in 1992. Hitesh graduated from the Carmel School of Kuwait in 2004. He moved to The Penn State University for his B.S. and M.S. degree in Engineering Science and Mechanics, which he obtained in 2009 and 2011 respectively. His Master's thesis was on the development of vanadium oxide thin films for microbolometer application.

Following the obtaining of his M.S. degree, he stayed at Penn State for his Ph.D and was the first Super User for the Penn State Nanofabrication Facility. Here he worked on magnetron and low energy ion beam deposition systems. His Ph.D. work was on temperature sensing materials and devices.

In July of 2014, Hitesh accepted a position at Intel within the Intel Mask Operations Unit and will be moving to Hillsboro, OR with his fiancée Jennifer Ober.